TUNABLE ZNO SURFACE ACOUSTIC WAVE DEVICES BASED ON ACOUSTOELECTRIC INTERACTION

by

JUN ZHU

A Dissertation submitted to the

Graduate School-New Brunswick

Rutgers, The State University of New Jersey

in partial fulfillment of the requirements

for the degree of

Doctor of Philosophy

Graduate Program in Electrical and Computer Engineering

Written under the direction of

Professor Yicheng Lu

And approved by

_____

_____

_____

_____

New Brunswick, New Jersey

January, 2008

ABSTRACT OF THE DISSERTATION

TUNABLE ZNO SURFACE ACOUSTIC WAVE DEVICES BASED ON ACOUSTOELECTRIC INTERACTION

by JUN ZHU

Dissertation Director:

Professor Yicheng Lu

Tunable surface acoustic wave (SAW) devices have been attracting considerable research efforts, as they are highly desired in advanced communication systems by offering versatile signal processing capability. Among various tuning mechanisms, the perturbation of the electrical boundary condition based on the acoustoelectric interaction in a semiconducting/piezoelectric multilayer structure is a promising approach to realize tunable SAW devices with low bias, large tunability, and small device dimension. To reduce the fabrication complexity and enhance the device reliability, the monolithic device structure is preferable.

This dissertation addresses the design and development of the tunable ZnO SAW devices based on the acoustoelectric interaction. Epitaxial ZnO and $Mg_xZn_{1-x}O$ multilayer structures grown by metal-organic chemical vapor deposition (MOCVD) on r-Al_2O_3 substrates are used as the basic structure, which offer advantages as high coupling

coefficient and multimode SAW generation. The device related processing techniques, including wet chemical and dry etching of ZnO and $Mg_xZn_{1-x}O$ films, are investigated with respect to the etch rate, etch profile, surface morphology and process induced damage. The maximal 1:1 pattern edge slope has been achieved.

A prototype of ZnO UV SAW device has been demonstrated using semiconducting-piezoelectric ZnO multilayer structure, which enables the wireless output for sensor network. The interaction of the SAW with the UV induced carriers in the semiconducting ZnO layer results in a phase shift and an insertion loss change, as functions of the incident light wavelength and power. A phase shift of 107^o is achieved at 365 nm for a light power of 2.32 mW/ cm^2.

A prototype of ZnO based voltage controlled multi-mode tunable SAW device has been demonstrated through the integration of a depletion-type MIS structure (Al/SiO_2/semiconducting ZnO) and a piezoelectric ZnO/r-Al_2O_3 system. The acoustic velocity tunability is achieved by changing the sheet conductivity of the semiconducting channel through the gate biasing. Due to the in-plane piezoelectric anisotropy of the ZnO/r-Al_2O_3 system, the device can be operated with both Sezawa and Love mode for gaseous and liquid sensing, respectively. Under –18 V bias, 420^o and 277.3^o phase shifts are achieved for Sezawa and Love mode operation, respectively.

Dedicated to

My parents and my wife

ACKNOWLEDGEMENTS

I would like to take this opportunity to express my sincere gratitude and appreciation to my advisor, Prof. Yicheng Lu, for his invaluable guidance, insightful encouragement and patient critique through out my Ph.D. study in Rutgers University. From his words and action, I learned not only the research methodology in science and technology, but also the merits to become a scientific researcher.

I would like to greatly thank all the members of my dissertation committee, Professor Ahmad Safari, Professor Paul Panayatatos, and Professor Wei Jiang for devoting their time and expertise to review my dissertation. I thank Dr. K. P. Cheung and Professor Kuang Sheng for many valuable technical discussions. I thank Dr. Boris V. Yakshinskiy for helping me the surface characterization in the ZnO etching study.

I would like to thank my fellow co-workers in Prof. Lu's research group, who have provided continuous support throughout my work: Dr. Nuri W. Emanetoglu, Dr. Yiming Chen, Dr. Sriram Muthukumar, Dr. Rich Wittstruck, Dr. Haifeng Sheng, Dr. Jian Zhong, Dr. Pan Wu, Mr. Gaurav Saraf, Mr. Hanhong Cheng, Ms. Ying Chen, Ms. Zheng Zhang, Mr. Ziqing Duan, and Mr. Pavel Rayes. I would like to express my sincere appreciation for their constant help in research, valuable technical discussion, and friendly collaboration.

I would like to thank my family and friends for their support and help through my studies and research in Rutgers. In particular, I would like to thank my parents and wife, who have always supported me with their love, understanding, encouragement and wisdom. Financial supports from NSF and NJCST are highly appreciated.

TABLE OF CONTENTS

LIST OF ILLUSTRATIONS

LIST OF TABLES

Chapter 1. Introduction

1.1 Motivation

Surface Acoustic Wave (SAW) devices utilize one or more interdigital transducers (IDTs) to convert acoustic wave to electrical signal and vice versa utilizing the piezoelectric effect of certain materials. SAW devices can be designed to provide quite complex signal processing functions within a single package. Due to their special advantages such as mass-producible, low cost, small size, lightweight and versatile functionality, SAW devices have been widely employed in telecommunications as bandpass and spectrum-shaping filters, convolvers, duplexers and delay lines. In addition, SAW devices are also used in Wide Area Network (WAN), Wireless Local Area Network (WLAN) communications, wireless passive identifications tags, miniature chemical/biochemical sensors.

In the development of SAW devices, one important phenomenon, the acoustoelectric interaction, has been continuously studied and implemented for various signal processing applications, such as the acoustoelectric amplifier, acoustic convolver, optical scanner, acoustic focusing and imaging devices, etc. This acoustoelectric interaction is based on the fact that there is a longitudinal electric field associating with the surface acoustic waves, which propagates along the surface of a piezoelectric material. When a semiconducting layer is located close to the surface of a piezoelectric material, on which the SAW is propagating, the acoustoelectric interaction between the SAW associated longitudinal electric field and free carriers in the semiconductor will influence the SAW propagation properties by resulting in attenuation due to ohmic loss and velocity change due to the piezoelectric stiffening of the material. The acoustoelectric

interaction can be exploited with many different effects, such as field effect controlled or photon induced carrier changes, etc., leading to a family of novel multifunctional tunable SAW devices.

Traditional photoconductor and photodiode type UV sensing devices require either voltage or current to drive. The direct wire connection and additional power supply become necessary. These requirements limit their applications in the distributed sensor network. Based on the acoustoelectric interaction, by integrating UV sensing function with SAW technology, zero power and wireless UV sensing devices can be realized. The UV induced free carriers in the semiconducting sensing layer interact with the electric field accompanying the propagating SAW, resulting in a velocity reduction and increased insertion loss, leading to a phase shift and a time delay across the device. In the UV SAW device, the UV sensing information is transported in frequency domain. UV SAW device will find potential applications in early missile threat warning, chemical and biological agent detection, engine flame detection and pollution monitoring, etc.

For traditional SAW devices, one of the major limits is lack of the tunability of the operation frequency and wave velocity. However, in many modern communication systems, adaptive filters for signal processing are desired for increased signal to noise performance and security concerns. Furthermore, tunability of the time or frequency domain response is desirable for the system to adapt to its operating environment. Some tunable SAW device concepts have been proposed based on various tuning mechanisms, including filter banks with selectable filters, perturbation of piezoelectric material properties and perturbation of SAW propagating boundary conditions. In comparison with other tuning mechanisms, the perturbation of the electrical boundary condition based

on the acoustoelectric interaction is more practical to realize tunable SAW device with low bias, large tunability range, continuously tuning and small dimension. By considering the fabrication complexity, production yield and device reliability, a monolithic device is preferable.

Zinc oxide (ZnO) is a versatile material and has many applications including optoelectronic devices, acoustic wave devices, piezoelectric MEMS actuators, and sensors. The as-grown ZnO is n-type semiconductor. Through proper doping or alloying, ZnO can be made piezoelectric, ferromagnetic and conducting. ZnO is a wide band gap semiconductor ($E_g \approx 3.3$ eV at room temperature). In comparison to conventional Si based photosensitive devices, ZnO possess excellent optical properties for high sensitive UV detection. As a piezoelectric material, ZnO can be deposited on various substrates with high coupling coefficient. Based on the acoustoelectric interaction, the ZnO UV sensing layer can be monolithically integrated with ZnO piezoelectric layer to form ZnO UV SAW devices, which offer advantages as high UV sensitivity, passive operation and RF wireless readout. By integrating the ZnO based MIS or MES structure with SAW device, the voltage controlled charge density change can directly impact the SAW propagation and tune the acoustic velocity. In the acoustoelectric interaction, the electromechanical coupling coefficient, the measure of the efficiency of a given piezoelectric in converting the electrical signal into mechanical energy, is the key factor influencing the magnitude of the interaction and directly impacts the performance of the UV SAW and tunable SAW devices. In this work, ZnO/r-Al_2O_3 material system is used, which offer high electromechanical coupling coefficients, low insertion loss and high acoustic velocity. Due to the in-plane anisotropy of ZnO/r-Al_2O_3 material system, it offers

another unique advantage as multi-mode SAW generation. Both Rayleigh and Love type SAW modes can be excited in ZnO/r-Al_2O_3 system, which enables the multi-mode sensing functions on a single chip.

1.2 Scope of Work

The objective of this research is to conduct the feasibility studies of implementing the acoustoelectric interaction in the versatile ZnO/$Mg_xZn_{1-x}O$ material system to realize novel multifunctional devices. Two types of the integrated SAW devices will be designed, fabricated and evaluated, including (1) ZnO based UV SAW device; (2) ZnO based multimode tunable SAW device. Meanwhile, the related processing techniques, the wet chemical and dry etching of ZnO, will be investigated and applied to the ZnO integrated SAW device fabrication. The scope of this study covers:

(i) Investigation of the wet chemical etching of ZnO film grown on r-Al_2O_3 substrate by MOCVD and the optimization of the processing conditions.

(ii) Investigation of the $SiCl_4$ based Reactive Ion Etching of ZnO and $Mg_xZn_{1-x}O$ film grown on r-Al_2O_3 substrate by MOCVD.

(iii) Design, fabrication and characterization of ZnO based UV SAW devices.

(iv) Design, fabrication and characterization of ZnO based multimode tunable SAW devices.

1.3 Organization of the Dissertation

After a brief introduction in Chapter 1, piezoelectricity and surface acoustic devices are reviewed in Chapter 2, along with the analysis of the acoustoelectric interaction

associated with the homogeneous bulk semiconductor and thin semiconducting layer. Chapter 2 also reviews the status of the devices studied in this work, including UV SAW devices and tunable SAW devices. At the end of Chapter 2, the material properties of ZnO and $Mg_xZn_{1-x}O$ are discussed. In Chapter 3, the investigation of the wet chemical etching and $SiCl_4$ based Reactive Ion Etching of ZnO and $Mg_xZn_{1-x}O$ thin film are presented with respect to the etch rate control, etch profile control and surface damage. In Chapter 4, the SAW characterization of the piezoelectric ZnO (Li doped) film grown by MOCVD on r-Al_2O_3 substrate is evaluated. The device structure, fabrication procedure and result analysis of a prototype ZnO based UV SAW device are presented. In Chapter 5, the sputtering and MOCVD hybrid growth technology is discussed targeting for the thick piezoelectric ZnO film growth. The structure of a prototype ZnO based multi-mode tunable SAW device, device performance and the comparison between the measured and simulated results are presented and discussed. Finally, Chapter 6 summarizes the accomplished tasks and proposes future investigations in the related areas.

Chapter 2. Technical Background

2.1 Piezoelectricity

In the design and application of surface acoustic wave (SAW) and bulk acoustic wave (BAW) devices, the piezoelectricity of materials is of the fundamental importance. Piezoelectricity is the phenomenon coupling elastic stresses and strains to electric fields and displacements, which was first discovered by Jacques and Pierre Curie in the 1880's during experiments on quartz. For a piezoelectric material, when an external stress is applied, an electrical charge is collected at its surface. Conversely, when a piezoelectric material is subjected to a voltage drop, it mechanically deforms. Piezoelectricity occurs only in anisotropic materials whose internal structure lacks a centre of symmetry. Piezoelectricity occurs in most non-centrosymmetric crystal classes but is often weak.

For general elastic materials, Hooke's Law describes the relation between the compressional stress T and strain S along the same axis as:

$$T = cS \tag{2.1}$$

where c is the elastic stiffness coefficient, also known as Young's modulus (N/m^2). In order to accommodate all possible components of stress and deformation, Eq. (2.1) needs to be expressed into a tensor equation:

$$(T) = (c) : (S) \tag{2.2}$$

Here (c) is referred to as a fourth-rank tensor and its components have four suffixes c_{jklm}, (T) and (S) are classed as second-rank tensors. Due to the symmetry of the crystal, tensor Eq. (2.2) can be reduced to a matrix equation [T] =[c] [S], so that the stress and strain matrix have only one suffix instead of two. The tensor components of T and S can be related to their matrix components as:

$$T_1=T_{11},\ T_2=T_{22},\ T_3=T_{33}$$

$$T_4=T_{32}=T_{23},\ \mathrm{T}_5=T_{31}=T_{13},\ T_6=T_{12}=T_{21}$$

$$S_1=S_{11},\ S_2=S_{22},\ S_3=S_{33}$$

$$S_4=2S_{32}=2S_{23},\ S_5=2S_{31}=2S_{13},\ S_6=2S_{12}=2S_{21} \tag{2.3}$$

In this way, the elastic stiffness constant is reduced to a 6×6 matrix [c]. Now, Hooke's Law becomes:

$$\begin{bmatrix} T_1 \\ T_2 \\ T_3 \\ T_4 \\ T_5 \\ T_6 \end{bmatrix} = \begin{bmatrix} c_{11} & c_{12} & c_{13} & c_{14} & c_{15} & c_{16} \\ c_{21} & c_{22} & c_{23} & c_{24} & c_{25} & c_{26} \\ c_{31} & c_{32} & c_{33} & c_{34} & c_{35} & c_{36} \\ c_{41} & c_{42} & c_{43} & c_{44} & c_{45} & c_{46} \\ c_{51} & c_{52} & c_{53} & c_{54} & c_{55} & c_{56} \\ c_{61} & c_{62} & c_{63} & c_{64} & c_{65} & c_{66} \end{bmatrix} \begin{bmatrix} S_1 \\ S_2 \\ S_3 \\ S_4 \\ S_5 \\ S_6 \end{bmatrix} \tag{2.4}$$

Because of the coupling between electrical and mechanical parameters, the simple version of Hooke's Law is not sufficient to describe the interaction in piezoelectric materials. By introducing the piezoelectric constant matrix [e] and electrical displacement density D, the general piezoelectric equations of state are given below:

$$[T]=[c][S]-[d][E] \tag{2.5}$$

$$[D]=[e][S]+[\varepsilon][E] \tag{2.6}$$

where [E] is the electric field intensity, [ε] is permittivity or dielectric constant of the material, which is measured at zero or constant strain. [e] is the piezoelectric constant for the material and [d] is the transpose of the piezoelectric constant [e]. Because the S term has six components, the dielectric permittivity [ε] is a 3×3 matrix with 9 elements and the piezoelectric constant terms in [e] will form a 3×6 matrix with 18 elements.

$$[e] = \begin{bmatrix} e_{11} & e_{21} & e_{31} \\ e_{12} & e_{22} & e_{32} \\ e_{13} & e_{23} & e_{33} \\ e_{14} & e_{24} & e_{34} \\ e_{15} & e_{25} & e_{35} \\ e_{16} & e_{26} & e_{36} \end{bmatrix} \tag{2.7}$$

The element values of [e] are dependent on the symmetry properties of the piezoelectric crystal.

In the piezoelectric material, one important parameter used to evaluate the piezoelectricity is the electromechanical coupling coefficient. Due to the additional potential energy stored in each unit cell, a piezoelectric material has an augmented elastic stiffness effect when compared to its non-piezoelectric counterpart. This stiffening increases the effective elastic stiffness coefficient by:

$$c_{stiffened} = c(1 + K^2) \tag{2.8}$$

where $K^2 = e^2 / c\varepsilon$ and c, e and ε are the elastic, piezoelectric and dielectric constants for the propagation direction of the acoustic wave in the solid. K^2 is defined as the electromechanical coupling coefficient, which is to measure of the efficiency of a given piezoelectric material in converting an electrical signal into the mechanical energy.

2.2 Surface Acoustic Wave Devices

Surface acoustic wave was first investigated by seismologists in the behavior study of various earthquake waves. In 1885, Lord Rayleigh demonstrated the existence of the basic type of surface acoustic waves. These are Rayleigh waves, involving wave motions confined to and propagating along the surface of the body. By 1911 a second type of

surface wave motion, produced in a bounded body with layered material properties, was characterized by Love and is hence named as Love wave. Rayleigh and Love waves are surface waves and resulted from the interaction of longitudinal and shear particle displacement with the boundary condition of the body. Figure 2.1 shows the possible particle displacements relative to the propagation direction. Surface acoustic waves have particle motion in at least two out of three directions of the Cartesian coordinate system. The generalized SAW has particle motion in the propagation direction and the two shear directions. The Rayleigh wave mode has both longitudinal and shear vertical particle displacement, while the Love wave mode has longitudinal and shear horizontal particle displacement. Figure 2.2 shows the sense of particle motions for Rayleigh and Love wave.

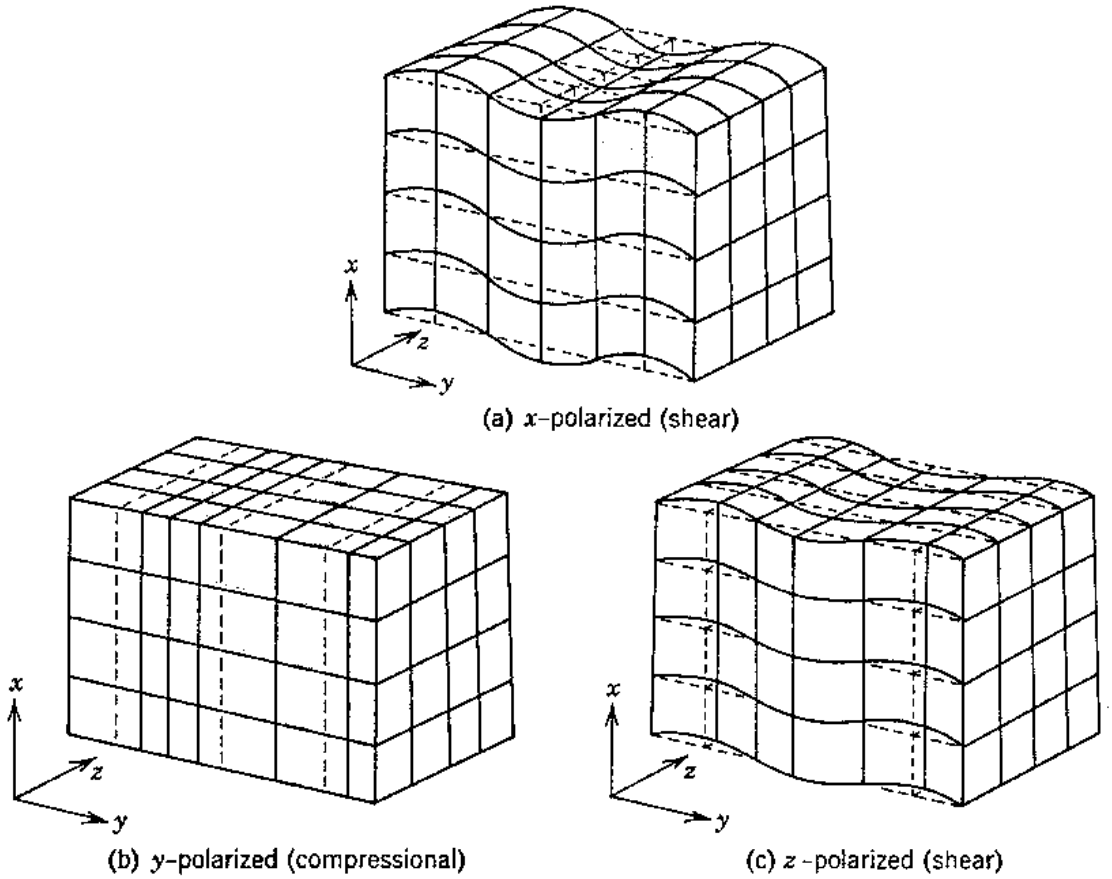

Figure 2.1. Acoustic wave propagation [1] (a) Shear vertical (SV); (b) longitudinal (compressional); (c) shear horizontal (SH).

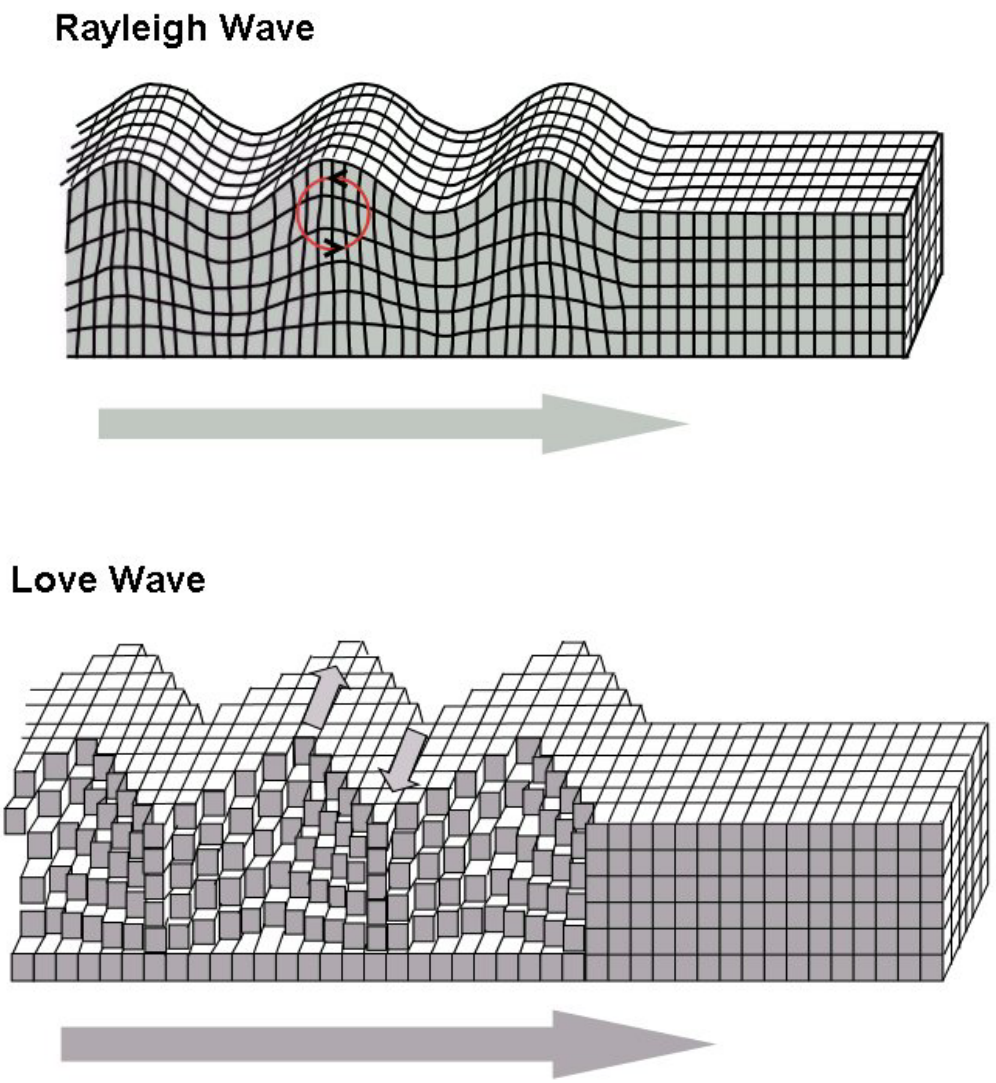

Figure 2.2. Schematic of the sense of particle motions of Rayleigh and Love wave [2]

In the layered system with various velocities, Love indicated that beside the Love wave, a Rayleigh-type wave could also exist. Further study of the layered Rayleigh wave showed that a series of higher order modes could exist in addition to the fundamental wave mode. Among these higher order mode, an important one is the first higher order mode M_{21} or Sezawa mode, which was first introduced by Sezawa (1927) [3]. Sezawa wave has larger velocity than basic Rayleigh wave and in certain layered system may have much higher electromechanical coupling coefficient, which is critically important to SAW device applications. The generation of the Sezawa wave mode in a dispersive material system will have a cutoff frequency and critical thickness/wavelength ratio.

Although piezoelectricity and surface acoustic wave in solid and layered structure have been introduced for long time, piezoelectric SAW devices were not well exploited until invention of the thin-film interdigital transducer (IDT) by White and Voltmer in 1965. The interdigital transducer becomes the key feature for all SAW devices, which supplies the most efficient method to generate and detect the SAW waves on piezoelectric surfaces. The simplest type of SAW device is a delay line employing two IDTs on top of a piezoelectric substrate, as shown in Figure 2.3. The input IDT converts signal voltage variations into mechanical acoustic waves and the output IDT converts mechanical SAW vibrations back into output voltages. Absorbers are sometimes used to absorb the spurious SAW transmissions.

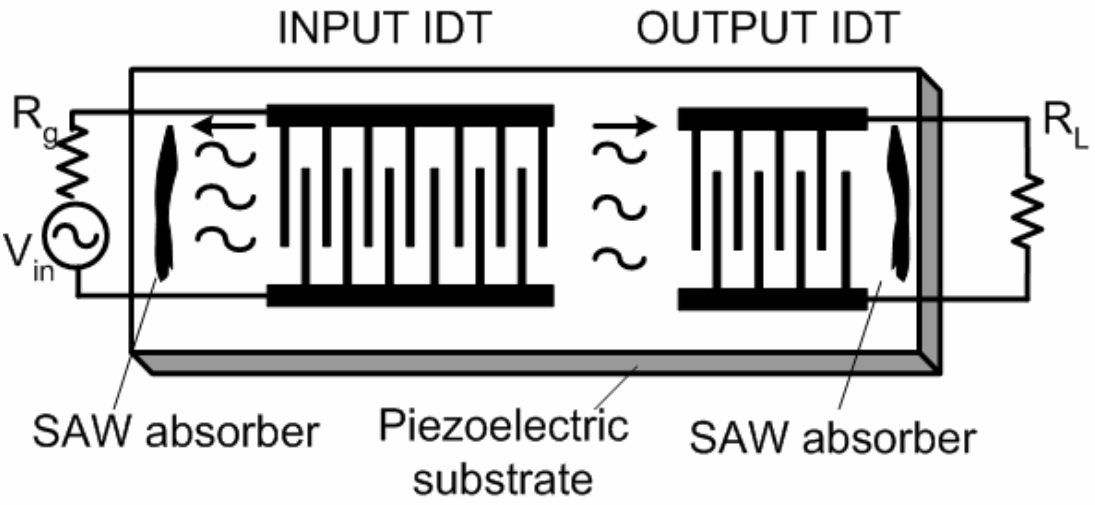

Figure 2.3. SAW delay line structure on the piezoelectric substrate

The IDT has a set of identical electrodes connected alternately to two metal bus-bars. The basic operation mechanism of the SAW devices is that when an AC voltage is applied to an input transducer, due to the piezoelectricity, the transducer produces periodical mechanical deformation of the piezoelectric substrate and generates mechanical wave. This mechanical wave propagates along the surface in both directions. After the mechanical wave reaches the receiving IDT, the mechanical energy will be converted back to a suitably filtered electrical signal due to the piezoelectricity of the substrate. By designing the superimposed thin metal input and output IDTs, SAW devices can provide desired bandpass filtering function $H(f) = V_{output}/V_{input}$, as the SAW propagates along the piezoelectric crystal surface. Quite complex signal processing functions can be realized within a single SAW package, such as various filters, delay lines, resonators and convolvers. SAW devices offer advantages as low power consumption, lightweight, functional versatility, and low cost. Compared to the digital signal processors, SAW-based processors are passive, hence with low power consumption. This is critical for most of the modern SAW applications, which involve portable wireless communications devices. Up to now, SAW devices found wide applications in analog signal processing for telecommunications, wireless passive RFID tags and recently sensors (chemical, biochemical torque, pressure mass and temperature, etc.).

In the design and application of SAW devices, the center frequency and 3dB bandwidth are the key parameters. For a SAW device, the basic relationship among acoustic velocity v_{saw}, center frequency f_c and wavelength λ is:

$$V_{SAW} = \lambda \cdot f_c \tag{2.9}$$

The wavelength λ is determined by the IDT electrode structure. The 3dB bandwidth of the passband is given by:

$$BW_{3dB} = 0.9 \cdot \frac{100}{N} \tag{2.10}$$

where N is the number of electrode pairs in the IDT. Another important SAW parameter is the temperature coefficient, which is dependent on the variation of the material volume and the acoustic velocity. It is a critical parameter for temperature stable applications, such as oscillators and chemical/biochemical sensors.

When the surface acoustic wave propagating along the surface of the piezoelectric substrate, there is accompanying electrical field and potential in addition to the mechanical deformation. This potential is not just confined to the piezoelectric surface. It also extends above or beneath the surface by a distance on the order of one acoustic wavelength [4]. The spatial variation of the potential at the piezoelectric surface produces electric fields in both the longitudinal and vertical directions. This effect is also called as piezoelectric stiffening, which means the material becomes stiffer because the same potential energy produces less deformation than in a non-piezoelectric material. When a perfect conductor is deposited on or put close to the piezoelectric surface, the longitudinal electrical field will be partially cancelled, space charge will accumulate on the conductor, the material becomes less "stiff" and the acoustic wave slows down. This effect is used to define the electromechanical coupling coefficient K^2 as a measure of the strength of the piezoelectricity of a given material. In Eq. (2.8) K^2 was defined in terms of piezoelectric parameters as $K^2 = e^2 / c\varepsilon$. This parameter may also be obtained experimentally as:

$$K^2 = \frac{-2\Delta v}{v} \tag{2.11}$$

where Δv is the SAW velocity difference between the metallized surface (short circuit) and free surface (open circuit) and v is the unperturbed SAW velocity (open circuit). Instead of the good conductor, when a semiconductor with finite conductivity is adjacent to the piezoelectric surface, it will not only modulate the wave velocity, but also generate an energy loss or attenuation for the surface wave due to the much longer time constant to redistribute the space charge. The variability of the conductivity of the semiconductor allows the continuous change of the SAW velocity and attenuation. By integrating this acoustoelectric interaction with the multi-functional ZnO material system, novel high efficiency electric and sensor devices can be realized.

2.3 Acoustoelectric Interaction

The interaction between the SAW and piezoelectric semiconductor has been investigated by several authors [5-11]. In the development of SAW devices, the acoustoelectric interaction has been used in the design of acoustoelectric amplifiers, SAW-based convolvers and correlators, and various SAW related charge coupled devices (CCD) for imaging, memory and signal processing etc.

2.3.1 Interaction of SAW and Piezoelectric Semiconductor with Homogeneous Bulk Conductivity

Although the basic equations used in acoustic wave analysis are generally written in tensor forms, the interaction between SAW and semiconductor with homogeneous bulk conductivity can be effectively discussed in terms of a one dimensional model. The basic equations of state that govern the propagation of acoustic wave in the piezoelectric

semiconducting medium connect the mechanical stress T and the electrical displacement D with the mechanical strain S and the electric field E. In one-dimensional form, these are:

$$T = cS - eE \tag{2.12}$$

$$D = eS + \varepsilon E \tag{2.13}$$

where c is the elastic constant at constant electric field, ε is the dielectric permittivity at constant strain, and e is the piezoelectric constant.

By considering acoustic wave propagation in the x direction of a piezoelectric semiconducting medium, by using

$$S = \frac{\partial u}{\partial x} \quad \text{and} \quad \frac{\partial T}{\partial x} = \rho \frac{\partial^2 u}{\partial t^2} \tag{2.14}$$

where u is the displacement amplitude in the x direction and ρ is the mass density, the one dimensional longitudinal wave equation is:

$$\rho \frac{\partial^2 u}{\partial t^2} = c\left(1 + \frac{e^2}{c\varepsilon}\right)\frac{\partial^2 u}{\partial x^2} - \frac{e}{\varepsilon}\frac{\partial D}{\partial x} \tag{2.15}$$

There are three cases of SAW propagation with respect to the homogeneous bulk conductivity of the semiconductor:

1) Conductivity is zero ($\sigma = 0$).

As the zero space charge condition, Poisson's equation requires the derivative of the displacement vector to be zero, as:

$$\frac{\partial D}{\partial x} = Q = 0 \tag{2.16}$$

From Eq.(2.15), the increased elastic constants will be:

$$c' = c\left(1 + \frac{e^2}{c\varepsilon}\right) \tag{2.17}$$

and thus acoustic velocity becomes:

$$v_o = \sqrt{\frac{c'}{\rho}} \tag{2.18}$$

This effect is defined as piezoelectric stiffening and is used to define the electromechanical coupling coefficient K^2 as a measure of strength of the piezoelectricity of a given material.

2) Conductivity is infinite ($\sigma = \infty$).

The very high conductivity implies that the internal electric field has to vanish. Thus, the electric stiffness is absent. The wave equation (2.15) reduces to:

$$\rho \frac{\partial^2 u}{\partial t^2} = c \frac{\partial^2 u}{\partial x^2} \tag{2.19}$$

which describes longitudinal sound wave in a medium appearing to be non-piezoelectric. The sound velocity is then:

$$v_o = \sqrt{\frac{c}{\rho}} \tag{2.20}$$

3) Limited conductivity ($0<\sigma<\infty$).

For the intermediate value of the conductivity, the wave is accompanied by D fields, currents, and varying space charge. The acoustoelectric interaction between the piezoelectric semiconductor and longitudinal electric field accompanying the SAW will has two effects on the acoustic wave. 1) The surface acoustic wave is attenuated due to ohmic losses; 2) The surface acoustic velocity is altered by the piezoelectric stiffening of the material. The propagation of the SAW in piezoelectric semiconductor with homogeneous bulk conductivity can be described with a frequency dependent relaxation-type model. The dispersion frequency is directly controlled by the bulk conductivity of

the material. The attenuation, Γ, and change in SAW velocity, $\Delta v/v_0$, in the case of a homogeneous piezoelectric semiconductor are [5]:

$$\frac{\Delta v}{v_0} = \frac{v - v_0}{v_0} = \frac{K^2}{2} \frac{1}{1 + (\omega_c / \omega)^2}$$

$$\Gamma = \frac{K^2}{2} k \frac{(\omega_c / \omega)}{1 + (\omega_c / \omega)^2} \tag{2.21}$$

where K^2 is the piezoelectric coupling coefficient and $k = \frac{\omega}{v_0}$ is the wave vector. ω_c is the conductivity relaxation frequency defined as:

$$\omega_c = \frac{\sigma}{\varepsilon_1 + \varepsilon_2} \tag{2.22}$$

where σ is the conductivity of the semiconductor, ε_1 and ε_2 are the dielectric constants of the piezoelectric substrate and the half-space above it, respectively [7].

2.3.2 Interaction of SAW and Thin Semiconducting Layer

In the case of a thin semiconducting layer system placed on the piezoelectric crystal's surface, the mobile carriers are confined to a conductive layer of thickness *d*, which is assumed to be much smaller than the wavelength of the SAW in the following analysis. The thin semiconducting layer can be either single layer semiconductor film or two dimensional electron gas (2DEG) formed by heterojunction, which supplies special advantage as the high electron mobility. The longitudinal electric field of the SAW can only be screened at the piezoelectric surface, i.e., z=0. The fact that here the conductivity is restricted to a thin sheet results effectively in a modification of the relaxation frequency ω_c, which is dependent on the SAW wave vector, $k = 2\pi/\lambda$ for homogeneous

semiconductor.

Because the electric field in the homogeneous bulk semiconductor decreases exponentially with the height (e^{-kz}), a layer of thickness 1/k effectively carries this current. For the thin semiconducting layer, the available thickness to carry the current is defined as *d*. Thus the effective resistance, and the time constant becomes 1/kd times larger:

$$\tau = \frac{\varepsilon_1 + \varepsilon_2}{\sigma \cdot kd} \tag{2.23}$$

and the conductivity relaxation frequency becomes:

$$\omega_c = \frac{kd \cdot \sigma}{\varepsilon_1 + \varepsilon_2} = \frac{\sigma_d k}{\varepsilon_1 + \varepsilon_2} \tag{2.24}$$

where $\sigma_d = \sigma \cdot d$ is the sheet conductivity of the thin film.

Thus, the ratio ω_c/ω in Eq. (2.21) becomes frequency independent

$$\frac{\omega_c}{\omega} = \frac{\frac{\sigma_d k}{\varepsilon_1 + \varepsilon_2}}{\omega} = \frac{\sigma_d}{\frac{\omega}{k}(\varepsilon_1 + \varepsilon_2)} = \frac{\sigma_d}{v_0(\varepsilon_1 + \varepsilon_2)} = \frac{\sigma_d}{\sigma_M} \tag{2.25}$$

where $\sigma_M = v_0 (\varepsilon_1 + \varepsilon_2)$, is the conductivity, at which the maximum loss occurs.

Now Eq. (2.21) becomes:

$$\frac{\Delta v}{v_0} = \frac{v - v_0}{v_0} = \frac{K^2}{2} \frac{1}{1 + (\sigma_d / \sigma_M)^2} \tag{2.26}$$

$$\Gamma = \frac{K^2}{2} k \frac{(\sigma_d / \sigma_M)}{1 + (\sigma_d / \sigma_M)^2}$$

Figure 2.4 (a) and (b) illustrate Eq.(2.26), i.e., (a) the relative change $\Delta v/v_0 = (v - v_0)/v_0$ of the sound velocity; (b) the attenuation Γ per unit length, as function of the sheet conductivity of the thin semiconducting layer.

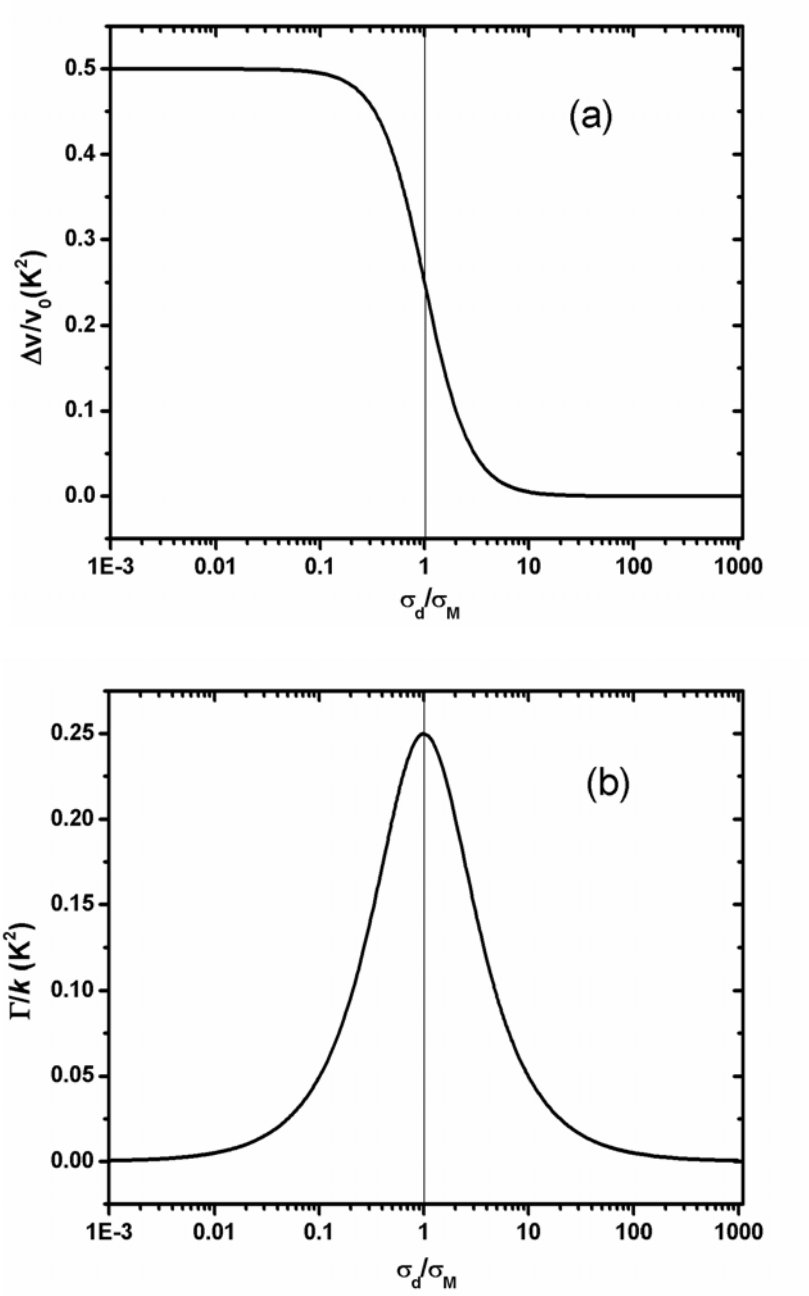

Figure 2.4. Change in sound velocity $\Delta v/v_0$ (a) and attenuation coefficient per unit wave vector k (b) in units of effective coupling coefficient K^2 as a function of the ratio σ_d/σ_M. The thin conducting layer is assumed to be located on top of the piezoelectric surface.

2.4 UV SAW Devices

The ultraviolet (UV) light photodetectors have been extensively studied for years, as they have wide applications in the UV astronomy, flame detection, UV radiation dosimetry, early missile threat warning, and chemical/biochemical reagent detectors. For solid-state UV photodetectors, various materials have been used, such as Si, GaAs, SiC, GaN, $Al_xGa_{1-x}N$, ZnO and $Mg_xZn_{1-x}O$. The basic device structures of current solid-state UV photodetectors include: 1) photoconductors; 2) Schottky metal-semiconductor-metal (MSM) detectors; 3) Schottky barrier photodiodes; 4) p-i-n photodiodes; 5) Avalanche photodiodes; and 6) Focal plane arrays [12]. These structures have been designed to fulfill various UV detection requirements, such as detection speed, sensitivity, bias, quantum efficiency, and fabrication simplicity. However, most of these UV photodetectors need either voltage or current to drive. As a result, the direct wire connection and additional power supply become necessary. In order to construct zero-power and wireless UV detector for distributed sensor network, several UV SAW photodetectors have been proposed to integrate the UV sensing function and SAW technology based on the acoustoelectric interaction [13-20]. In the UV SAW photodetectors, the UV sensitive semiconductor layer is integrated on, or in, the SAW device. The incident light will be absorbed by the semiconductor and generate electron-hole pairs. These free carriers in the semiconductor layer will interact with the electric field accompanying the propagating SAW, resulting in an increased insertion loss. Additionally, a velocity reduction will occur due to the piezoelectric stiffening, resulting in a phase shift and time delay across the SAW device. Both the attenuation and phase changes can be used as the sensing information. Beside the sensitivity issue, the UV SAW

photodetectors offer important features as passive (no power supply necessary) and RF readout (for wireless communication).

Recently, several UV SAW photodetectors have been proposed and demonstrated with various piezoelectric and UV sensing layer integration. GaN based UV SAW devices were demonstrated by using MOCVD grown GaN on c-plane sapphire substrates [13-17]. In these devices, GaN, which is a weakly piezoelectric wide bandgap semiconductor, was used for both SAW excitation and UV sensing. A GaN-based SAW UV detector was reported to cause a 60 kHz oscillation frequency shift at 221.3 MHz when used as a delay element in the feedback path of an oscillator. The estimated electromechanical coupling coefficient K^2 is ~0.055% and the achieved relative oscillation frequency shift is 271 ppm. The maximum response was observed at the optical wavelength of 365 nm, which corresponds to the photon energy equals to the band gap width of GaN 3.4eV [14]. In an alternative configuration, a SAW launched from an input interdigital transducer (IDT) was used to sweep electron-hole pairs generated in the sensing area to an MSM photoconductive detector out of the sensing region [15]. The schematic experiment setup is shown in Figure 2.5. The responsivity of this MSM photodetector was reported to be a function of the frequency and power of the SAW.

Based on the acoustoelectric interaction, the coupling coefficient K^2 is the key factor to influence the change of velocity and attenuation. A higher K^2 is desirable for the larger acoustoelectric effect and hence the high sensitivity. A hybrid ZnO/$LiNbO_3$ SAW UV photodetector was also reported, for better piezoelectric coupling [19]. The $LiNbO_3$ substrate was used for SAW excitation, while the unbalanced RF magnetron sputtering deposited ZnO film was used as the photosensitive layer. This device was reported to

exhibit a frequency shift of 170 kHz at 37 MHz, for a UV light intensity of 40 mW/cm^2. The wavelength of the UV light is of 365 nm. In order the enhance the UV sensitivity, a hybrid ZnO/$LiNbO_3$ UV SAW photodetector was reported with thinner ZnO thickness (71 nm) to minimize the influence of the mass loading [20]. The UV SAW photodetector was connected in the feedback loop to form an oscillator. The UV sensitivity was evaluated by both the oscillation voltage amplitude and frequency shift. For the amplitude measurement, the UV sensitivity was depended on the power supply V_{cc} of the oscillator circuit and an oscillation quench was observed with a higher UV light intensity. The voltage responsivity is reported to be ~24 kV W^{-1}, which is better than the results from [19]. For the frequency evaluation, there was ~28 kHz oscillation frequency (f_o=35.4 MHz) down shift when UV illumination (~34 μW cm^{-2}) was chopped after 5s.

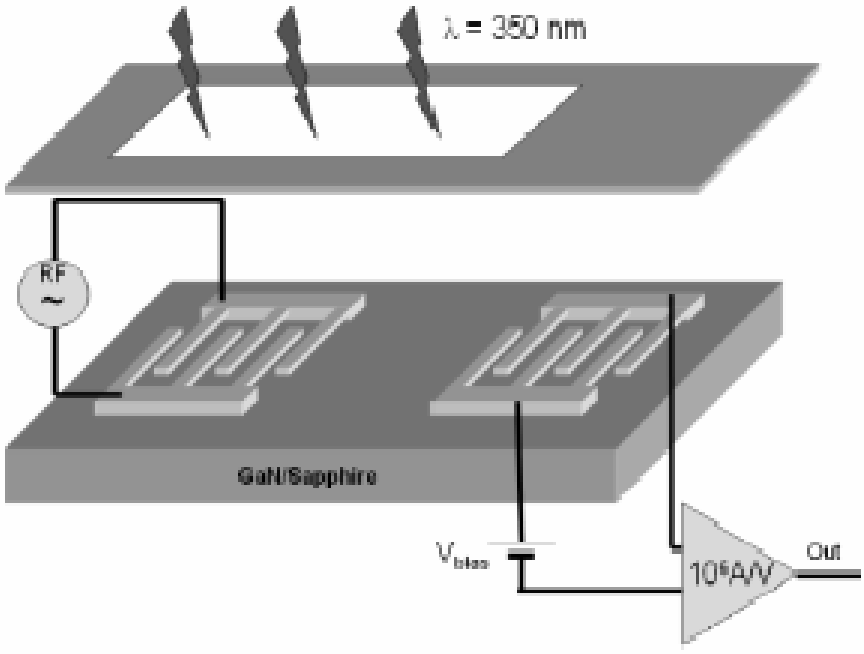

Figure 2.5. Schematic experiment setup for the integration of SAW generator and a UV photodetector [15].

2.5 Tunable SAW Devices

Another important application example of the acoustoelectric interaction in the communication and sensing is the tunable SAW devices. For traditional SAW device, the acoustic velocity and frequency are un-adjustable because after the fabrication, metal patterns, such as IDT fingers, and the delay line length is fixed. However, such tunability is critically important in many applications, such as advanced communication receivers, as it enhances filter flexibility and allows adaptive signal processing, and tunable sensors. The tunable SAW device can be inserted to the feed back loop to form a voltage-controlled oscillator (VCO) without additional phase shifter. Tunable SAW delay lines can also be used in various analog signal processing circuits, for example in radar applications. As a SAW sensor component, the tunable SAW sensor can improve the sensitivity and selectivity of the sensing, extend the lifetime by "resetting" the sensor velocity range. The tunable SAW device can also be used as adjustable RF ID tag for wireless identification.

Great efforts have been involved to realize practically usable tunable SAW devices. The proposed approaches mainly include three categories based on the operation mechanisms, including filter banks with selectable filters [21-23], perturbation of piezoelectric material properties [24-31], and perturbation of SAW propagating boundary conditions [32-41]. In the first approach, the responses of a number of IDTs, placed either in series or parallel, are combined to achieve the desired time delay or frequency spectrum [21, 22]. RF or mechanical switches have been used to select the suitable filter channel. Figure 2.6 shows the schematic diagram of the tunable SAW device with RF switch [22]. A mechanical switch approach, as shown in Figure 2.7, has also been

reported, in which the channel SAW filters in the separate package are located sequentially in an imaginary cylinder and on the ribs in the radial planes passing through a symmetry axis of this cylinder [23]. However, there are several major drawbacks of filter bank approaches: 1) the tuning of the time delay and frequency is not continuous; 2) the dimension of the device is large, such as the device reported in [23], which has the dimension of 55 $\times$15 mm^2. These drawbacks make the filter bank based tunable SAW filters impractical for a number of applications which require miniaturized components, such as cellular phones or wireless sensors.

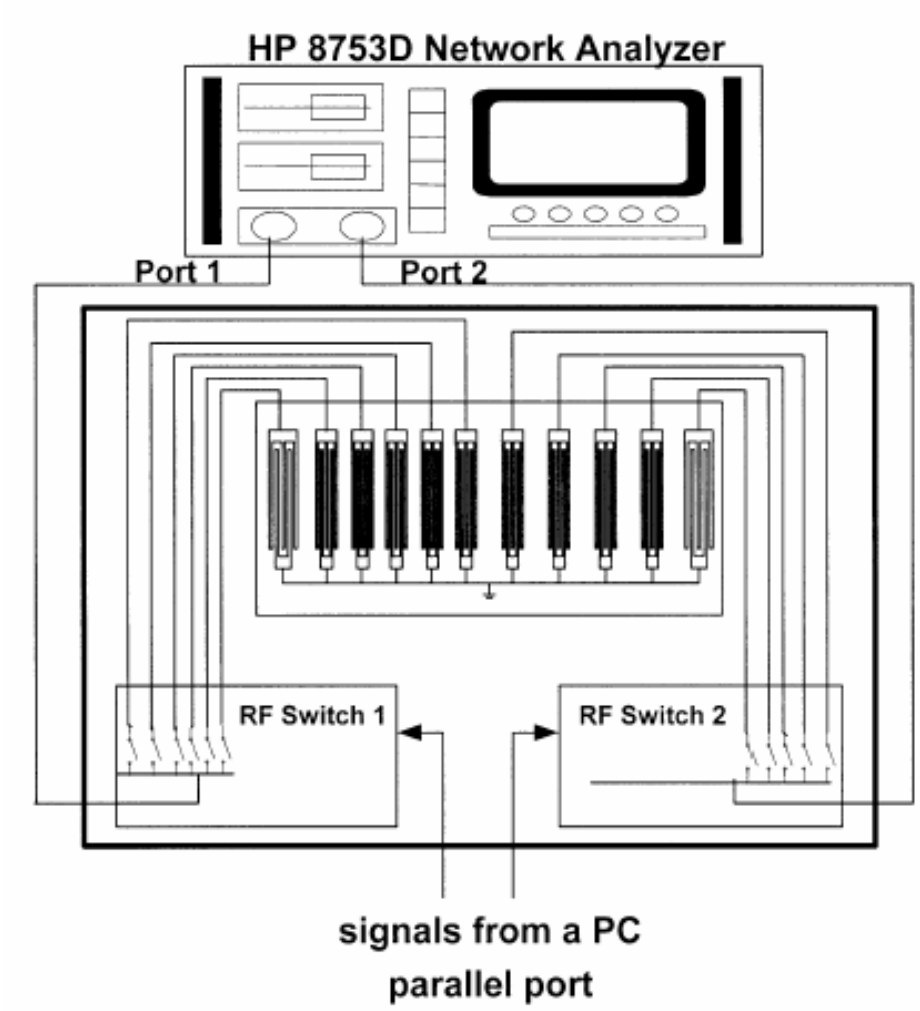

Figure 2.6. Schematic diagram of the tunable SAW device with RF switches [22]

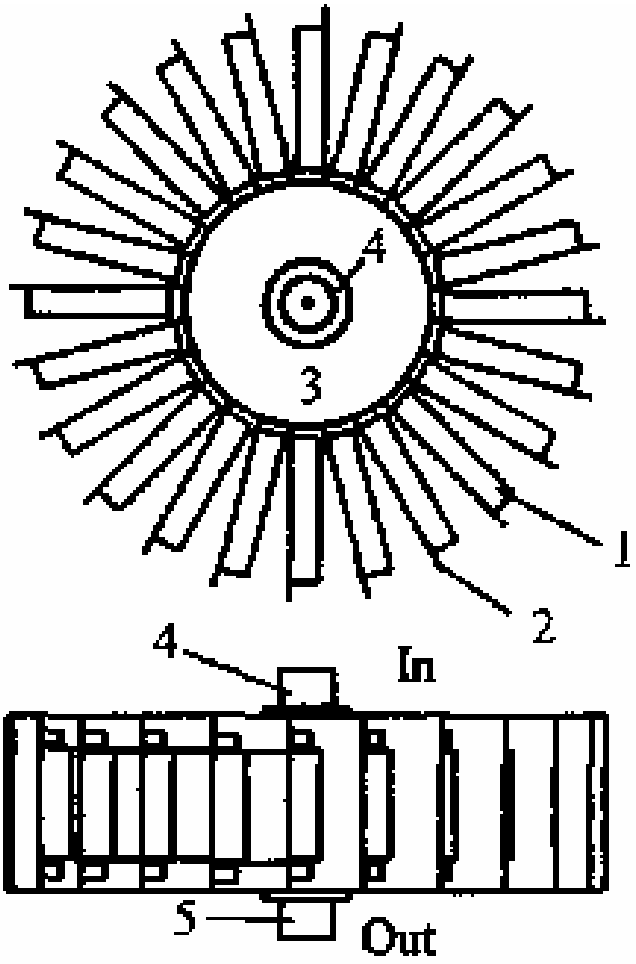

Figure 2.7. 3-D construction of the tunable SAW device with mechanical switch [23]

In the second approach, either DC bias or magnetic field was applied to the piezoelectric material directly or magnetostrictive material adjacent to the piezo-substrate to adjust the material stiffness and then SAW propagating properties. For example, a tunable SAW oscillator was proposed [25] with the normal field configuration on x-cut quartz, in which two electrodes deposited on the upper and lower surface of the SAW propagation medium. DC bias was applied to the medium through these two electrodes to adjust the effective stiffness coefficients of the material. In such a device, a voltage as high as 5.5 kV was needed to achieve a 12kHz oscillation frequency shift at the center frequency of 59.08 MHz, corresponding to a tuning range of only 0.02%. Obviously, this high bias is highly incompatible with most applications. Another proposed device used the in-plane filed configuration, which located the two electrodes beside the SAW propagation path or delay line on various $LiNbO_3$ substrates [26]. Although the operation frequency increased up to ~800 MHz, the velocity tuning rang is still very small. For example, a $\Delta v/v$ of $15x10^{-8}$ V^{-1} was reported for the in-plane configuration, and a comparable $\Delta v/v$ of $33x10^{-8}$ V^{-1} for the normal field configuration. It requires voltages on the order of 6 kV to achieve 0.1% velocity tunability.

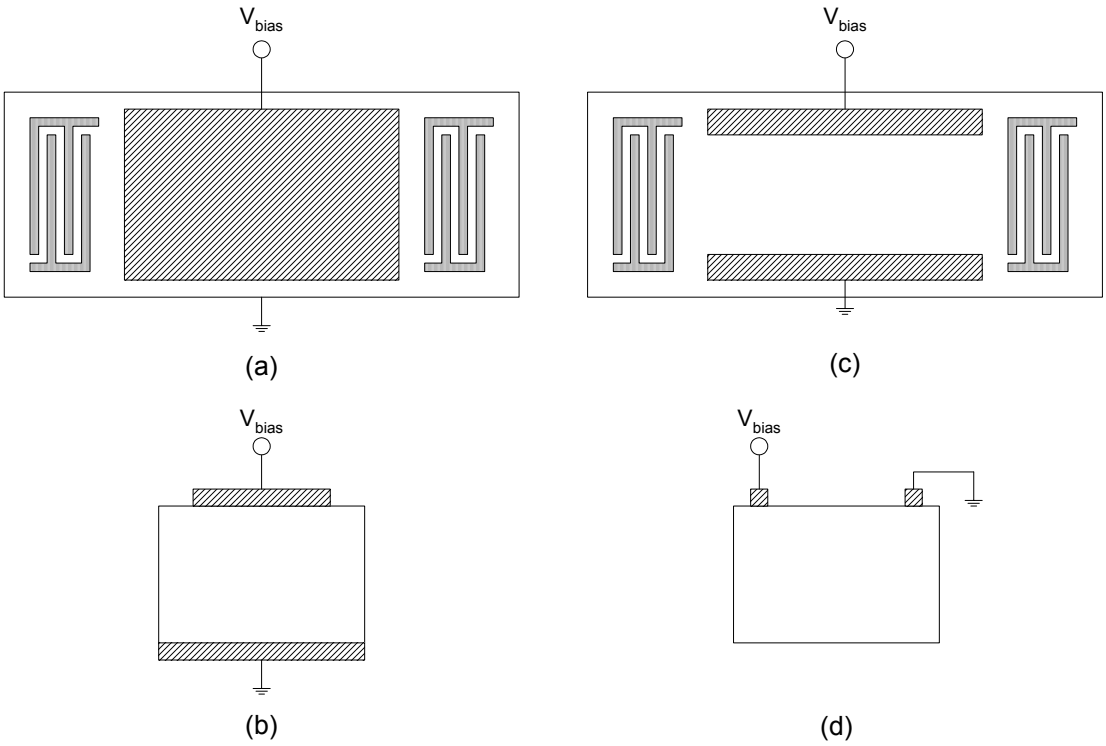

Figure 2.8. Tunable SAW device configurations using an electrical field to vary the effective stiffness constants of the piezoelectric material: (a) normal field top view; (b) normal field side view; (c) in-plane field top view; and (d) in-plane field side view.

Beside the application of DC bias to adjust the material effective stiffness, the magnetic field dependence of the stiffness coefficients in a magnetostrictive material was also proposed to realize the tunable SAW devices [28-31]. Compared to electrical field configuration, the reported magnetic field depended tunable SAW devices had relative larger velocity tunability. However, the requirement of additional magnetic field generation equipment makes this kind of devices not suitable to portable or mobile applications.

In comparison to the first two approaches, the perturbation of the electrical boundary condition based on the acoustoelectric interaction is more practical to realize tunable SAW device with low bias, large tunability range, continuously tuning and small dimension. In the device operation, the effective coupling coefficient K^2 is the key factor. The perturbation of the electrical boundary condition can be realized by either current flow control or charge control. The current flow control mechanism was proposed in the design of piezoelectric acoustic amplifier or SAW delay line amplifier based on the acoustoelectric interaction [32-34]. By applying DC bias to the semiconducting medium adjacent to the piezoelectric substrate, amplification gain could be achieved when the carrier drift velocity v_d exceeds the phase velocity v_p. In this design, the external DC electric field is aligned in the same direction of the propagating SAW. For charge control mechanism, there is no drift current inside the semiconductor. The total power consumption is reduced. The velocity tunability is realized through the control of the free carrier density in the semiconducting medium by forming either depletion or accumulation layer. Metal-insulator-semiconductor (MIS) and metal-semiconductor (MS) schottky diode (normal or in plane) configurations were proposed in the device design

[35-37]. J. D. Crowley *et al.* proposed a voltage tunable SAW device with a Si/Air gap/$LiNbO_3$ vertical structure and SiO_2 was used as the spacer [35]. DC and pulse bias was applied to the electrode on top of the silicon and the ground electrode beneath the $LiNbO_3$ to from the depletion or accumulation layer in the silicon. The center frequency of the SAW was 230MHz. For a device with 12mm long Si bar, at +30V pulse voltage, the reported phase shift of the device was 180 ^{o}, corresponding to a 0.06% relative velocity change. T. W. Grudkowski *et al.* reported another configuration by integrating the GaAs SAW and lateral Schottky barrier diode at the delay line region [36]. With an electrode length of 10mm, the maximum velocity change was reported to be 0.0575% with a –60V reverse bias. In order to investigate the silicon IC compatibility, S. Urabe investigated the velocity tunability of the device with a metal-zinc oxide-oxide-silicon (MZOS) structure [37]. After the thermal growth of 100nm SiO_2 layer on top of the n-type Si wafer, a 1.0 μm ZnO film was fabricated using an rf-sputtering system with hemispherical configuration. Aluminum IDT and top electrode were fabricated on the top ZnO surface. Another ohmic electrode was deposited on the bottom surface of the n-Si wafer. DC bias was applied to the structure and depletion layer was formed in the n-Si. The length of the top electrode is 4mm. The schematic of the prototype MOZS SAW phase shifter is shown in Figure 2.9. The maximum phase shift of the device is 67 ^{o} at –5V bias, corresponding to a relative variation of 0.085%. Further increase of the bias will make the device into strong inversion and surface charge polarity change. The phase shift tends to zero, and the attenuation due to minority charge carriers is large. By comparing these reported results, it can be seen the velocity tuning ranges are rather small, mainly in the ppm level.

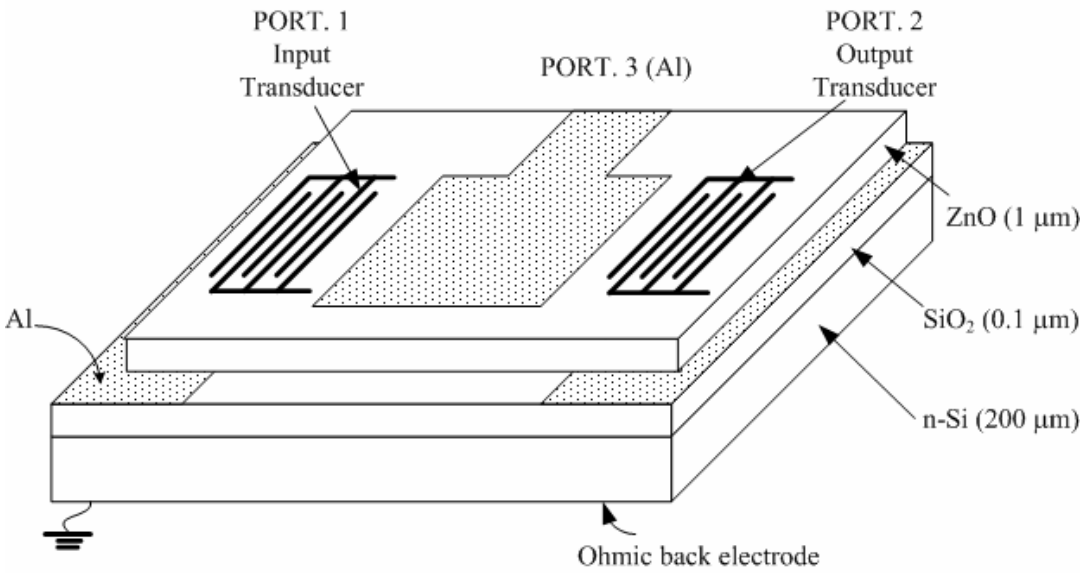

Figure 2.9. Schematic of the experimental MZOS SAW phase shifter [37]

An improved result is reported using a two dimensional electron system (2DEG) to tune the acoustic velocity [38-41]. The first demonstration of 2DEG tunable surface acoustic waves used the GaAs/ $Al_xGa_{1-x}As$ system, where the GaAs substrate was used as a piezoelectric medium, and the 2DEG was formed in the $Al_xGa_{1-x}As$ quantum well [40]. Due to the small coupling of the GaAs (k^2_{GaAs}< 0.06%), the reported tunability range was <0.1%. The better version of the 2DEG tunable SAW device was reported by the same group which integrates the GaAs/ $Al_xGa_{1-x}As$ quantum well (QW) with $LiNbO_3$ substrate [41]. The QW was epitaxially lifted off, and bonded to the $LiNbO_3$ substrate using Van der Waals forces. The effective coupling coefficient of this hybrid structure was reported to be 3.5%, with a velocity tunability of 0.5%. However, the epitaxial lift-off and Van der Waals bonding technologies are very complicated with low yields, poor reliability and high expenses; therefore, unsuitable for commercial applications.

Tunable SAW devices have wide applications in advanced communication systems and chemical/biochemical sensors. The tunable SAW device can be inserted into the feed back loop of an oscillator to form a SAW VCO. VCO is one of the principal components in transmitter and receiver systems. Tunable SAW devices can be implemented into adaptive filters, which are necessary in many wireless sensors and communications applications, where the signal may shift frequency to adapt to environmental factors such as multipath interference, and to avoid interception by a third party. Tunable SAW devices are attractive platforms for chemical and biochemical sensing, by improving the sensors' sensitivity, selectivity and lengthening the SAW sensor lifetime by "resetting" the sensor velocity range.

2.6 ZnO and $Mg_xZn_{1-x}O$ related properties

As a direct wide bandgap semiconductor, ZnO (E_g ~ 3.3 eV at 300*K*) has attracted increasing attention in potential blue and UV optoelectronic applications. Because of its large exciton binding energy (~ 60meV), which is 2.4 times the thermal energy at room temperature, the excitonic emission mechanisms are significant at temperatures even above room temperature. ZnO is a II-VI compound semiconductor whose ionicity resides at the borderline between covalent and ionic semiconductor. ZnO crystals commonly exhibit a wurtzite structure (hexagonal symmetry) or a zincblende structure, with c=5.2069Å and a=3.2495Å. Compared to another popular wide bandgap semiconductor GaN (~3.4eV at 300*K*), ZnO offers advantages as 1) more efficient optical emission and detection [42], 2) better radiation resistance [43, 44], 3) ZnO has commercially available native substrate, 4) simpler growth technology and lower cost for devices, 5) wet chemical processing is feasible; 6) epitaxial films can be grown at low temperature (<400 ^oC). Because of the small lattice mismatch, ZnO has been used as the buffer layer to grow high quality GaN film [45, 46]. GaN films grown on high quality ZnO buffer layers have been observed to have better structural properties compared to GaN films grown on sapphire and SiC. Compared conventional Si based photosensitive devices, ZnO possesses excellent optical properties for high sensitive UV detection [47-51]. ZnO is inherently visible blind. The wide bandgap promises a low dark current in the photodiode, reducing the need of a cooling system. The large photoresponse leads to high quantum efficiency and low bias voltage. ZnO can be alloyed with CdO and MgO to form the ternary compounds, extending the direct energy band 2.8eV to 3.3 eV and 3.3eV to 4eV. Such properties eliminate the needs for bulky blocking filters, dramatically simplifying

the optical system design. By tailoring the energy bandgap, ZnO based photodetectors can used to detect radiations ranging from UVA (315-400nm), to UVB (280-315nm) and UVC (200-280nm). Optically pumped laser emission has been observed in ZnO films deposited by plasma enhanced MBE on sapphire [52]. This opens up the possibility of developing UV lasers from ZnO films.

Beside the excellent optical properties, ZnO is also known as a piezoelectric material with high electromechanical coupling coefficients for years. ZnO has been used as a piezoelectric material in bulk acoustic wave (BAW) and surface acoustic wave (SAW) delay lines, filters, and resonators in wireless communication and sensors. ZnO thin films have been used in conjunction with low loss high acoustic velocity substrates, such as sapphire (Al_2O_3) and diamond; with semiconductors, such as Si, GaAs, and InP; and with low coupling coefficient piezoelectric materials, such as quartz.

The as-grown ZnO film is usually n-type semiconductor, due to crystal defects [53, 54]. Through proper doping, ZnO film can be made from highly conductive to highly insulating, transparent, ferroelectric and piezoelectric, and ferromagnetic. ZnO based transparent conductive oxides can be realized by Al and Ga doping, which can be used as transparent electrode in the field of photovoltaic solar energy conversion [55, 56]. Compensation doping using Li, Ni and Cu has been used to achieve insulating ZnO films for piezoelectric applications [57-59]. In-situ N doping, Ga : N and Ga : As co-doping have been reported to achieve p-type ZnO [60-62]. Various transition metals (TM), such as V, Co, Mn and Fe, have been reported to dope into ZnO and realize the diluted magnetic semiconductor for novel spin-electronics applications [63-67].

Alloying ZnO with MgO (E_g ~ 7.7eV) forms $Mg_xZn_{1-x}O$, extending the direct energy band gap from 3.3 eV (ZnO) to ~4.0 eV ($Mg_{0.33}Zn_{0.67}O$). The range of direct band gap energies obtainable is limited by the solubility limit of MgO in ZnO. According to the phase diagram of the ZnO–MgO binary system, the thermodynamic solid solubility of MgO in ZnO is less than 4 mol % [68]. In addition, MgO has a NaCl-type structure, which consists of interpenetrating face centered cubic (f.c.c) Mg and O sub-lattices, while ZnO has a wurtzite structure, which consists of interpenetrating hexagonal close packed (h.c.p) Zn and O sub-lattices. Several deposition methods have been used to grown $Mg_xZn_{1-x}O$ films with Mg content up to 33%, including sputtering, pulsed laser deposition, MOCVD, metal organic chemical vapor phase epitaxy (MOVPE) and laser-assisted molecular beam epitaxial (MBE) [69-71]. It has been found that MgO segregates in the wurtzite MgZnO lattice above 33% of Mg content and further increase of the Mg content will result in $Mg_xZn_{1-x}O$ films into metastable cubic. The 0.85 eV bandgap offset (x=36%) between $Mg_xZn_{1-x}O$ and ZnO indicates that $Mg_xZn_{1-x}O$ is a suitable barrier layer in $Mg_xZn_{1-x}O$/ZnO heterostructure. The electronic and optical properties of $Mg_xZn_{1-x}O$ can be tuned by adjusting the Mg composition x in the ternary compound. These properties make $Mg_xZn_{1-x}O$ a promising candidate for solar blind UV photodetectors. $Mg_xZn_{1-x}O$/ZnO heterostructure has wide potential applications, such as UV lasing and heterostructure field effect transistor (HFET) devices. Integrating the $Mg_xZn_{1-x}O$/ZnO heterostructure with SAW technology may realize high efficiency tunable SAW device based on the acoustoelectric interaction, which offers low bias and large tuning range. Some important material properties of ZnO are listed in table 2.1 below.

Table 2.1 Important material properties of ZnO

Crystal class	Wurtzite (hexagonal)
Lattice parameters [Å]	a = 3.2498 ; c = 5.20661
Energy bandgap	~3.32 eV at room temperature
Dielectric constants (constant strain)	ε_{11} = 8.55 ; ε_{33} = 10.2
Piezoelectric stress constants [C/m^2]	e_{15} = -0.48 ; e_{31} = -0.573 ; e_{33} = 1.32

2.7 Summary

The scope of this thesis work is to develop integrated multifunctional ZnO SAW devices based on the acoustoelectric interaction. Traditional SAW devices have found wide applications in telecommunications and sensors. However, they lack tunability of acoustic velocity, which is critically important in many applications, such as adaptive communications and tunable sensors. Different approaches have been proposed to achieve the tunability of SAW devices with their special advantages and disadvantages. The acoustoelectric interaction between the adjacent free carriers and SAW supplies an efficient way to impact the SAW propagation properties and realize acoustic tunability. In addition, the implementation of the acoustoelectric interaction will extend the functionality of the SAW device and generate novel electronic and sensing devices.

As a versatile material, ZnO shows multiple functionalities and supplies the fundament for multifunctional device integration based on the acoustoelectric interaction. To fulfill the device fabrication requirements, we will investigate the wet and dry etching of ZnO films grown on r-Al_2O_3 substrate. In this dissertation, we will investigate the feasibilities to fabricate two types of integrated SAW devices based on the acoustoelectric interaction. A novel ZnO based UV SAW device will be investigated, in which the UV

sensing function of ZnO film will be integrated to the SAW technology. In comparison to the traditional UV detectors, the ZnO UV SAW device is passive and enables the output in frequency domain, suitable for wireless sensor network. In this dissertation work another integrated multifunctional device, the ZnO based multimode tunable SAW device, will be demonstrated. The acoustic velocity tunability is achieved by changing the sheet conductivity of the semiconducting channel through the gate biasing. The ZnO based tunable SAW devices are expected to find broad applications in communications, as well as in chemical/biochemical sensing.

Chapter 3. ZnO Processing Technology – Wet and Dry etching

In the development of ZnO tunable SAW devices, various semiconductor processing techniques are involved, such as etching, diffusion and Schottky/ohmic contact, etc. Based on the device design, the ZnO tunable SAW devices are constructed with a semiconducting ZnO/ piezoelectric ZnO multilayer structure on r-Al_2O_3 substrates. The etching process is of critical importance to the device fabrication and device performance. Beside the function of forming and delineating patterns accurately, there are special etching requirements in the tunable SAW device fabrication, including 1) The ZnO etching rate needs to be controllable to make good ohmic contract to the semiconducting ZnO layer and to avoid over etch the piezoelectric ZnO layer; 2) the etched surface need to be smooth and less surface damage to achieve good metal contact, IDT fabrication and SAW response; 3) to isolate the cross-talk between each device, mesa etching to the substrate is desired for thick ZnO films (~2.0 μm). The mesa etching of the thick ZnO layer requires steep sidewall and less lateral pattern shrink for compact device design.

Similar as other semiconductors, wet chemical and dry etching technologies has been applied to ZnO, with the consideration of their special advantages and disadvantages. In order to fulfill the requirement of ZnO tunable device fabrication, investigation of both the wet chemical etching and dry etching of ZnO and $Mg_xZn_{1-x}O$ films grown by MOCVD on r-Al_2O_3 substrate has been conducted. The processing optimization has been carried out to generate controllable etch rate, steep etch sidewall, smooth etched surface and less surface damage. The developed ZnO etching processes have been successfully applied to the prototype ZnO tunable SAW device fabrication.

3.1 ZnO and $Mg_xZn_{1-x}O$ Films Grown by MOCVD on r-Al_2O_3 Substrate

Epitaxial ZnO and $Mg_xZn_{1-x}O$ ($0 \leq x \leq 0.35$) films grown by MOCVD on r-Al_2O_3 substrates were used in this etching study [72-74]. In the MOCVD growth, diethyl zinc (DEZn) and oxygen (O_2) are the precursors for ZnO growth. $(MCP)_2$ Mg is the precursor used for alloying ZnO with Mg. The Zn and Mg vapors are introduced onto the rotating substrate in the vacuum chamber, using argon (Ar) as the carrier gas flowing through the bubblers. The oxidizer O_2 is introduced through a separate line into the chamber to avoid the gas phase reaction before deposition. The substrate temperature was maintained at 400-500^oC.

The substrate used in our work is r-plane sapphire (Al_2O_3). The use of r-Al_2O_3 substrate offers following three advantages targeting for ZnO tunable SAW devices: 1) the c-axis of the ZnO film is in-plane, resulting in unique anisotropic acoustic properties, which can be used for multi-mode SAW generation; 2) the system has higher electromechanical coupling coefficients, k^2, up to 6% for certain wave modes. The high coupling coefficient is critically important for applications based on acoustoelectric interaction; 3) lattice mismatch between ZnO and r-Al_2O_3 is less than that in ZnO/c-Al_2O_3, resulting in high quality ZnO thin films.

The quality of the films was characterized using a Leo-Zeiss field emission electron microscope (FESEM), high-resolution x-ray diffraction (XRD) θ-2θ scan. Figure 3.1 shows FESEM image of the MOCVD grown ZnO on r-plane Al_2O_3. The as-grown film is dense and uniform. Figure 3.2 shows the θ-2θ scan of x-ray diffraction pattern of the MOCVD grown ZnO film on r- Al_2O_3 with full width half maximum (FWHM) 0.12 degree. The epitaxial relationships between ZnO and r-plane sapphire were determined to

be $(11\bar{2}0)$ ZnO|| $(0\bar{1}12)$ Al_2O_3, and [0001] ZnO|| $[0\bar{1}11]$ Al_2O_3. The MOCVD grown $Mg_xZn_{1-x}O$ ($0<x<0.33$) films on r-Al_2O_3 substrate were characterized by using FESEM, XRD, Rutherford backscattering spectrometry (RBS) and optical transmission. Figure 3.3 shows the FESEM image of the MOCVD grown $Mg_xZn_{1-x}O$ (x=0.2) film on r-Al_2O_3 substrate. Figure 3.4 shows the x-ray θ-2θ scan of the MOCVD grown $Mg_xZn_{1-x}O$ (x=0.2) film on r-Al_2O_3 with FWHM of 0.28 degree. The epitaxial relationships between $Mg_xZn_{1-x}O$ and r- Al_2O_3 are determined to be $(11\bar{2}0)$ $Mg_xZn_{1-x}O$ || $(0\bar{1}12)$ Al_2O_3, and [0001] $Mg_xZn_{1-x}O$ || $[0\bar{1}11]$ Al_2O_3. The composition of the as grown $Mg_xZn_{1-x}O$ films was analyzed by Rutherford Back Scattering (RBS) method. Figure 3.5 shows the RBS spectrum of a $Mg_xZn_{1-x}O$ film. The dotted line is the experimental data and the solid line presents simulation results of $Mg_{0.26}Zn_{0.74}O$ film. It can be seen that the experimental data fit well with the simulated profiles. The $Mg_xZn_{1-x}O$ film was thus determined to be $Mg_{0.26}Zn_{0.74}O$. Figure 3.7 shows the optical transmission spectra for ZnO, $Mg_xZn_{1-x}O$ films with different x values. The progressive blue shift with increasing Mg content is evident.

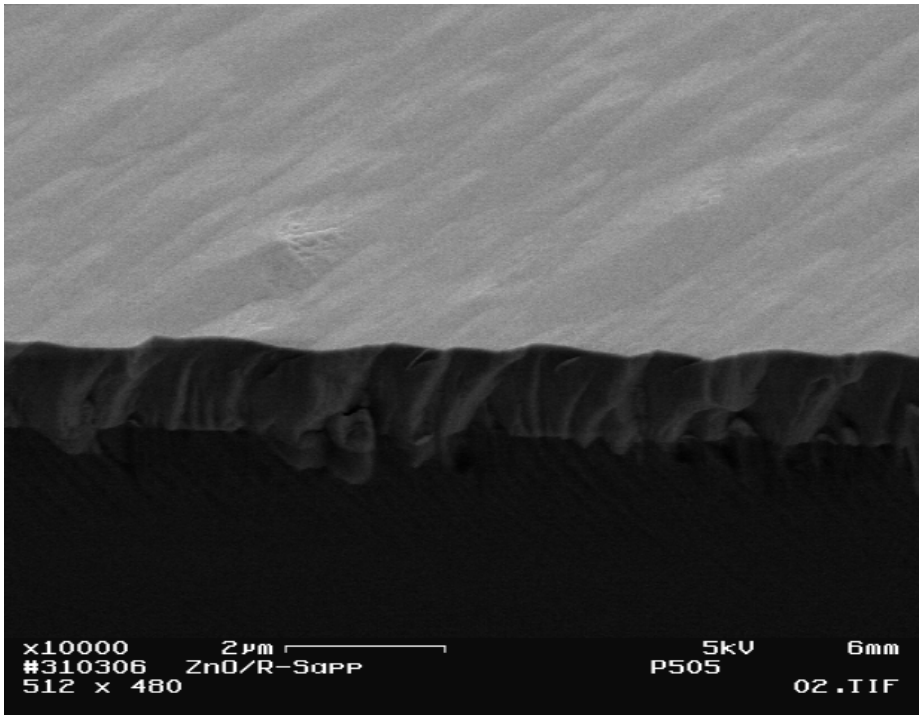

Figure 3.1. FESEM image of ZnO on r-Al_2O_3

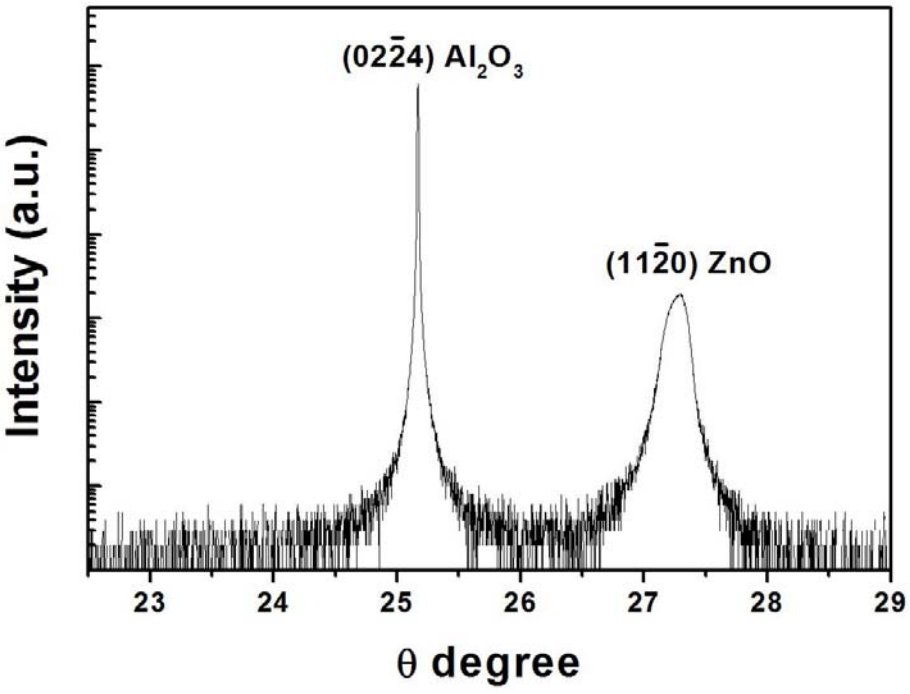

Figure 3.2. θ-2θ scan x-ray diffraction of ZnO film on r-Al_2O_3

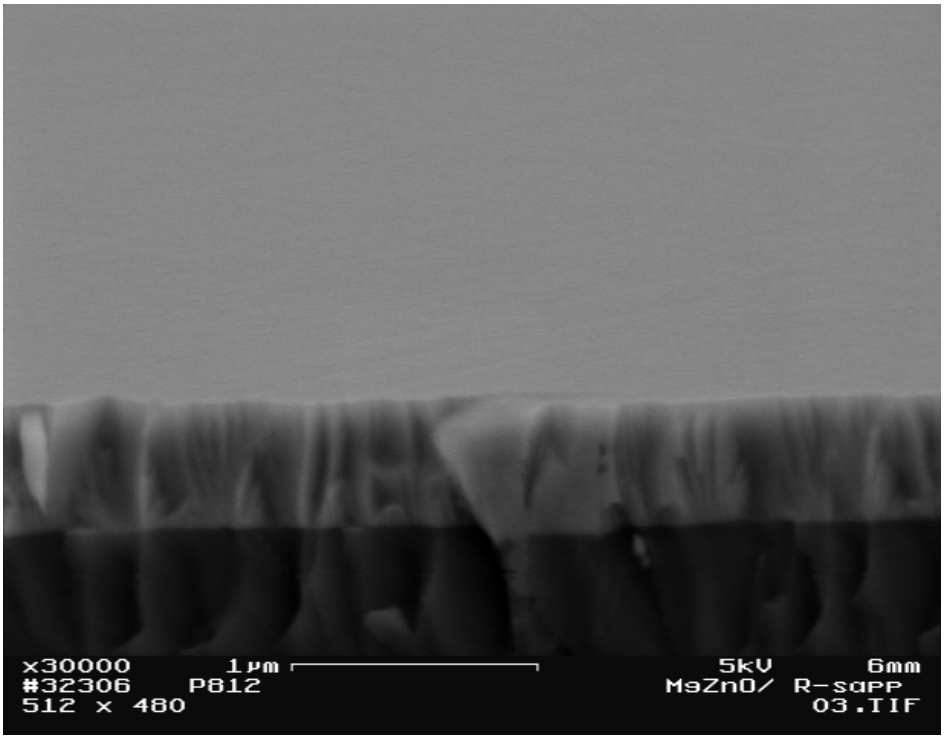

Figure 3.3. FESEM image of $Mg_xZn_{1-x}O$ (x=0.2) on r-Al_2O_3

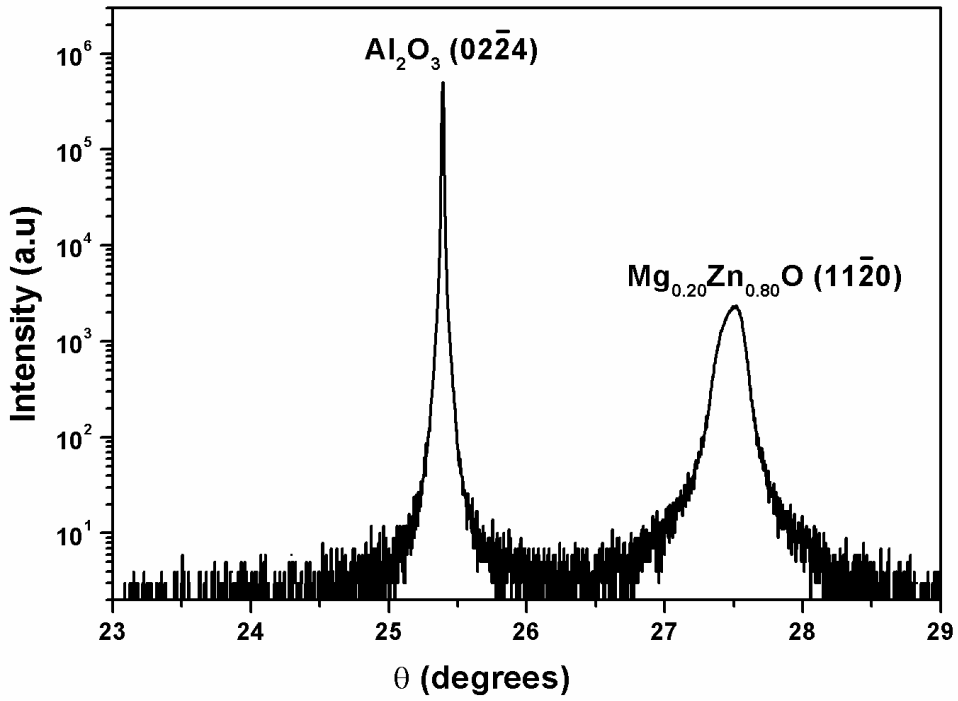

Figure 3.4. θ-2θ scan X-ray diffraction of $Mg_xZn_{1-x}O$ (x=0.2) on r-Al_2O_3

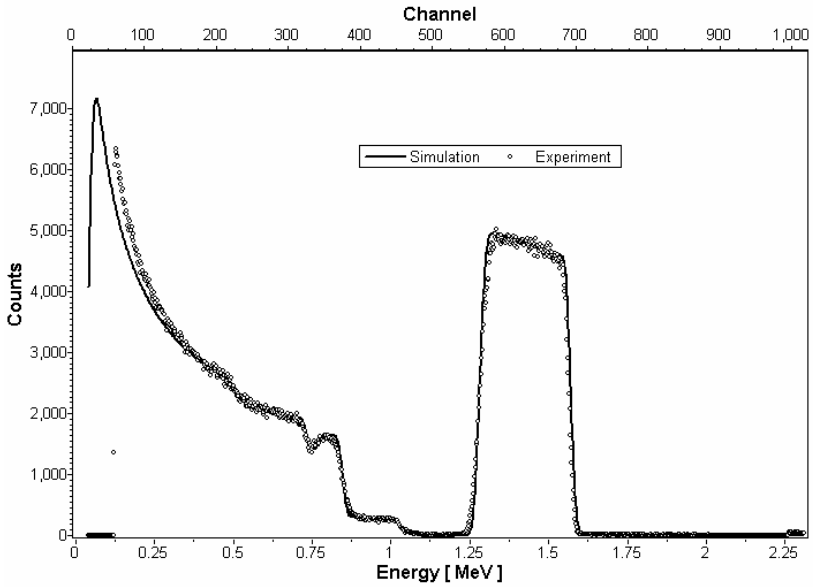

Figure 3.5. RBS spectrum of $Mg_{0.26}Zn_{0.74}O$ film. The value of x was determined by fitting the simulated profile with the experimental data.

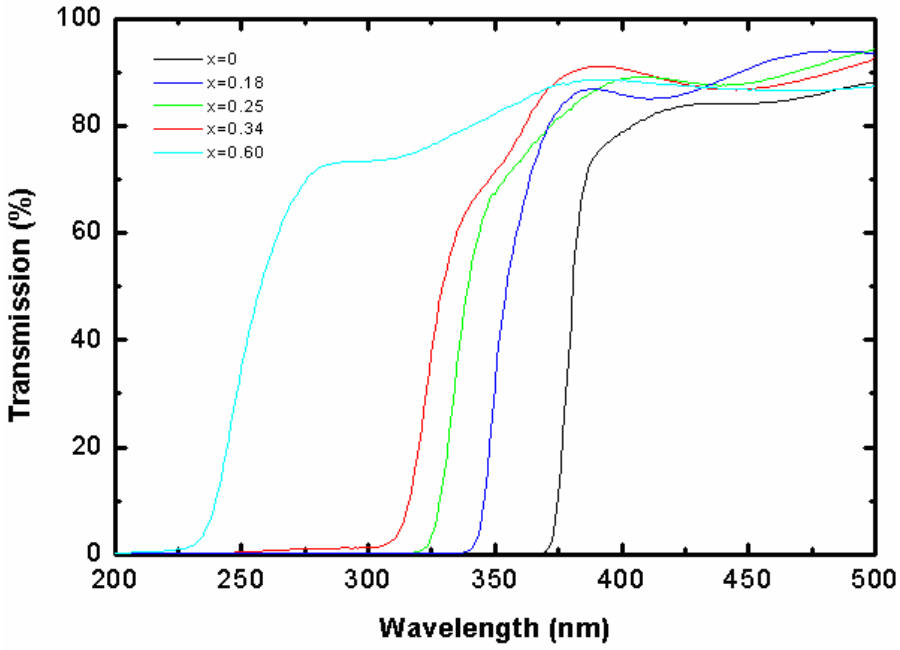

Figure 3.6. Optical transmissions of ZnO and $Mg_xZn_{1-x}O$ films with various Mg compositions.

3.2 Wet Chemical Etching of MOCVD Grown ZnO films on r-Al_2O_3 Substrates

Wet chemical etching process has been widely used in the ZnO-based device fabrication with the major advantages as simple processing, low cost and less surface damage. ZnO films can be etched with both acidic and alkaline solutions, including mixtures such as, HNO_3, HCl, HBr, BOE, BHF, NH_4Cl and Ammonia [75-85]. The etching products of ZnO in aqueous alkali or ammonia are mainly zinc hygroxide ($Zn(OH)_2$), or tetramminezinc (II) complex and soluble zincates by excess alkali. Reacting with acidic solutions, numerous salts are the products. Many of these salts, including chlorides, bromides, iodides, nitrates, sulfates, acetates, chlorates, and perchlorates, are soluble in water. For example, the basic etching process of ZnO in aqueous HCl is:

$$H_2O + HCl_{(aq)} \rightarrow H_3O^+{}_{(aq)} + Cl^-{}_{(aq)}$$

$$ZnO_{(s)} + 2H_3O^+{}_{(aq)} + 2Cl^-{}_{(aq)} = Zn^{2+}{}_{(aq)} + 2Cl^-{}_{(aq)} + 3H_2O$$

Because of the crystalline structure of ZnO, the etch rates of many etchants are direction dependent. In the wurtzite type structure of ZnO, Zn layers and O layers are alternately stacked along the c axial direction. In the single crystal ZnO, there are two polar surfaces: the Zn-terminated (0001) surface and the O-terminated $(000\bar{1})$ surface. These two surfaces were terminated by the same ion, i.e. Zn or O, respectively; therefore, these surfaces have great potential for appearance of distinctive chemical properties [75]. It has been reported that the etch rate of the oxygen face is one order of magnitude faster than the zinc face. Normal to the c-axis, the etch rate is between 40 and 50 times higher than the zinc face [76]. The etching of ZnO is mostly reaction-rate limited with the usual

characteristics, i.e., no dependence of the etch rate on the agitation of the acid mixtures and high activation energy (>6 kcal mol $^{-1}$) with a linear dependence of etch depth on time. In the case of viscous acids such as H_2SO_4 or H_3PO_4, the etching may be diffusion-limited with a low activation energy (<6 kcal mol^{-1}), strong dependence on agitation of the mixture, and a square root dependence of etch depth on time [77].

In the ZnO based thin film device fabrication, several parameters are used to evaluate the etching process, including the etch rate, sidewall slope, etched surface roughness and damage. Currently, various technologies are used to grow ZnO films, including molecular beam epitaxy (MBE), pulsed laser deposition (PLD), RF Sputtering and chemical-vapor deposition (CVD), etc. The etching phenomena show differences in ZnO films grown by different methods.

The etching sidewall slope is mainly determined by the vertical and lateral etch rate of the ZnO film with different etchants. For strong acid as HCl and HNO_3, the etching process is less controllable, even if the acid concentration is drastically reduced, because of the relatively large H_3O^+ concentration. Etching solutions with suitable H_3O^+ concentration is desired for a controllable etch rate [78]. During the ZnO film etching, the adhesion between the mask layer and the ZnO film is another factor influencing the etching profile. Traditional photoresist (PR) mask can be used for large pattern etching. However, due to the poor adhesion to ZnO films, the lateral etch rate is high and the etch profile shows a shallow etch slope. Metal masks, such as Cr and Ni, show good adhesion to the etched film and may generate the steep sidewall. However, the strong acid based metal mask etchants will attack ZnO and finally destroy the pattern.

Up to now, most of the previous studies of ZnO etching were carried out based on

polycrystalline or epitaxial (0001) ZnO films. For the ZnO/r-Al_2O_3 material system used in the tunable SAW device fabrication, since the c-axis of ZnO film is located in the surface, there exists unique in-plane anisotropy in electrical and optical properties. On the other hand, the anisotropic etching behaviors are also expected. In the ZnO wet chemical etch rate investigation, different etching solutions and composition ratios have been used, including HCl: H_2O, HNO_3: H_2O, BOE and H_3PO_4: H_2O. The used MOCVD grown ZnO films had thickness ranging from 0.5 to 2.5 μm. The etched surface was inspected by using SEM and optical microscope. In order to investigate the influence of this etching process on the material properties, such as surface binding and electrical resistivity, X-ray photoelectron spectroscopy (XPS) and four-point probe measurements were carried out.

3.2.1 Investigation of ZnO Etch Rates

The etching rates of different etching solutions and composition ratios are shown in table 3.1. From table 3.1, it can be seen that the etching rate has close relation with the concentration of acid solution. Strong acids with high concentration usually yield higher etching rate. Based on the requirement of device fabrication, controllable etching rate can be achieved by adjusting the solution concentration.

Etching solution	Solution Concentration	Etching rate (μm/min)
HCl: H_2O	1:60	1.9
HCl: H_2O	1:200	0.9
HCl: H_2O	1:500	0.4
HCl: H_2O	1:900	0.2
HNO_3: H_2O	1:100	0.9
BOE	1:7	0.06
H_3PO_4: $C_6H_8O_7$:H_2O	1:1:30	2.2
	1:5:60	1.8
	1:1:80	1.4
	1:1:150	1.0
	1:1:200	0.8
	1:2:300	0.65

Table 3.1. The etching rates of different etchants and concentrations

3.2.2 Investigation and Optimization of the ZnO Etching Slope

For ZnO film epitaxially grown on r-Al_2O_3, different etching solutions generate different etching slopes of the pattern edges, resulted from the difference of vertical and lateral etching rates. This is due to the in-plane anisotropy of the $(11\bar{2}0)$ ZnO films. Most of the etching solutions used in our experiments have a higher lateral etching rate than the vertical one, and generate a small etching slope. For 2.0 μm $(11\bar{2}0)$ ZnO film with photoresist as an etching mask, HCl: H_2O (1:100) and H_3PO_4: H_2O (1:200) generate etching slopes as 1:12~13 (4.6±0.2°) and 1:9~10 (6.0±0.3°), respectively. Higher concentration of strong acid solutions, such as HCl: H_2O (1:60) and HNO_3: H_2O (1:100) do not improve the slope. In contrast, it has been found that by using H_3PO_4 etching solution, a relatively steeper edge slope is generated. For example, a H_3PO_4 : $C_6H_8O_7$: H_2O (1:1:60) solution resulted in an etching slope 1:5~6 (10.3±0.8°). The introduction of citric acid is to reduce the concentration of H_3O^+ in the etching solution. H_3PO_4 is not as strong as HCl and HNO_3, indicated by its first dissociation constant $K_{a1}=7.5\times10^{-3}$. Although in the solution, phosphoric acid behaves as a triprotic acid, having three ionizable hydrogen atoms, its K_{a2} and K_{a3} are much smaller than K_{a1} as shown in Table 3.2 [86].

$H_3PO_4(aq)$	⇔	$H^+(aq) + H_2PO_4^-(aq)$	$K_{a1} = 7.5 \times 10^{-3}$
$H_2PO_4^-(aq)$	⇔	$H^+(aq) + HPO_4^{2-}(aq)$	$K_{a2} = 6.2 \times 10^{-8}$
$HPO_4^{2-}(aq)$	⇔	$H^+(aq) + PO_4^{3-}(aq)$	$K_{a3} = 1.7 \times 10^{-12}$

Table 3.2. Dissociation constants of H_3PO_4

In wet chemical etching, ZnO dissolves in the aqueous H_3PO_4 acid by the hydronium ions (H_3O^+) attacking the oxygen, forming water, then producing soluble salt

[78]:

$$ZnO(s) + 2H_3O^+(aq) \rightarrow Zn^{2+}(aq) + 3H_2O(l) \quad (3.1)$$

The enhanced edge etching, or corner effect, has been observed on all samples as shown in Figure 3.7. Generally, the enhanced edge etching indicates a diffusion limited etching reaction [87]. For strong acids in a diffusion limited etching process, the consumed etchant can be resupplied fast due to the high dissociation constant and H_3O^+ concentration. This results in a less controllable etching process. In contrast, for the relatively weaker acids such as H_3PO_4, the supplement of consumed etchant penetrating below the mask is relatively slower because of its smaller dissociation constant and H_3O^+ concentration. Thus, the in-plane lateral etching rate is limited in comparison with the case of the strong acids. By maintaining, or increasing, the vertical etching rate, the edge slope becomes steeper. In our experiments, instead of the stationary etching process, a series of discrete short time etching cycles were applied. Each cycle includes a 10 second stationary etching followed by water cleaning and N_2 drying. By using this technique with a H_3PO_4: $C_6H_8O_7$ (citric acid): H_2O (1:1:60) solution, a 1:3.4~4 (15.1±1.0°) etching slope is obtained.

The mask/film adhesion condition influences the lateral etching rate. Good adhesion will limit the penetration of the etchant below the mask; therefore, reduce the lateral etching rate. To improve the adhesion, a 150 nm Al layer was deposited on the ZnO films to serve as the etching mask. The SEM photography of the etched sample with an Al mask is shown in Figure 3.8. The film thickness is ~1.4 μm and the Al mask has been removed. In comparison to thin ZnO films (≤ ~500nm), the thick ZnO film on r-Al_2O_3 substrate shows larger surface roughness. The root mean square (rms) roughness of a

~2.0 μm ZnO film on r-Al_2O_3 substrate is ~9nm. The c-axis of the a-plane ZnO film lies in the growth plane, which results in the in-plane anisotropy of the physical properties between the directions perpendicular to the c-axis versus parallel to the c-axis. The surface roughness is caused by anisotropic growth kinetics and in-plane strain relaxation in the films. From Figure 3.8, it can be seen that this etching process results in a steep sidewall in the direction along to c-axis of ZnO film, and the profile slope is close to 1:1(45°). For the edge in the direction perpendicular to the c-axis, the profile slope reaches 1:2 (26.6°). This etching slope difference indicates that because the film's primary symmetric axis is located in the plane, the wet chemical etching of $(11\bar{2}0)$ ZnO film is anisotropic.

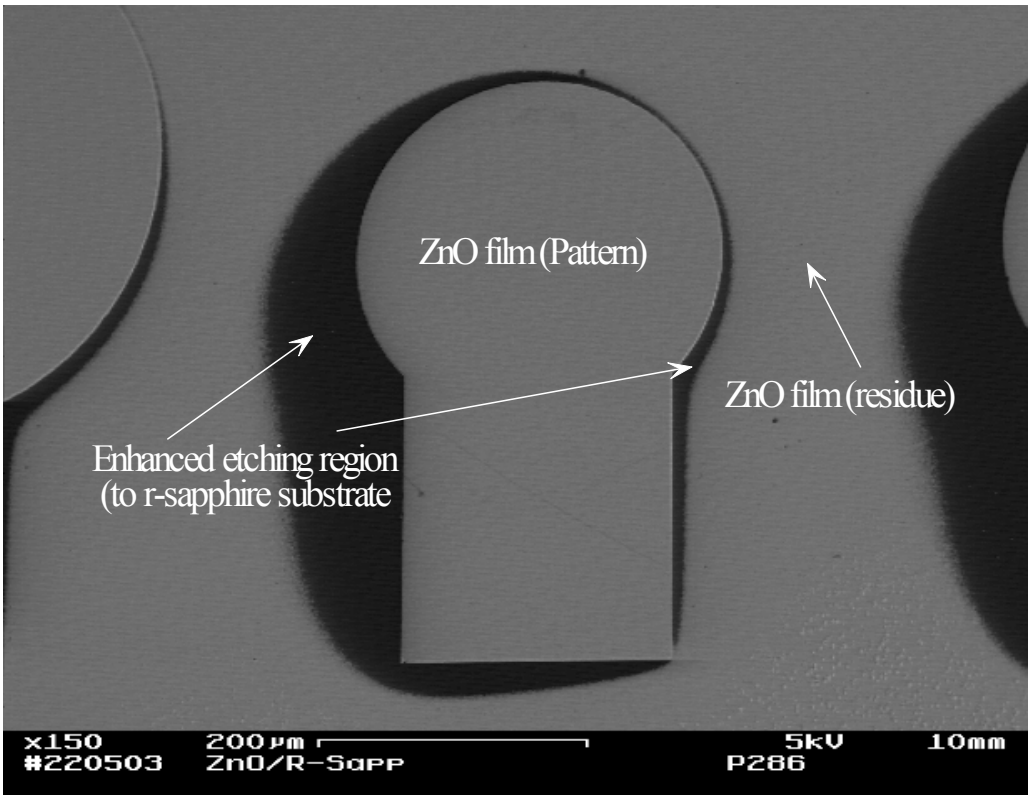

Figure 3.7. SEM of a ZnO sample with enhanced edge etching (Corner effect)

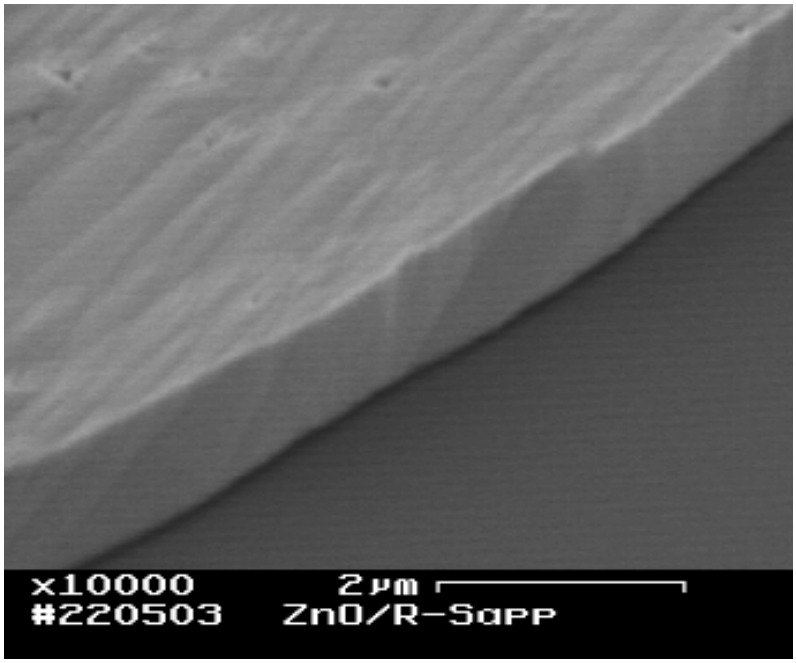

(a)

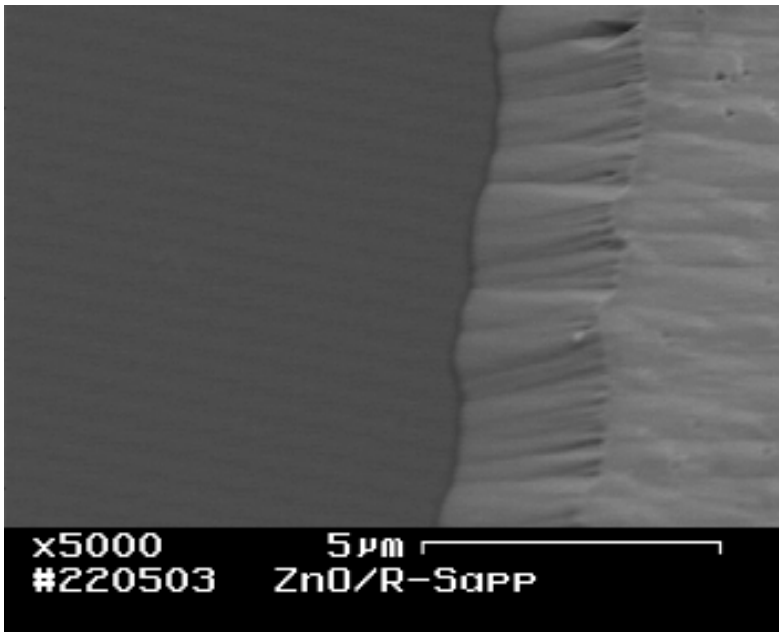

(b)

Figure 3.8. SEM photography of a ZnO sample etched with Al mask+Phosphoric etching mixture. Pattern edge (a) parallel to c-axis (b) vertical to c-axis. (Film thickness 1.4 μm after Al removal)

3.2.3 Analysis of the Etched ZnO Surface

In order to investigate the influence of the wet chemical etching on the surface properties, XPS measurements with Al K_α radiation are taken. The test samples are etched 0.6 μm with selected phosphoric acid solution. The survey and detailed spectra Zn 2p and O1s are monitored. No change in Zn 2p spectra is found and no Phosphoric related fragments are shown on the samples. The band broading 5% is found in the O1s spectrum. Gaussian deconvolution of O1s peak shows the increasing of high binding energy fragment, probably related with OH and CO contaminations during water cleaning and etching. The survey and detailed Zn 2p and O1s spectra of the etched and un-etched samples are shown in Figure 3.9, respectively. For the etched sample (0.6 μm etching depth), four-point probe measurements (MAGNE-TRON Mod M-700) shows no change in the sheet resistivity (10.0-40.0 Ω-cm) compared with the un-etched one.

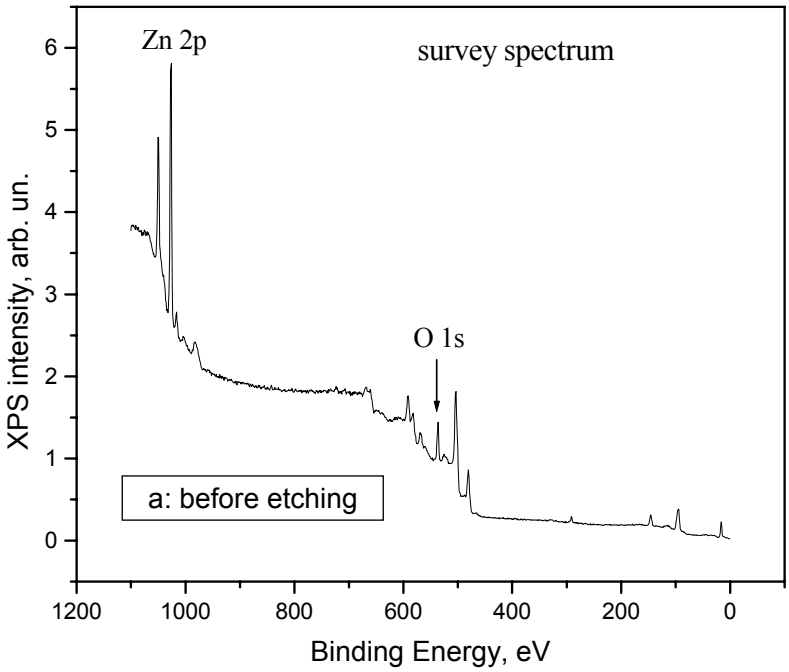
Zn 2p
survey spectrum
O 1s
a: before etching
XPS intensity, arb. un.
Binding Energy, eV
0
1
2
3
4
5
6
1200
1000
800
600
400
200
0

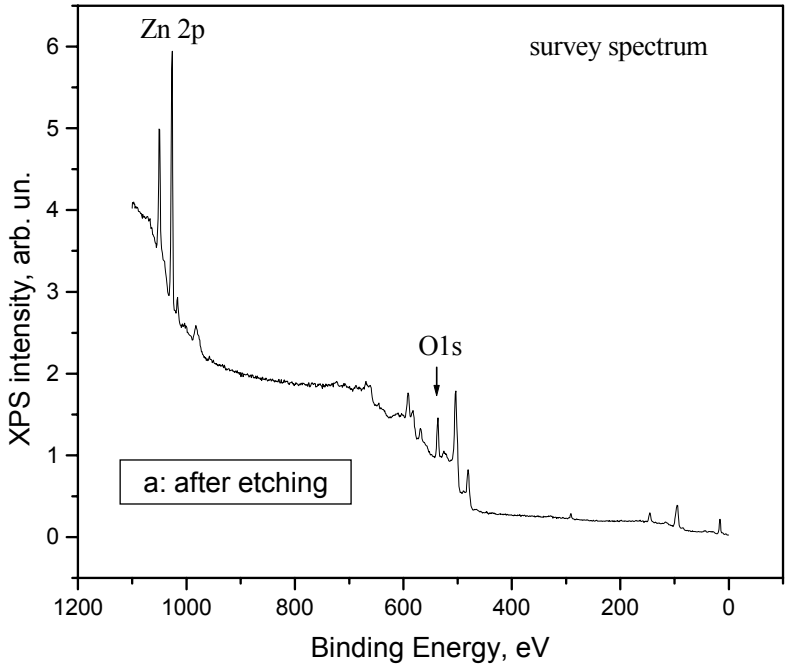
Zn 2p
survey spectrum
O1s
a: after etching
XPS intensity, arb. un.
Binding Energy, eV
0
1
2
3
4
5
6
1200
1000
800
600
400
200
0

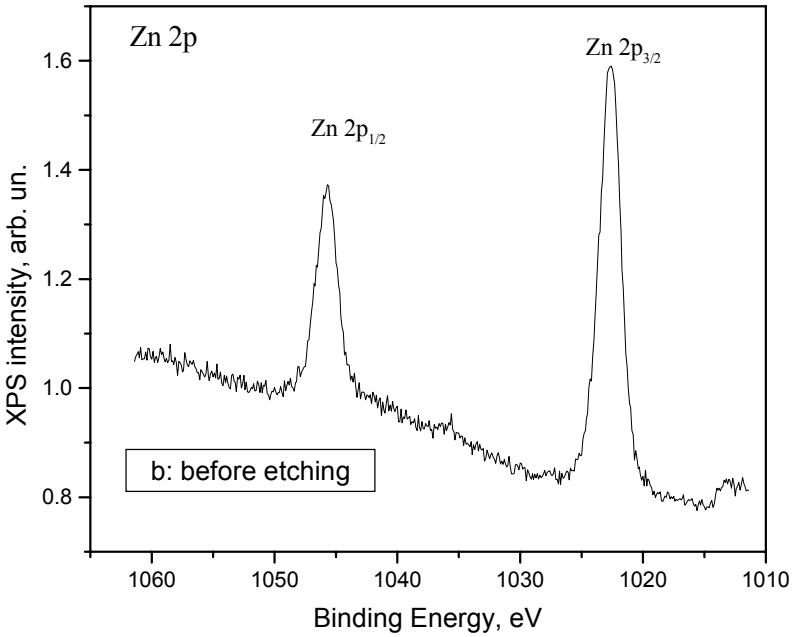
Zn 2p
Zn 2p3/2
Zn 2p1/2
b: before etching
XPS intensity, arb. un.
Binding Energy, eV
1.6
1.4
1.2
1.0
0.8
1060
1050
1040
1030
1020
1010

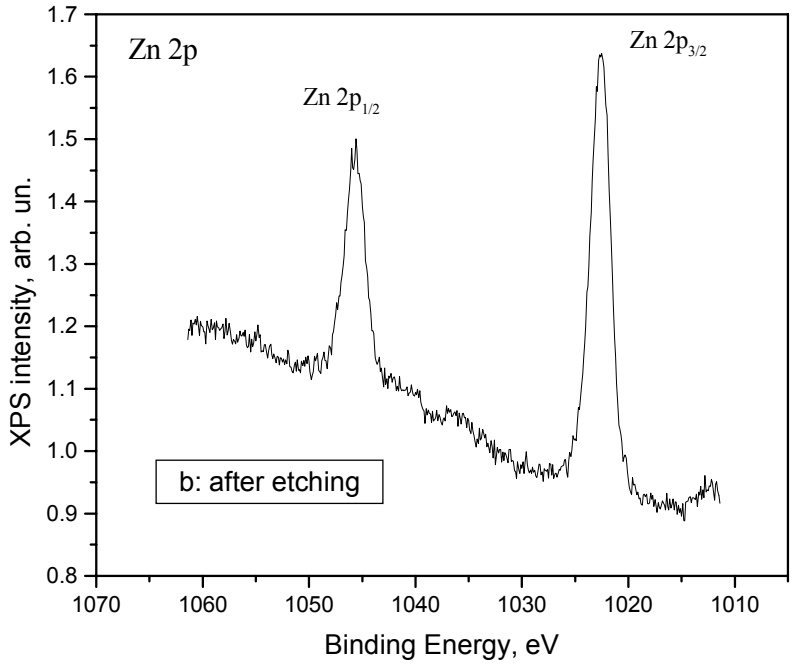
Zn 2p
Zn 2p3/2
Zn 2p1/2
b: after etching
XPS intensity, arb. un.
Binding Energy, eV
1.7
1.6
1.5
1.4
1.3
1.2
1.1
1.0
0.9
0.8
1070
1060
1050
1040
1030
1020
1010

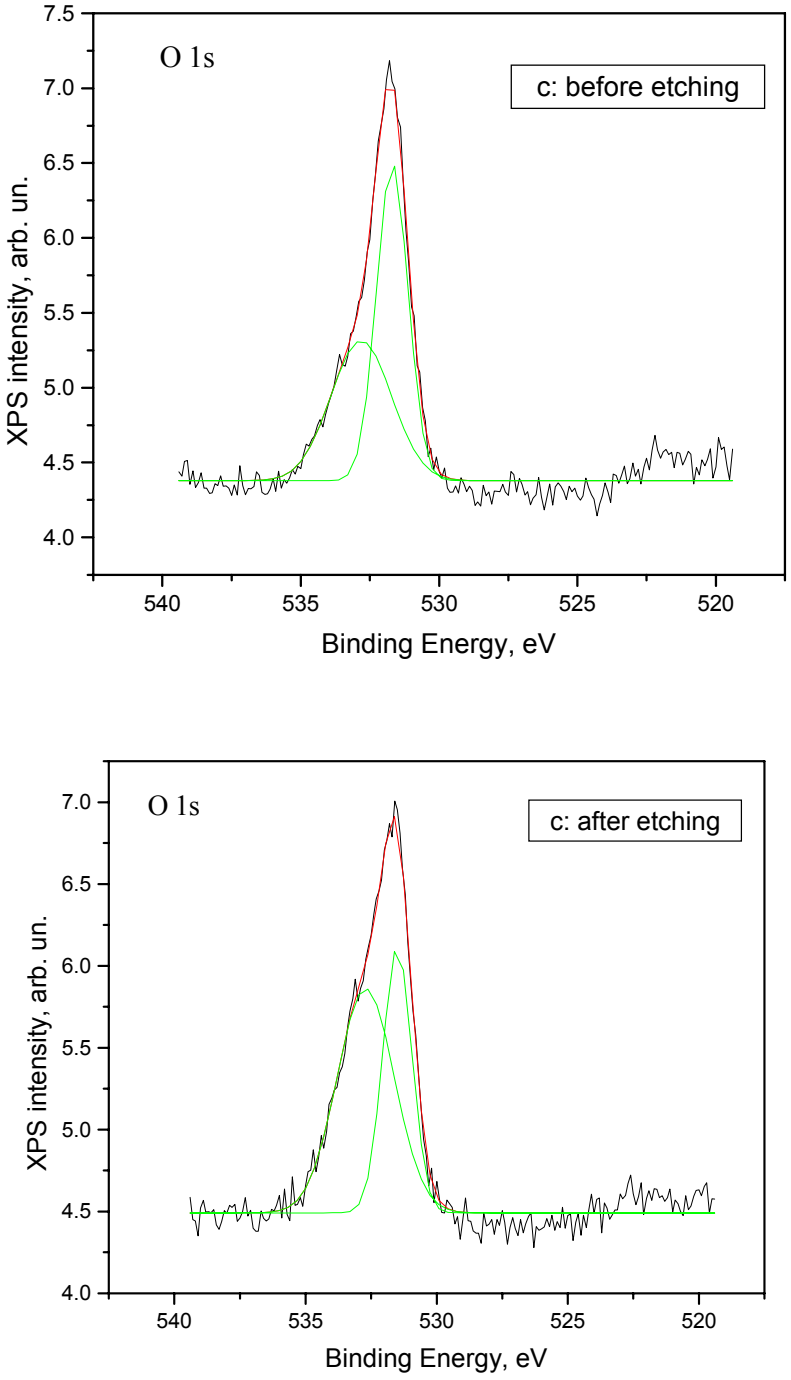

Figure 3. 9. XPS of $(11\bar{2}0)$ ZnO: (a) The survey spectra (b) Zn 2p spectra (c) O1s spectra before etching and after 0.6 μm etching

3.3 Reactive Ion Etching (RIE) of ZnO and $Mg_xZn_{1-x}O$ Films Grown on r-Al_2O_3 by MOCVD

Although wet chemical etching of ZnO films has advantages such as simple process and less surface damage, the major disadvantages are the serious under cut, small sidewall slope and direction dependence. Meanwhile, dry etching technology has been widely used in semiconductor device fabrications, which supplies highly anisotropic etch profile and fine pattern control.

3.3.1 Dry Etching Technology

Dry etching technology is an etching process without using liquid chemicals or etchants to remove materials and form the pattern. In the dry etching process, a solid state surface is etched in the gas phase based on three basic etching mechanisms, (1) physically by ion bombardment, (2) chemically by a chemical reaction with a reactive species at the surface, or (3) combined physical and chemical mechanisms. In various dry etching techniques, physical sputtering and ion beam milling are examples of purely physical dry etching techniques. The reactive plasma etching is an example of a purely chemical dry etching technique. The reactive ion etching employs both physical and chemical processes [88, 89].

In the pure physical plasma etching, the etching is realized mainly by momentum transfer between energetic ions and the substrate surface. The etching process is inherently nonselective, due to the large ion energies. The etch rate of the pure physical plasma etching is lower than other dry etching means and the electrical damage from ion bombardment can be problematic. In the reactive plasma etching, there are six basic steps

involved: 1st the production of the reactive species in the gas-phase; 2nd the reactive species diffuse to the solid; 3rd the reactive species are absorbed; 4th reaction with the solid surface; 5th desorption of the byproducts from the surface; 6th diffusion of the desorbed byproducts into the bulk of the gas. However, the pure chemical dry etching does not exhibit high anisotropy, because chemical reactions can and do occur in all directions. By considering the advantages and disadvantages of pure physical and pure chemical dry etching respectively, the more useful plasma etching is to add a physical component to a purely chemical etching mechanism. As a result, the reactive ion etching (RIE) has been widely used semiconductor industry. In the RIE, a reactive sputter etching (RSE) consists of bombarding the material with highly energetic chemically reactive ions. In addition to sputter-removal, the bombarding ions are chosen so that they will chemically react with the material being bombarded to produce highly volatile reaction byproducts that can simply be pumped out of the system. To generate plasma operating at low pressure with very high ion density, which supplies high etch rate and good anisotropic etch profile, new plasma sources, such as electron cyclotron resonance (ECR) and inductively coupled plasma (ICP), have been developed [89, 90].

3.3.2 Current Status of ZnO Dry Etching

For ZnO dry etching, some initial investigations have been reported for the sputter-deposited ZnO thin films and bulk substrates with respect to the etching conditions, etch rates, etching profiles, surface damage, influence to the optical and electrical properties [91-98]. Although various gas combinations have been used, there are three basic gas chemistries 1) Cl_2 based; 2) CH_4 based and 3) BCl_3 based.

(a) Cl_2 based ZnO Dry Etching

Chlorine based ZnO dry etching is favorable than fluorine based chemistries due to the volatility of the $ZnCl_2$ etch product versus the ZnF_2 product. The etch rates range from 20 to 300 nm/min, depending on the etching mixture, RF power, chamber pressure and substrate temperature [91-94]. The general gas mixtures used in the Cl_2 based ZnO dry etching includes Cl_2/Ar, Cl_2/H_2, and Cl_2/H_2/Ar.

Band-edge photoluminescence (PL) study indicates that a substantial decrease in the PL intensity is observed in Cl_2 and Cl_2/H_2/Ar plasmas etched ZnO samples [93]. In comparison to Cl_2/H_2/Ar plasmas, a more severe degradation was observed in Cl_2-based chemistries and probably due to plasma induced surface damage.

(b) CH_4 based ZnO Dry Etching

To achieve high etch rate of ZnO, it prefers the etch products have high vapor pressure and low boiling temperature to make the removal easier. In the CH_4-based ZnO dry etching, CH_x fragments can react with ZnO to form volatile metallorganic zinc compounds, such as $(CH_3)_yZn$. For example, one possible product $(CH_3)_2Zn$ has a very high vapor pressure of 301 Torr at 20^{o}C which is significantly higher than that of $ZnCl_2$ (only 1 Torr at 428°C). The general gas mixtures used in the CH_4 based ZnO dry etching includes CHF_3/H_2, CH_4/CF_4, CH_4/H_2, and CH_4/H_2/Ar. The CH_4 based ZnO dry etching rates range from 19 to 300 nm/min, depending on the etching mixture, RF power, chamber pressure and substrate temperature [91-93, 95]. It has been reported the decrease in PL intensity observed with CH_4/H_2/Ar mixtures is not as severe as that observed for Cl_2/Ar gas mixtures [93]. Figure 3.10 give the SEM of a ZnO sample etched with ECR plasma at condition of CH_4:CF_4=1:1 with 80W RF power and 1kV DC bias [95]. The etched ZnO sample was grown by MBE with a metal zinc source (7*N*) and oxygen (6*N*).

(c) BCl_3 based ZnO Dry Etching

As the third basic ZnO etching chemistry, BCl_3 avoids the formation of polymeric compounds during the CH_4-based plasma etching. BCl_3 is a more effective etch chemistry than Cl_2 because B and BCl radicals help to remove surface oxides by forming volatile oxygen compounds such as $(BOCl)_3$, BOCl, and B_xO_y. The general gas mixtures used in the BCl_3 based ZnO dry etching includes BCl_3, BCl_3 /Ar, BCl_3/Cl_2/Ar, and $BCl_3/CH_4/H_2$. The BCl_3 based ZnO dry etching rates ranges from 10 to 300 nm/min, depending on the etching mixture, RF power, chamber pressure and substrate temperature [96-98]. Figure 3.11 gives the SEM of a BCl_3 etched ZnO sample. The etching condition is 20 sccm BCl_3 flow rate with 900 W ICP power and 100 W RF power [96]. The etched ZnO sample was grown by RF-sputtering at 800 °C on c-sapphire substrate.

Besides these three basic ZnO dry etching chemistries, other reaction gases are also used, such as $SiCl_4$ and HI. In the ZnO dry etching study, in addition to the etch rate, the etching profile, etched surface morphology, surface contamination and damage are also of critical importance to the ZnO based thin film device fabrication.

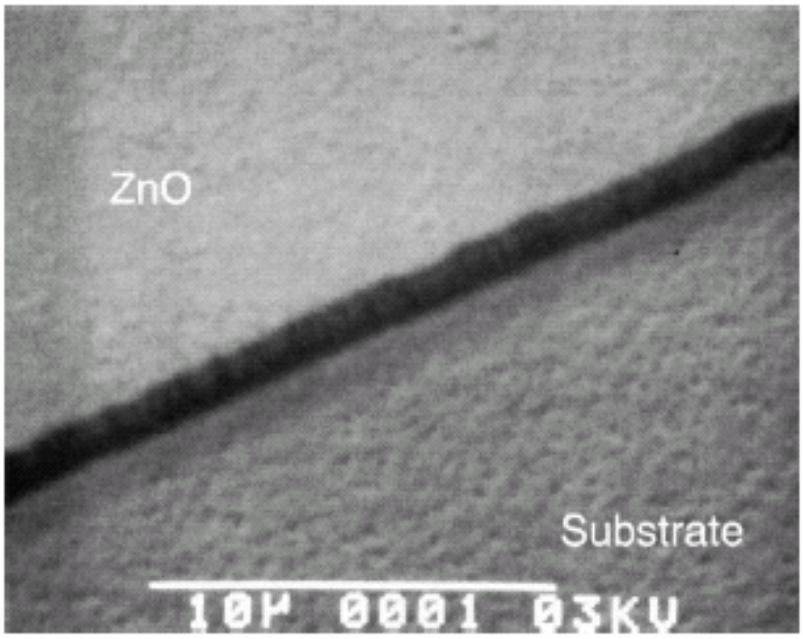

Figure 3.10. SEM image of a ZnO film etched in a ECR plasma of the gas mixture with CH_4 :CF_4=1:1 with 80W RF power and 1kV DC bias [95]

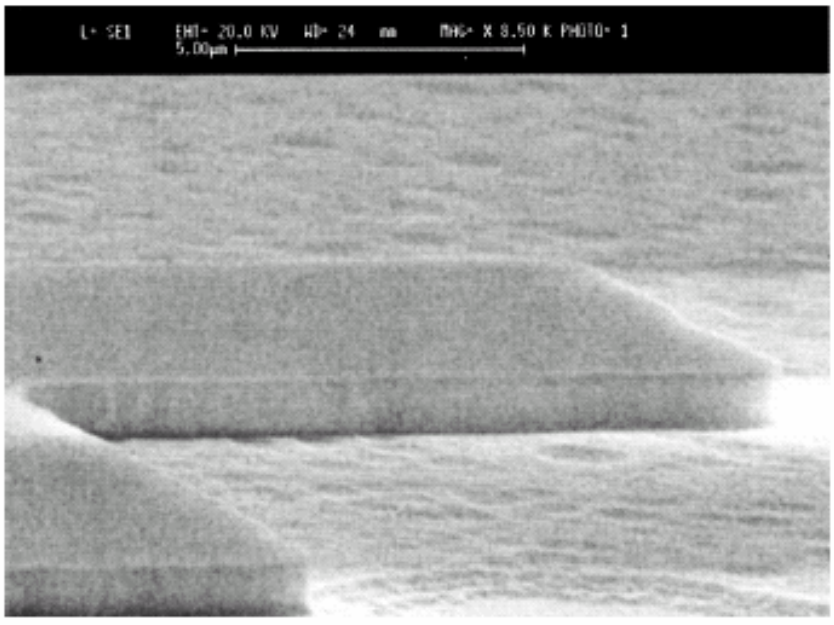

Figure 3.11. SEM of ZnO sample patterned with NiCr mask and etched in 20 sccm BCl_3 flow rate with 900 W ICP power and 100 W RF power [96]

3.3.3 Experimental investigation of $SiCl_4$ based RIE of MOCVD grown ZnO and $Mg_xZn_{1-x}O$ films on r-Al_2O_3

Although some initial dry etching results have been reported for both sputter-deposited ZnO films and bulk ZnO substrates, there is little information available in literatures on the dry etching of $Mg_xZn_{1-x}O$ films. As described in chapter 2, $Mg_xZn_{1-x}O$ and $Mg_xZn_{1-x}O$/ZnO heterostructure have wide potential applications, such as solar blind UV photodetectors, UV lasing and HFET. Integrating the $Mg_xZn_{1-x}O$/ZnO heterostructure with SAW technology may realize high efficiency tunable SAW device based on the acoustoelectric interaction, which offers low bias and large tuning range.

Targeting for fine pattern device fabrication and accurate etch rate control, we also conducted the dry etching investigation of the MOCVD grown ZnO and $Mg_xZn_{1-x}O$ films on r-Al_2O_3 substrates. In this work, $SiCl_4$ was used as the reaction gas for the ZnO and $Mg_xZn_{1-x}O$ films. The Reactive Ion Etching was conducted in a Trion MINILOCK II ICP-RIE system. The plasma density and ion energy are controlled by the ICP coil power supply and RIE power supply, respectively. Instead of using photoresist or metal as etching masks, SiO_2 layer deposited by plasma enhanced chemical vapor deposition (PECVD) was used as the etching mask. The SiO_2 mask layer was deposited in a Plasma-Thermal 790 PECVD system with deposition condition as: substrate temperature: 250^oC; Wall temperature: 60 ^oC; SiH_4 flow rate: 200 sccm; N_2O flow rate: 1100 sccm; and RF power: 25 W. To form the SiO_2 etching mask pattern, a CF_4 based RIE process was used with the photoresist mask. After the ZnO dry etching, the SiO_2 mask was removed by the same CF_4 based RIE process. Up on the finish of the ZnO RIE, the etched samples were

immediately rinsed in DI water then dried by N_2 gas to avoid corrosion by hydrochloric acid, formed by residual chlorine and water vapor. The $Mg_xZn_{1-x}O$ RIE etch rates were investigated as a function of the Mg composition (x=0 for ZnO, 0.17, 0.22, 0.28), with RIE power ranging from 200 W to 500 W and chamber pressure from 40 mTorr to 100 mTorr. The RIE etch rates of $Mg_xZn_{1-x}O$ with respect to RIE power and chamber pressure are shown in Figure 3.12 (a) and (b), respectively. As observed in Figure 3.12 (a), at a fixed chamber pressure of 60 mTorr, as RIE power changes from 200 W to 500 W, the etch rates of both ZnO and $Mg_xZn_{1-x}O$ samples increase. ZnO etch rate is found to change from 12.8 nm/min to 28.8 nm/min. An increase of the RIE power raises the plasma ion energy, which in turn enhances the reaction product dissociation from the etching surface, thus increasing the etch rate. The relatively low etch rate of the $SiCl_4$ RIE of ZnO is primarily due to the high boiling temperature (737^oC) of the reaction product $ZnCl_2$, which makes the evaporation of the reaction products from the etching surface difficult, thus preventing the sample being etched further. As compared to the pure ZnO samples, the etching of $Mg_xZn_{1-x}O$ includes both $ZnCl_2$ and $MgCl_2$ as reaction products. The boiling temperature of $MgCl_2$ is 1412^oC, which is much higher than that of $ZnCl_2$. With a higher Mg composition in $Mg_xZn_{1-x}O$, the ratio of $MgCl_2$ in the reaction products increases, which increases the difficulty of the reaction product removal, thus reduces the etch rate. In Figure 3.12(b), at a fixed RIE power of 300 W and with a change of the chamber pressure from 40 to 100 mTorr, the etch rates of both ZnO and $Mg_xZn_{1-x}O$ is found to decrease initially, till it becomes relatively saturated. The etch rate of ZnO is found to change from 22.5 nm/min to 10.9 nm/min. The chamber pressure was chosen in the ion-assisted etching range. An increase of the chamber pressure reduces the mean free

path length of the ions, thus reducing the ion energy. Low ion energy in an ion-assisted etching makes the ion-assisted desorption of the etching products less efficient and reduces the etch rate further. The possible reason for observed saturation in the etch rate at high-pressure range (~80 to 100 mTorr) could be due to a shift of etching mechanism from ion-assisted etching to chemical plasma etching.

Figure 3.13 (a) shows the SEM micrograph of a ZnO sample etched with chamber pressure of 60 mTorr, RIE power of 300 W and $SiCl_4$ flow rate of 20 sccm. The SiO_2 etching mask is removed by CF_4 based RIE. From this figure, it can be observed that well-defined ZnO pattern is fabricated on the r-sapphire substrate. The etching sidewall is steep and the sidewall facet is smooth. In comparison to the as-grown films, there is no observable change in the surface morphology after the removal of the SiO_2 mask. Figure 3.13 (b) shows a comparison between the RIE etched and un-etched ZnO surface. The etched surface is found to be smooth, with surface roughness at the similar scale as the un-etched ZnO surface. Due to the in-plane anisotropy in $(11\bar{2}0)$ ZnO and $Mg_xZn_{1-x}O$, the difference in etch rate along c-axis [0001] direction against the etch rate in the perpendicular to c-axis $[1\bar{1}00]$ direction is observed for wet chemical etching. This in-plan etching anisotropy is found to be reduced in the $SiCl_4$-based RIE.

In order to evaluate the surface damage due to the RIE, room temperature photoluminescence (PL) spectra were measured. No changes in PL peak intensity and half-width are observed, suggesting that the good optical quality of the samples is preserved after RIE etching. To investigate the influence of the $SiCl_4$-based RIE to the surface characteristic of ZnO and $Mg_xZn_{1-x}O$, X-ray photoelectron spectroscopy (XPS) was carried out with Al K_α excitation at 1486.6 eV on the etched and un-etched samples.

The survey spectrum was monitored. Figure 3.14 shows the XPS comparison of the etched and un-etched ZnO samples. Figure 3.14 (a) and (c) are the survey spectrum of the un-etched and etched sample. Figure 3.14 (b) and (d) are the zoom-in view of the survey spectrum to investigate possibility of surface contamination induced by RIE. The comparison samples were prepared with RIE conditions of chamber pressure of 60 mTorr, RIE power of 300 W and $SiCl_4$ flow rate of 20 sccm. Short time BOE cleaning was applied to the testing samples after the $SiCl_4$ RIE. Neither Si, nor Cl traces are found, within the sensitivity limit of the XPS equipment.

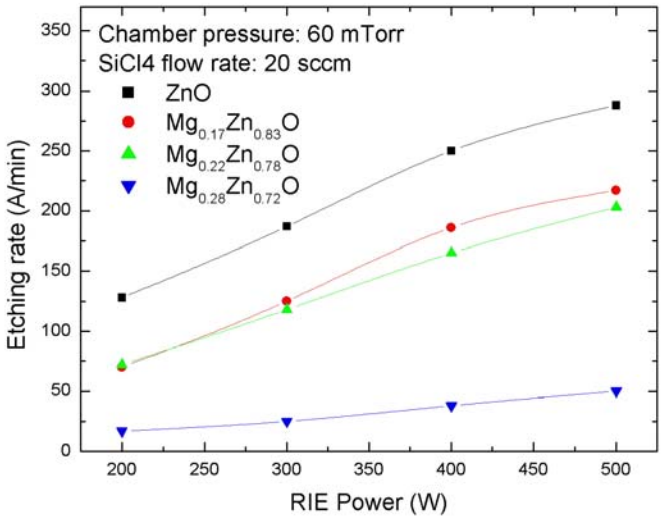

(a)

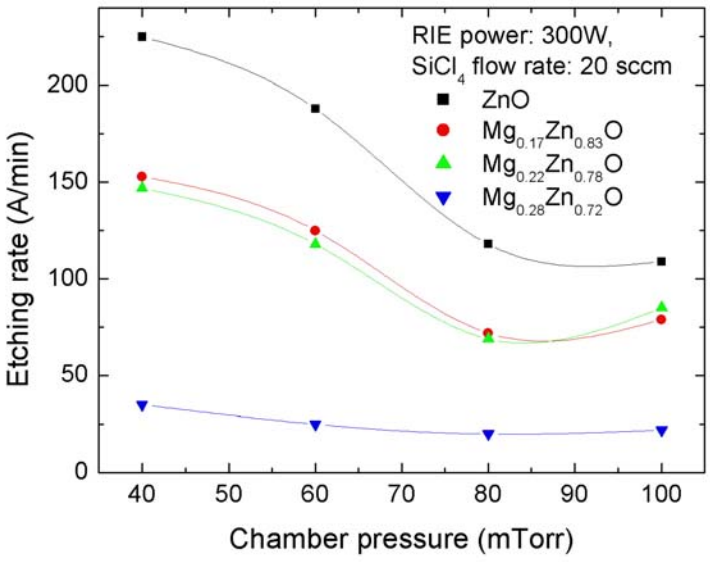

(b)

Figure 3.12. RIE etch rate of $Mg_xZn_{1-x}O$ ($0 \leq x \leq 0.28$) with respect to the Mg composition, chamber pressure and RIE power: (a) etch rate vs. RIE power; (b) etch rate vs. chamber pressure.

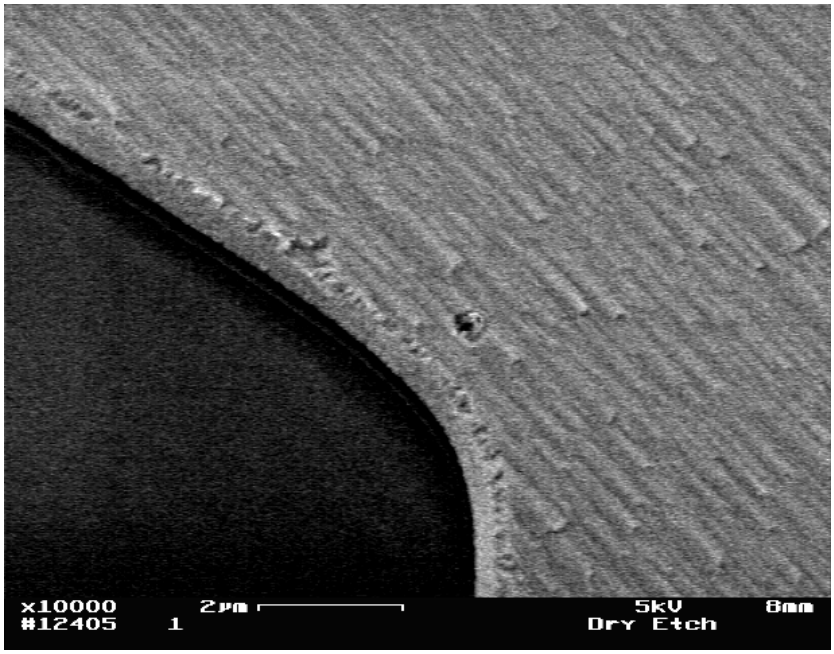

(a)

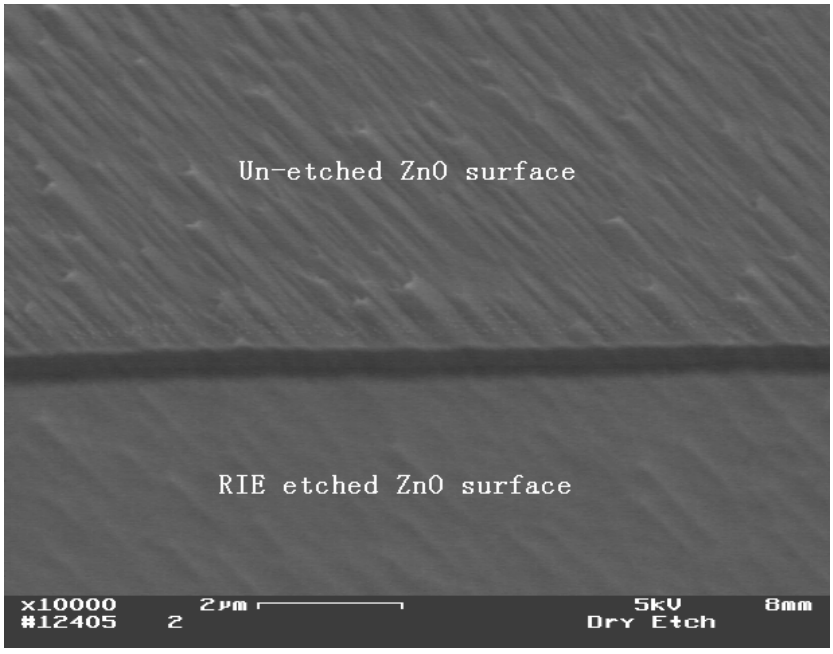

(b)

Figure 3.13. The SEM photographs of the etched ZnO samples. (a) The SEM of a RIE etched ZnO sample; (b) The SEM of the un-etched and etched ZnO surface. The SiO_2 mask is removed.

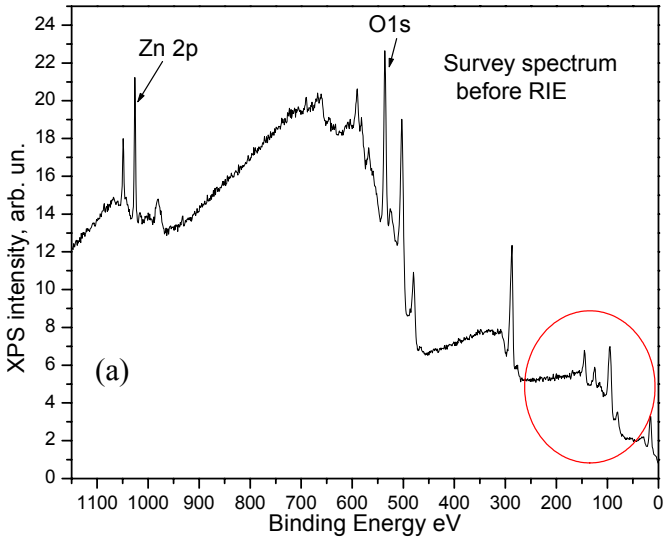
Zn 2p
O1s
Survey spectrum
before RIE
(a)
XPS intensity, arb. un.
Binding Energy eV

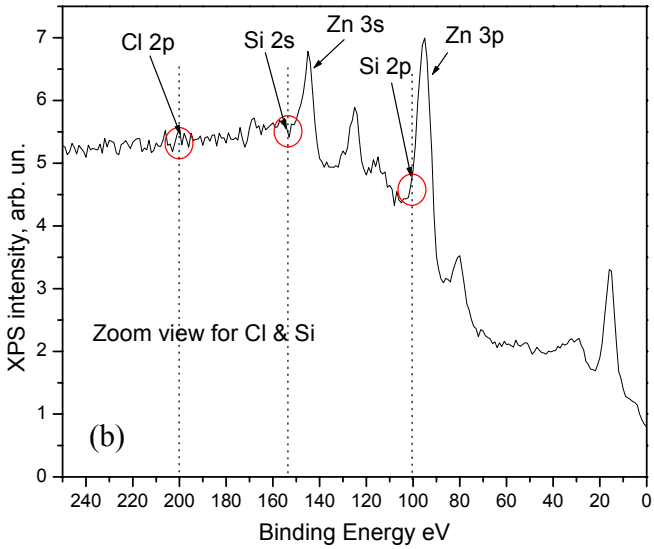
Cl 2p
Si 2s
Zn 3s
Si 2p
Zn 3p
Zoom view for Cl & Si
(b)
XPS intensity, arb. un.
Binding Energy eV

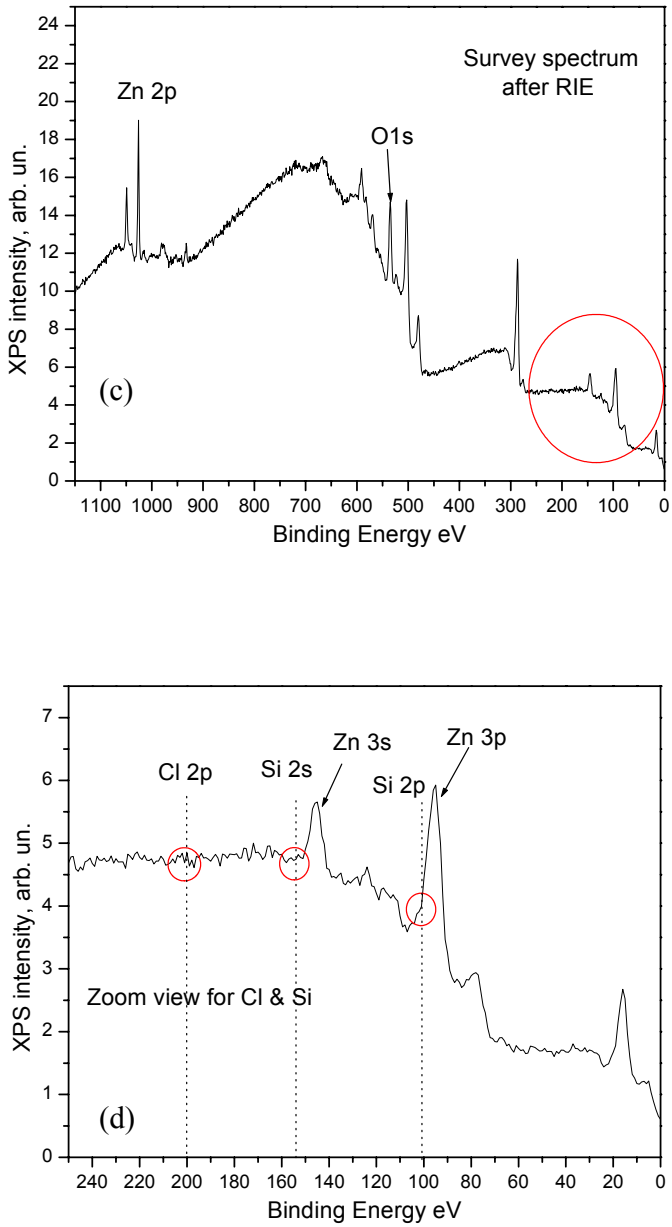

Figure 3.14. XPS survey spectrum of the ZnO sample before and after $SiCl_4$ RIE (after BOE cleaning). (a) and (b): Before RIE and Zoom view for Si and Cl; (c) and (d): After RIE and Zoom view for Si and Cl.

3.4 Summary

In order to fulfill the requirement of the ZnO device fabrication, investigation of the wet chemical etching and dry etching of MOCVD grown ZnO and $Mg_xZn_{1-x}O$ films on r-Al_2O_3 substrates has been carried out. A wet chemical etch process with controllable etching rate is developed to etch $(11\bar{2}0)$ ZnO epitaxial films. H_3PO_4 generates a better etching slope due to a diffusion limited etching mechanism. Compared with the stationary etching, a series of discrete short-time etching-rinsing cycles increase the vertical etching rate, and therefore improve the vertical/lateral slope ratio. The use of an Al metal as the etching mask to replace the photoresist mask improves the mask/film adhesion and limits the lateral etching rate. A vertical/horizontal-etching slope of 1:1 was obtained in the directions perpendicular to c-axis of $(11\bar{2}0)$ ZnO films. The wet chemical etching of $(11\bar{2}0)$ ZnO film is anisotropic. The XPS and electrical tests indicate that the etching process preserves the surface properties of the original films. For the $SiCl_4$ based reactive ion etching of ZnO and $Mg_xZn_{1-x}O$ ($x<0.3$) films grown on r-sapphire substrates, it is found that the etch rate of $Mg_xZn_{1-x}O$ increases with an increase of RIE power and with a decrease of the chamber pressure. It is also observed that an increase of Mg composition in the $Mg_xZn_{1-x}O$ reduces the etch rate. This is attributed to the high boiling temperature of the etching products. SiO_2 is found to be a suitable mask material for $SiCl_4$-based RIE for ZnO and $Mg_xZn_{1-x}O$. The SEM, XPS and PL measurements show that under the current RIE conditions, there is no observable surface damage or optical deterioration of the etched ZnO and $Mg_xZn_{1-x}O$ films as compared to the as-grown samples.

Chapter 4. ZnO based UV SAW Device

The ZnO UV SAW device is based on a multi-layered structure, composed of semiconducting and piezoelectric ZnO thin films on r-Al_2O_3 substrates. The basic structure and operation principle of the device is presented. The device fabrication procedure and testing setup of the prototype UV SAW device are described in this chapter. In this analysis, the relationship between SAW response (phase shift and attenuation change) and the UV illumination (light wavelength and power density) is evaluated.

4.1 Device Structure and Operation Principle

The schematic vertical structure of a ZnO UV SAW device is shown in Figure 4.1. Based on the acoustoelectric interaction, the device is designed by integrating UV sensitive semiconducting ZnO layer with piezoelectric ZnO layer on r-Al_2O_3 substrates. The detailed bottom-up layer structure consists of a piezoelectric ZnO layer on r-Al_2O_3 substrate for SAW generation, an $Mg_{0.2}Zn_{0.8}O$ buffer layer, and a semiconducting ZnO sensing layer. These three layers are all grown by using MOCVD. A thick piezoelectric ZnO film (~2.0 μm) is firstly grown on r-Al_2O_3 substrates. As ZnO has a lower acoustic velocity than r-Al_2O_3, this layered system has dispersive acoustic velocity, with higher order wave modes excited at higher film thickness – frequency (hf) products. Based on the SAW simulation, the thickness is determined to ensure the excitation of the first higher order Rayleigh wave mode, the Sezawa wave mode, in the test devices below 1.0 GHz. The Sezawa wave mode is chosen as it has higher acoustic velocity, v_{SAW}, and maximum effective piezoelectric coupling, K^2_{eff}, than the base Rayleigh wave mode and the Love wave mode [99]. The as-grown, unintentionally doped MOCVD ZnO shows n-

type conductivity, with a carrier concentration of about ~10^{17} cm^{-3} [100]. To compensate the excess carriers in ZnO film and ensure efficient SAW excitation, the piezoelectric ZnO layer is doped with Li to increase its resistivity to above 10^7 Ω cm [101]. Then, a 50 nm thick $Mg_{0.2}Zn_{0.8}O$ buffer layer is used to isolate the semiconducting ZnO layer from the piezoelectric ZnO layer and as a diffusion barrier for Li. The semiconducting ZnO layer's thickness, h_{mesa}, varies from 200 nm to 400 nm to analyze the thickness dependence of the SAW and optical responses. After the formation of the semiconducting ZnO sensing mesa by wet chemical etching, the Al interdigital transducers are deposited and patterned on top of the piezoelectric ZnO surface.

For the horizontal device structure, there are three main parameters: the SAW wavelength λ, the delay line length L and the UV sensing mesa length L_{mesa}. The SAW wavelength λ determines the operating frequency of the UV SAW device and is determined by the periodicity of the IDT electrodes. Three wavelengths, 8, 12 and 16 μm, are chosen based on the photolithography constraints and the piezoelectric film thickness. The aperture of the IDTs is chosen to be 380 μm. The ZnO UV SAW devices are comprised of two sets, with delay lengths, L, of 1.2 mm and 1.7 mm, and corresponding mesa lengths, L_{mesa}, of 1.0 mm and 1.5 mm, respectively. Each set contains SAW devices with 8, 12 and 16 μm acoustic wavelength. The length of the sensing mesa L_{mesa} is chosen based on ensuring sufficient phase shift and insertion loss change under UV illumination. The devices are aligned parallel to the ZnO c-axis, which is in the surface plane of the $(11\bar{2}0)$ ZnO film, to generate the Rayleigh type wave modes. In the IDT region, the base Rayleigh wave mode has an estimated maximum coupling coefficient of 1.9% with a velocity of 2768 m/s, while the maximum coupling coefficient for the

Sezawa wave mode is estimated to be 6% with an acoustic velocity of 5658 m/s, leading to a larger photoresponse.

When the sensing area of the UV SAW device is illuminated by UV light, the incident light will be absorbed by the semiconductor, generating electron-hole pairs. Based on the acoustoelectric interaction, these free carriers in the semiconductor layer will interact with the electric field accompanying the propagating SAW, resulting in an increased insertion loss. Additionally, a velocity reduction will occur due to piezoelectric stiffening, resulting in a phase shift and time delay across the SAW device. These SAW response changes are correlated to the light wavelength and power density of the incident light and can be used as the UV sensing information.

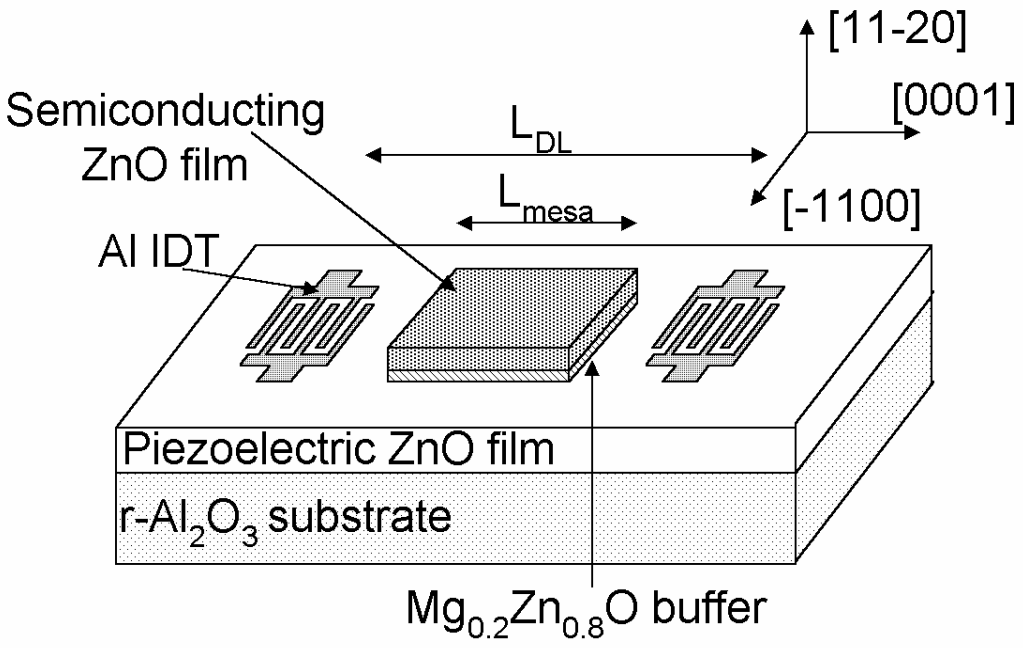

Figure 4.1 Schematic structure of UV SAW device.

4.2 Device Fabrication and Testing Setup

Figure 4.2 gives the flowchart of the ZnO UV SAW device fabrication. After the MOCVD growth of thick ZnO film (~2.0 μm), a post growth Li diffusion process is carried out to compensate the excess carriers. Then, the $Mg_{0.2}Zn_{0.8}O$ buffer layer and ZnO UV sensing layer are grown by MOCVD in sequence.

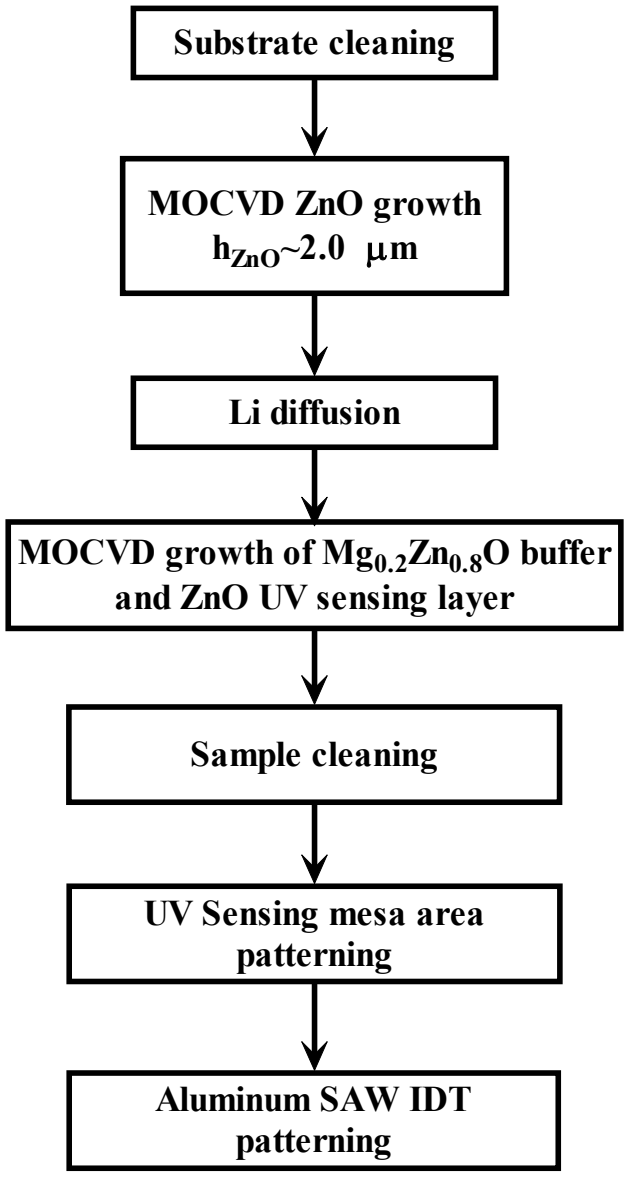

Figure 4.2 ZnO UV SAW device fabrication flow chat

4.2.1 Li Diffusion of the ZnO Film

The as grown ZnO film by MOCVD technique shows n-type semiconductor property. In order to compensate the excess carriers for piezoelectric applications, post-growth Li diffusion was carried out with solid LiOH powder as the diffusion source. The Li diffusion was performed in a close tube at 500~550 ^{o}C. The diffusion time was varied from 1hr to 2 hrs based on the thickness of the ZnO film. The Li doped piezoelectric ZnO layer increased its resistivity to above 10^7 Ω.cm, in order to ensure efficient SAW excitation. During the primary Li diffusion investigation, solid particle contamination was found on the surface of the ZnO film [101]. These solid particles increase the scattering of the SAW wave and introduce excess insertion loss to the device. The SAW testing results indicate the insertion loss of both basic Rayleigh and Sezawa wave mode are about -60 dB. To improve the SAW performance, optimization of the diffusion process was carried out by optimizing diffusion tube setup and diffusion temperature. A sample holder was inserted between the diffused sample and the diffusion box to avoid particle accumulation during the cooling period. With the optimized diffusion setup, the diffused ZnO samples show similar surface roughness as the as-grown film and there is no observable particle contamination, which is important to the low loss SAW performance.

To evaluate the effect of the Li diffusion process, SAW devices have been fabricated on the diffusion piezoelectric ZnO film and multi-mode SAW responses have been evaluated. Two sets of SAW test devices were fabricated on ZnO/ r-Al_2O_3. The delay line lengths, L_{DL} were chosen to be 1200 μm and 1700 μm, respectively. Each set

contains four devices, with wavelengths of 6, 8, 12 and 16 μm. The aperture of the IDTs was chosen to be 380 μm. To excite the Rayleigh-type wave, the test devices were placed along the c-axis of the ZnO film (in the direction of the [0001]).

The device fabrication process consisted of electron-beam evaporation of ~120 nm of Al, followed by photolithography and Al etching to define the IDTs. The fabricated devices were characterized using a HP8753D network analyzer and Cascade Microtech probes. The measurement results were time gated by using Matlab to identify the SAW response, and to eliminate electromagnetic feed through, BAW responses, and secondary effects such as triple transit interference.

Figure 4.3 shows SAW response of a SAW device made on a MOCVD grown ZnO film (with post-growth Li diffusion). The device wavelength is 8 μm with the delay length of 1.7 mm. The thickness of the ZnO film is ~2.0 μm to ensure the Sezawa wave mode excitation. This device is aligned parallel to the c-axis of ZnO film. Multi-mode SAW responses have been observed in Figure 4.3. The basic Rayleigh wave mode is at center frequency of ~553 MHz, with an insertion loss of ~-49.3 dB. The SAW velocity is ~ 4424 m/s. Sezawa wave is observed at center frequency of 711 MHz with insertion loss of ~-31.5 dB. The SAW velocity is ~5688 m/s.

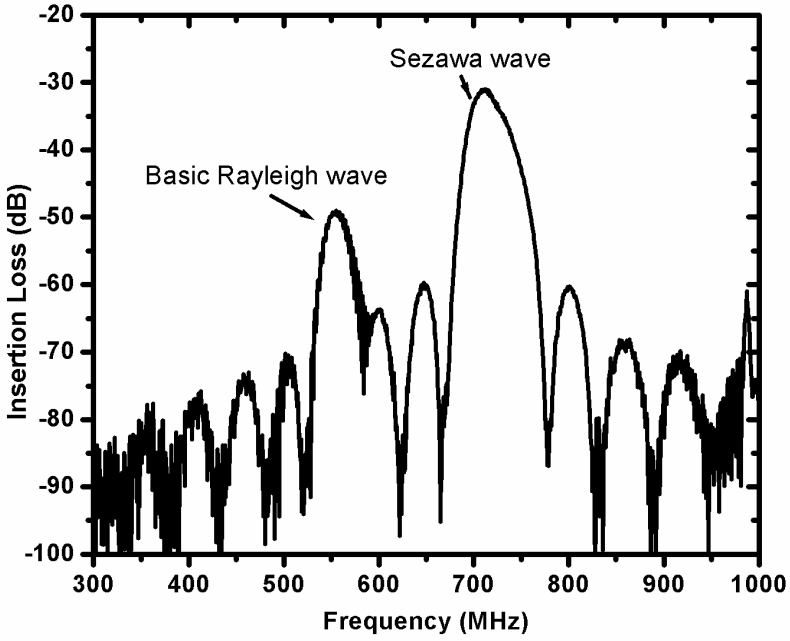

Figure 4.3 Rayleigh and Sezawa wave mode on a Li diffused 2.0 μm MOCVD grown ZnO film

4.2.2 UV SAW Device Fabrication Procedure

After the finish of the material growth and diffusion, the UV SAW device fabrication procedure mainly involves 1) Sample cleaning; 2) sensing area patterning; and 3) SAW aluminum IDT patterning. Multiple processing techniques are used in the device fabrication including photolithography, ZnO thin film etching, metallization and metal etching.

In the sensing mesa etching, beside the pattern profile, the ZnO etching is controlled for two purposes: 1) the area outside of the mesa needs to be etched to the piezoelectric surface. Because the MOCVD grown ZnO UV sensing layer is semiconducting, it reduces the surface resistivity of SAW propagating path and results large insertion loss. Therefore, the secondary grown ZnO semiconducting layer needs to be removed outside of the sensing mesa and the Al IDT electrode needs to be patterned on top of the Li diffused piezoelectric ZnO surface; 2) the etch thickness of the area outside of the mesa needs to be controlled. Based on the SAW simulation, the remaining thickness of the piezoelectric ZnO layer needs to be close to 2.0 μm for Sezawa wave mode generation, larger local ZnO coupling K^2_{IDT} and corresponding higher UV sensitivity based on the acoustoelectric interaction. The wet chemical etching technique described in chapter 3 has been used in the ZnO sensing mesa fabrication.

The microscopic images of a prototype ZnO UV SAW device are shown in Figure 4.4 (a) Top view of the UV SAW device; (b) Al IDT electrodes; and (c) UV sensing mesa area.

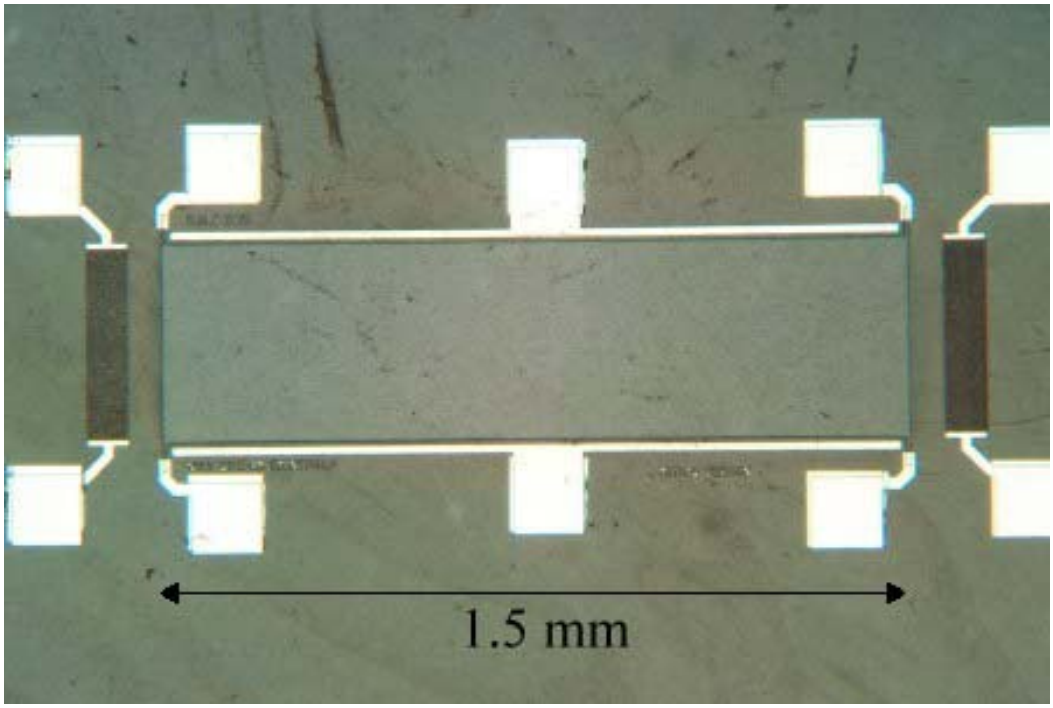

(a)

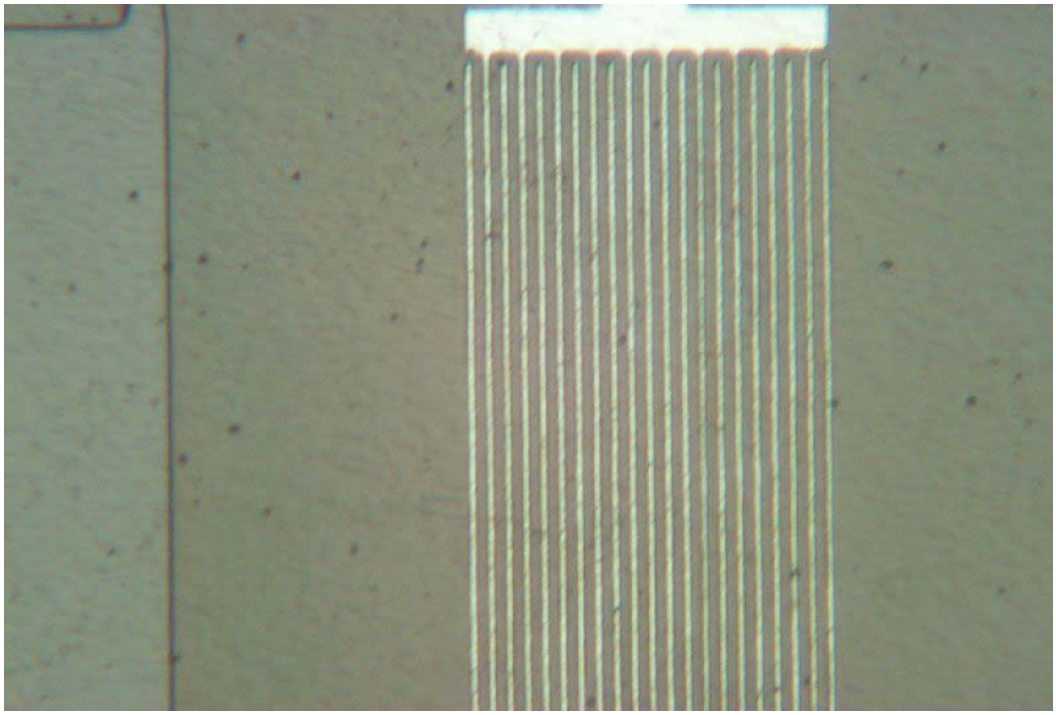

(b)

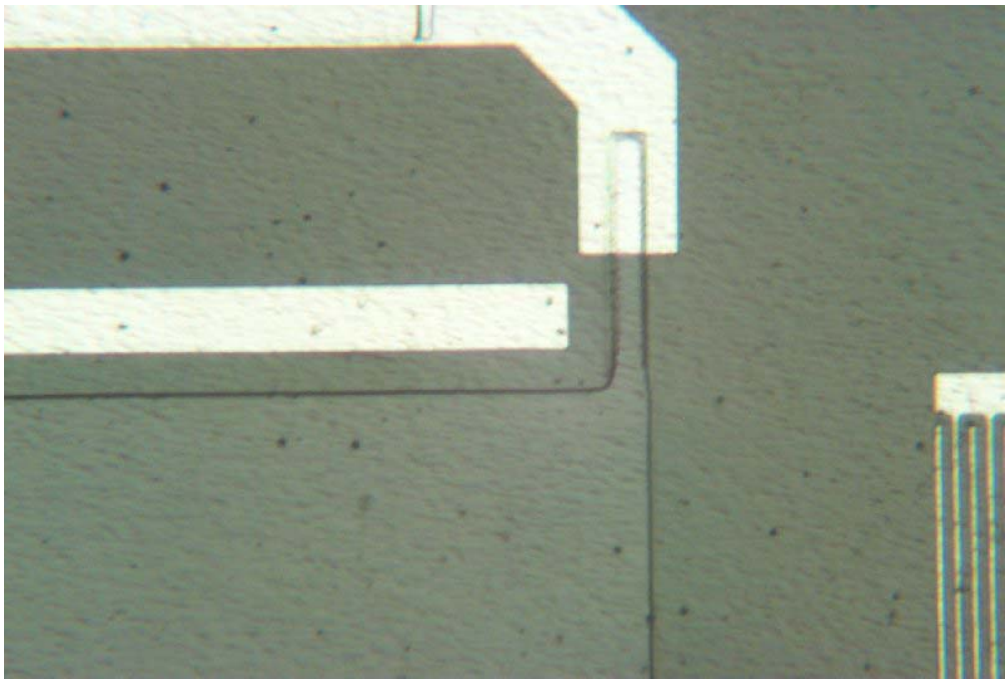

(c)

Figure 4.4 Optical microscopic images of the UV SAW device, (a) Top view of the UV SAW device; (b) Al IDT electrodes; (c) UV sensing mesa area

4.2.3 UV SAW Testing Setup

The ZnO SAW UV devices were tested using an HP 8753D network analyzer and Cascade Microtech probes for the RF response (the transmission parameter S_{21}). The ZnO UV SAW device was firstly evaluated under the dark condition and microscope light. Then, a 75W Xe lamp with a monochromator system was used as the UV source for detailed UV detection evaluation. Multiple UV filters were used to adjust the power density of the incident light. Two optical illumination procedures were used, illuminating the whole device surface and only illuminating the semiconducting ZnO mesa through a shadow mask, as shown in Figure 4.5. The light wavelengths were varied from 630nm to 300 nm. The light power density was varied from 810 $\mu W/cm^2$ to 2.32 mW/cm^2 at λ_{light} = 365 nm. I-V measurements were used to determine the change in the resistance of the mesa active layer as a function of the light wavelength and power, then correlated with the SAW photoresponse.

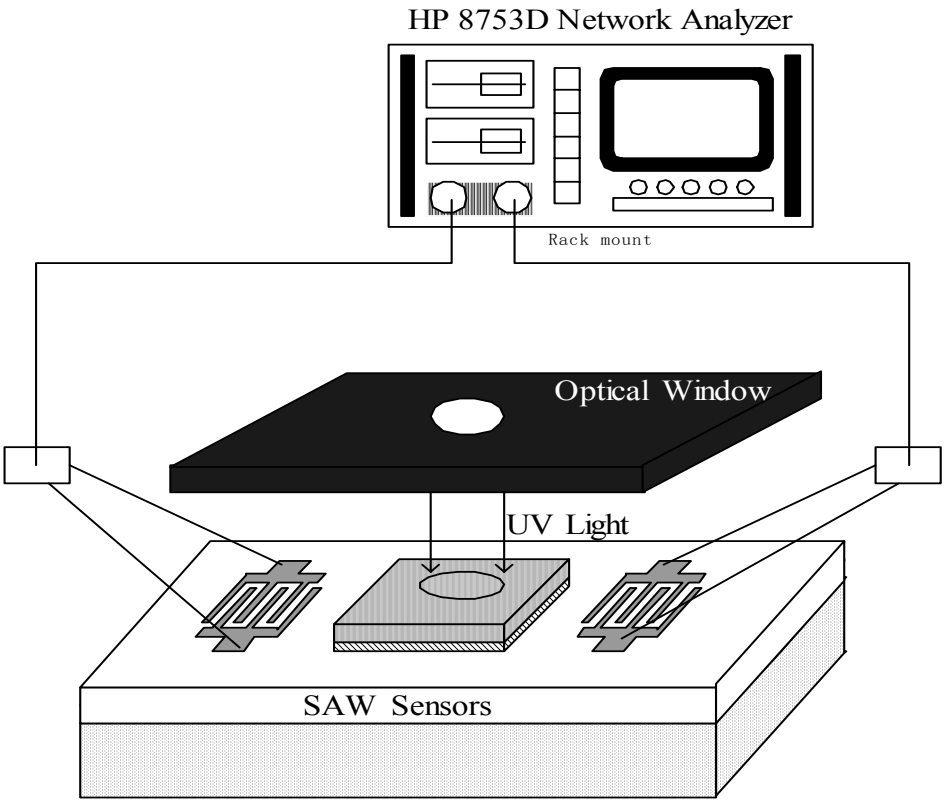

Figure 4.5 Schematic of the UV SAW testing setup

4.3 UV Detecting Evaluation of the Prototype ZnO UV SAW Device

Figure 4.6 shows the SAW response of a UV SAW device with λ_{SAW} = 8 μm, L = 1 mm, and h_{mesa} = 300 nm, under dark and two different light power conditions (λ_{light} = 365 nm), while using a shadow mask to limit the illuminated area to the mesa. The power density of the incident light was adjusted by applying UV filters to the light beam. The base Rayleigh wave mode response is at 545.9 MHz, with an insertion loss of -67.8 dB. In comparison, the Sezawa wave mode response is at 711.3 MHz, corresponding to v_{SAW} = 5690 m/s, with an insertion loss of -52.5 dB. The Sezawa wave insertion loss increases to -75.3 dB when the light power is 2.32 mW/cm^2, while the Rayleigh wave insertion loss is -83.3 dB. In comparison, the UV SAW detector with a 200 nm thick active region had an insertion loss of -33.8 dB for the Sezawa wave mode, due to its lower conductance. The insertion loss can also be improved by using better designed IDTs with narrower bandwidth and unidirectional transducers. When the whole device surface is illuminated, a shift in center frequency, up to 11 MHz, along with additional phase shift and insertion loss, was observed. This is due to the generation of carriers in the Li-doped piezoelectric ZnO layer under the IDTs, whose high resistivity (>10^7 Ω.cm) is insufficient to totally suppress carrier generation.

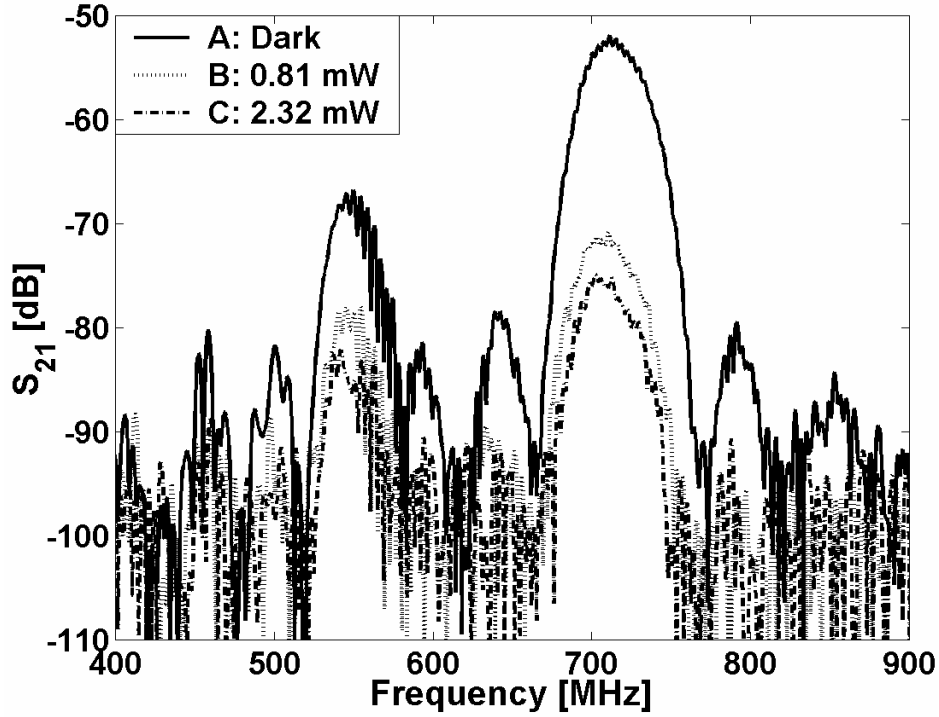

Figure 4.6. Frequency response of the SAW UV detector under 365 nm light illumination, under dark, 0.81 mW/cm^2 and 2.32 mW/cm^2 conditions.

The phase shift at center frequency for the Sezawa wave mode with respect to the dark condition, as a function of light wavelength and power level, is shown in Figure 4.7. The inset shows the transmission spectrum of ZnO epi-layer grown on r-Al_2O_3 for comparison. The power density level of each curve (A-D) is summarized in table 4.1.

From Figure 4.7, it can be seen that the UV SAW device response closely follows the absorption spectrum. For light wavelengths above 400 nm, the phase shift is small. The phase shift increases rapidly as the light wavelength approaches the band edge at about 372 nm. The phase shift at 365 nm for a light power of 2.32 mW/cm^2 is 107°, corresponding to a frequency shift of 1.36 MHz in an oscillator circuit, calculated for the standard oscillator circuit configuration with the SAW in the feedback path:

$$\Delta f = \frac{1}{\tau}\frac{\Delta\phi}{360^o} = \frac{1}{\frac{L_{mesa}}{v_{SAW,mesa}} + \frac{L_{IDT}}{v_{SAW,IDT}}}\frac{\Delta\phi}{360^o}$$

where τ is the delay time across the device, $v_{SAW,mesa}$ the acoustic velocity in the mesa region, $v_{SAW,IDT}$ the acoustic velocity in the IDT region, L_{IDT} the delay path length in the IDT region, and $\Delta\phi$ the phase shift across the device. The Sezawa wave velocity in the mesa region, $v_{SAW,mesa}$, is estimated to be 5430 m/s. This 1.36 MHz frequency shift corresponds to a 0.19% relative shift for a light power of 2.32 mW/cm^2, which compares favorably with the 0.46% relative frequency shift at 40 mW/cm^2 reported for a ZnO/$LiNbO_3$ SAW UV detector [19]. The estimated effective coupling, k_{eff}^2, at hf = 1710 is 1.6%, calculated using the transfer matrix method [102]. It is estimated that the maximum effective coupling that could be obtained for this structure is 3.2% at hf = 2820. Thus, device performance can be improved by operating at a higher frequency using a smaller SAW wavelength.

Figure 4.8 shows the differential insertion loss for the Sezawa wave mode with respect to the dark condition, as a function of light wavelength and power level. The data has been normalized for constant power on the device. As the light wave approaches the band edge, at about 372 nm, the differential insertion loss rapidly increases, similar as the phase shift changes. At 365 nm, the differential insertion loss for the Sezawa mode under 2.32 mW/cm^2 illumination is 22.8 dB.

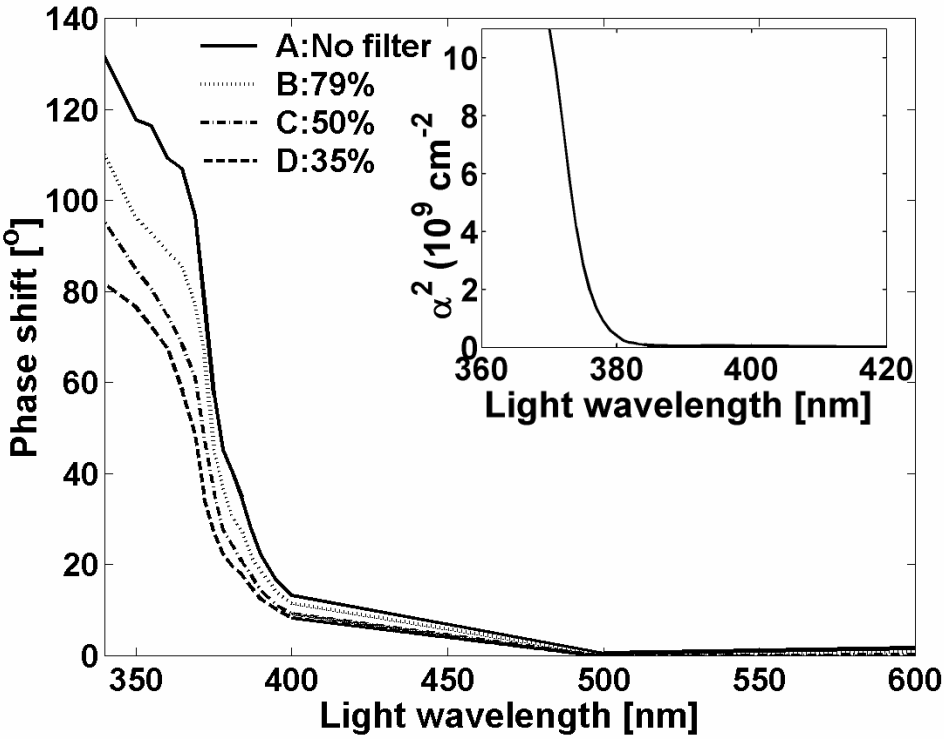

Figure 4.7. Phase shift vs. light wavelength for light power of 2.32 mW/cm^2, 1.83 mW/cm^2, 1.18 mW/cm^2, and 0.81 mW/cm^2. The responses have been normalized for constant power with respect to 365 nm. The inset shows the absorption spectrum of a ZnO thin film on r-Al_2O_3.

Curve ID	Filter ID	Power density ratio	Actual power density (mW/cm^2)
A	No filter	100%	2.32
B	Filter 1	79%	1.83
C	Filter 2	50%	1.18
D	Filter 3	35%	0.81

Table 4.1 Power density level of the each measurement

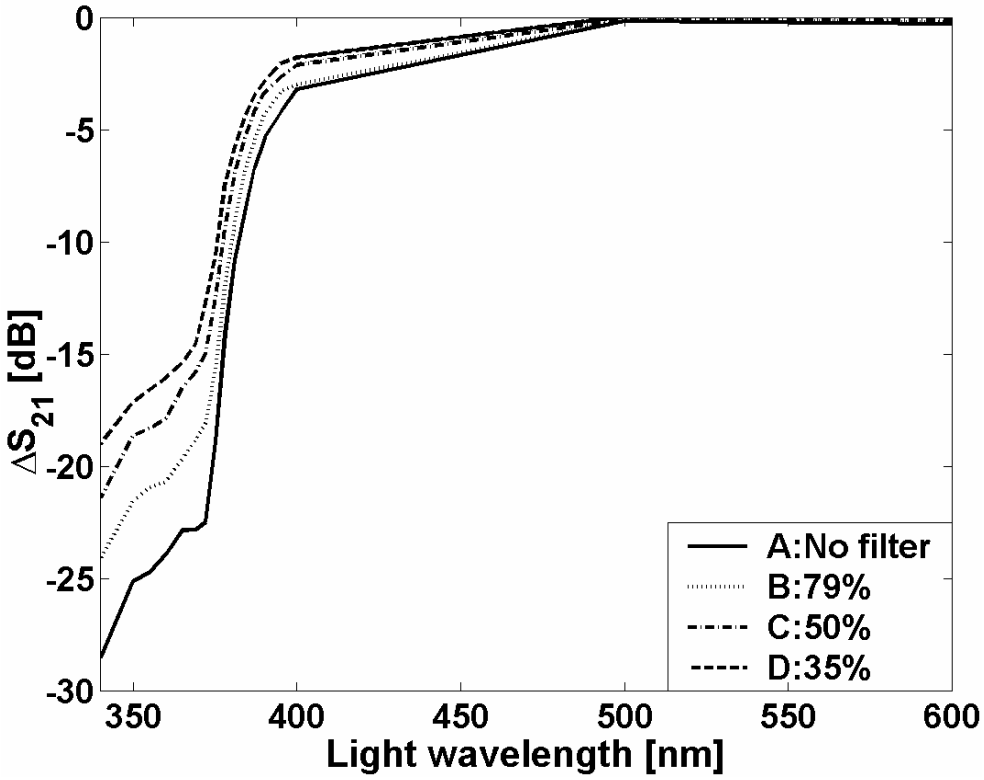

Figure 4.8 Differential insertion loss vs. light wavelength for light power of 2.32 mW/cm^2, 1.83 mW/cm^2, 1.18 mW/cm^2, and 0.81 mW/cm^2. The responses have been normalized for constant power with respect to 365 nm.

4.4 Summary

Based on the acoustoelectric interaction, a prototype ZnO based UV SAW device is designed and demonstrated by using epitaxial ZnO multilayers grown on r-Al_2O_3 substrates, where piezoelectric and semiconducting ZnO layers separated by a $Mg_{0.2}Zn_{0.8}O$ buffer layer are used for SAW excitation and photodetection, respectively. The ZnO/r-Al_2O_3 system possesses a high acoustic velocity and large maximum effective coupling constant obtainable with the Sezawa wave mode, in comparison with the previously reported GaN/c-Al_2O_3 and ZnO/$LiNbO_3$ structures. The interaction of the SAW with the photogenerated carriers in the semiconducting ZnO layer results in a phase shift and an insertion loss change, as functions of light wavelength and power. The SAW UV detector can be used as a passive zero-power remote wireless sensor.

Chapter 5. ZnO based Multimode Tunable SAW Device

To fulfill the requirement of the adaptive communication and tunable sensor, a ZnO based multimode tunable SAW device is designed, fabricated and demonstrated in this research. The basic structure of the ZnO tunable SAW device consists of a ZnO SAW device integrated with a SiO_2/semiconducting ZnO MIS structure. The device fabrication procedure is described in this chapter. The performance of the prototype device is evaluated with respect to the acoustic velocity tunability, device phase shift, attenuation change and external bias. The comparison between the measured and simulated results are presented and discussed based on the acoustoelectric interaction model.

5.1 Device Structure and Operation Principle

The structure of a prototype ZnO based multimode tunable SAW device is schematically described in Figure 5.1. In this device, r-Al_2O_3 substrate is used as the substrate material instead of the popular c-plane sapphire for the following three advantages:

(i) The c-axis of the ZnO film in the ZnO/r-Al_2O_3 material system is in-plane, resulting in unique anisotropic acoustic, optical, and electrical properties;

(ii) The system has higher electromechanical coupling coefficients, with K^2 up to 6% for certain wave modes;

(iii) Lattice mismatch between ZnO and r-plane sapphire is less than that in ZnO/c-plane sapphire, resulting in high quality ZnO thin films.

The piezoelectric ZnO film is firstly deposited on r-Al_2O_3 substrate for SAW generation. Based on the SAW simulation, the thickness of the piezoelectric ZnO film is

determined from 2.0 μm to 2.5 μm to (1) guarantee the excitation of the multiple wave modes, i.e., Sezawa and Love mode; (2) achieve maximal electromechanical coupling coefficient; and (3) supply enough processing tolerance. After the formation of the piezoelectric ZnO film, a semiconducting ZnO film is re-grown on top of the piezoelectric surface as the conducting channel by using MOCVD. To form the MIS structure, a semiconducting ZnO mesa pattern is formed in the delay line region using a diluted HCl solution and then a SiO_2 layer is deposited by PECVD and patterned as the gate insulator. The thicknesses of the semiconducting ZnO channel and the SiO_2 gate insulator are determined as ~100 nm and ~200nm, respectively, based on the consideration of required depletion bias, effective coupling coefficient, processing tolerance, electrical breakdown voltage and mesa step coverage. The interdigital transducers (IDTs) on the piezoelectric ZnO and the non-alloyed ohmic contacts to the n-type ZnO layer are formed by aluminum deposition and etching. The gate electrode is formed on top of the SiO_2 using aluminum deposition and lift off process.

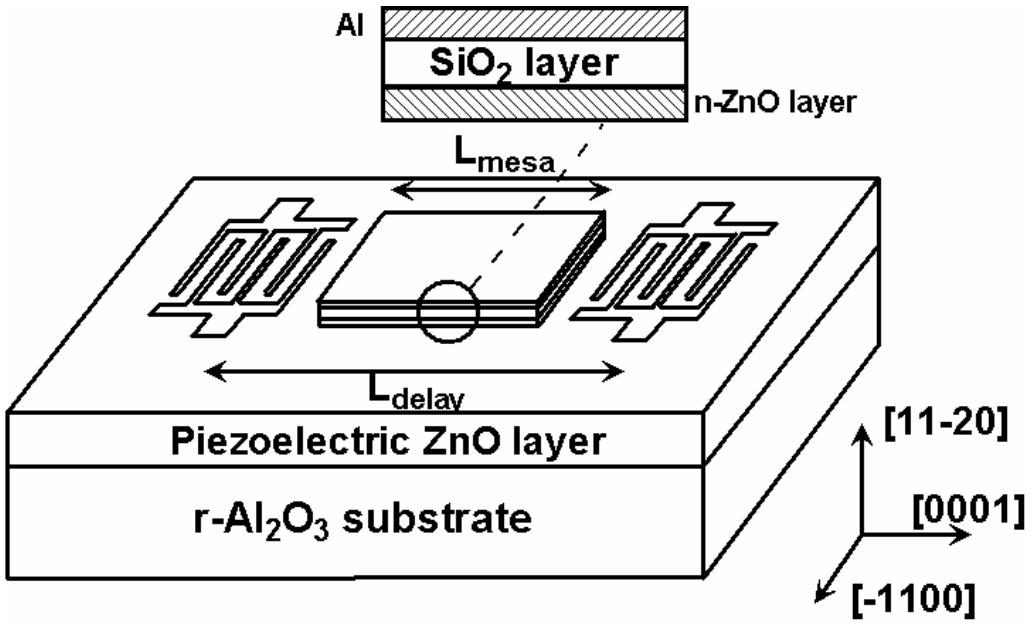

Figure 5.1 Schematic representation of the ZnO based tunable SAW device structure. The inset shows a cross-section view of an Al/SiO_2/ZnO (MIS) structure built on the piezoelectric ZnO.

In the vertical structure design of the ZnO tunable SAW device, the dimension of the top MIS structure is of importance to the overall device performance. Firstly, the thicknesses of the semiconducting ZnO channel and SiO_2 gate insulator are directly related to the required bias to efficiently adjust the carrier density in the channel and the corresponding acoustic velocity change based on the acoustoelectric interaction. Secondly, during the operation of the ZnO tunable SAW device, the top electrode of the MIS structure will screen the SAW potentials, suppress the interaction with the conducting channel and impact the device performance. The effective coupling coefficient K_{eff}^2 in the delay line region is not only determined by the piezoelectric layer's material property, but also influenced the screen effect of the top electrode and the mass loading of the gate insulator, which is related to the distance between the top electrode and ZnO channel. For the tunable SAW device operation, this effective coupling coefficient K_{eff}^2 is used in the acoustoelectric interaction model, instead of the SAW coupling coefficient of the IDT region. In the ZnO tunable SAW device, the distance between the top electrode and the ZnO channel is defined by the thickness of the gate insulator, i.e. SiO_2. When the distance between the top electrode metal and ZnO channel is small, the screen effect becomes severe and the effective coupling coefficient decreases. Based on the acoustoelectric interaction model, the maximal velocity tunability $\Delta v/v_0$ of a tunable device is of $K_{eff}^2/2$. Although with thinner gate insulator, the required bias for channel depletion can be reduced, due the reduced effective coupling coefficient resulting from the screen effect of the top electrode, the maximal velocity tuning range will decrease correspondingly; even when the channel can be fully depleted, i.e. the sheet conductivity becomes zero.

Therefore, in the tunable SAW device design, both the bias and effective coupling coefficient issues need to be considered to optimize the overall device performance.

Transfer matrix method [102] is used to simulate the relationship among the gate insulator thickness, SAW phase velocity and the effective coupling coefficient. The simulation multilayer layer structure is Al/SiO_2/ZnO channel/piezo-ZnO/r-Al_2O_3. To simplify the simulation, the ZnO channel has been approximated to be a thin carrier sheet between the SiO_2 and piezoelectric ZnO layer. The open circuit phase velocity v_o and short circuit velocity v_s are simulated, corresponding to the situation when the sheet conductance is zero (fully depletion) and the sheet conductance is infinite (conducting), respectively. Then, the effective coupling coefficient K_{eff}^2 is calculated based on: $K_{eff}^2 = \frac{-2(v_s - v_o)}{v_o}$. In the simulation, the Al electrode is defined on top of SiO_2 layer in both the situations when the channel sheet conductance is zero or infinite. This simulation is an approximation to select the SiO_2 thickness for the prototype ZnO tunable SAW device. In the operation of ZnO tunable SAW device, the ZnO channel has thickness d and the bias induced depletion changes the channel thickness. Under different biases, the acoustic velocity simulation is more complex. Under certain bias, instead of simplified Al/SiO_2/carrier sheet/piezoelectric ZnO/r-Al_2O_3 structure, the actual layer structure becomes Al/SiO_2/depleted ZnO/semiconducting ZnO/Piezoelectric ZnO/r-Al_2O_3. The varied thickness and position of the semiconducting ZnO channel and depletion layer will all impact the acoustic velocity change.

Figure 5.2 shows the simulation results of a) the phase velocity (open and short circuit) and b) effective coupling coefficient with different insulator thickness (250 nm, 100 nm and 25 nm) for Sezawa wave mode as function of the SAW center frequency.

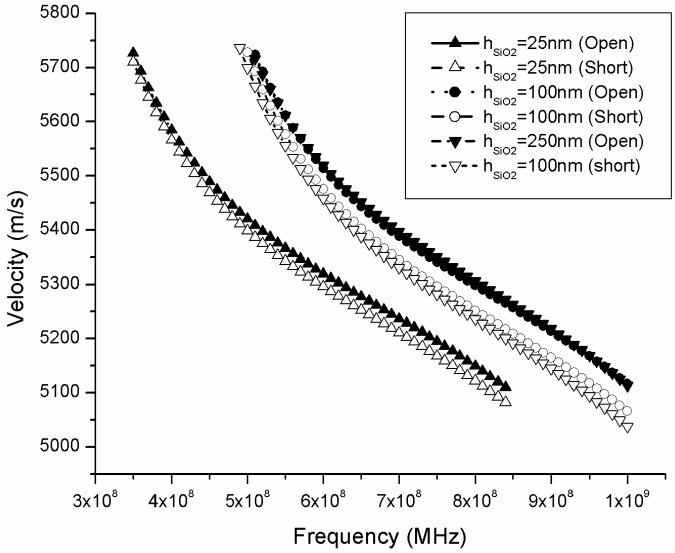

(a)

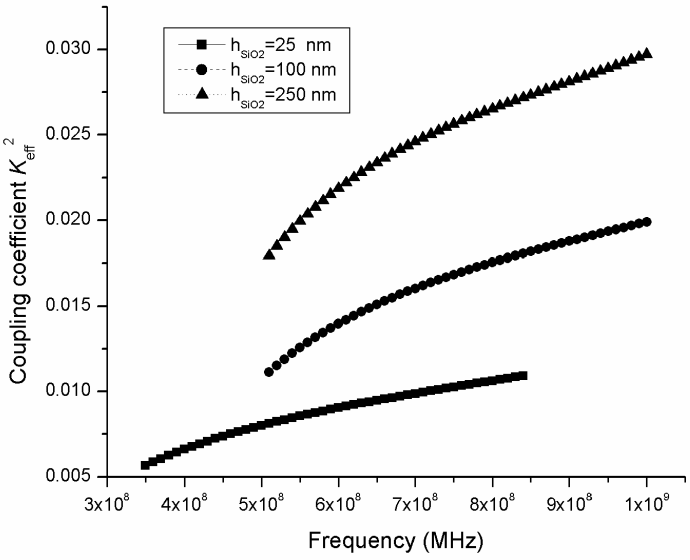

(b)

Figure 5.2. (a) Phase velocity (open and short circuit) and (b) the effective coupling coefficient with different oxide thickness. Wave mode: Sezawa mode. ZnO thickness: 2.4 μm

In the simulation, the thickness of the piezoelectric ZnO layer is defined as ~2.4 μm and the gate insulator is defined as SiO_2. From Figure 5.2 (b), it can be seen that the effective coupling coefficient drops quickly with the decrease of the insulator thickness. Based on the simulation and SAW testing results, the center frequency of a SAW device with wavelength of 8 μm is of ~700 MHz, for a ~2.4 μm piezoelectric ZnO film on r-Al_2O_3 substrate. From Figure 5.2 (b), at frequency 700 MHz, for SiO_2 with thickness of 25, 100 and 250 nm, the simulated effective coupling coefficients are 1.0%, 1.6% and 2.5%, respectively. The maximal acoustic velocity tuning ranges can be determined as 0.5%, 0.8% and 1.25%, correspondingly. The simulation results indicate that the thickness of the SiO_2 has dynamic influence to the effective coupling coefficient and corresponding velocity tunability. With the decrease of the SiO_2 thickness, the maximal acoustic velocity tuning range will decrease.

In addition to the effective coupling coefficient simulation, the relationship between the required bias for the ZnO channel depletion and the thickness of SiO_2 is also calculated based on the MIS structure model. The parameters used in the calculation are listed in Table 5.1. The intrinsic carrier concentration n_i of ZnO is given by equation:

$$n_i = 2(\frac{2\pi kT}{h^2})^{3/2}(m_e * m_h *)^{3/4} \exp(\frac{-E_g}{2kT}) \tag{5.1}$$

where k is the Boltzmann constant, h is the Planck's constant, T is the temperature, m_e* and m_h* are the effective masses of the electron and hole, respectively. E_g is the band gap energy of ZnO.

The energy separation ϕ_F between E_i (the Fermi level of intrinsic ZnO) and E_F (the Fermi level of n-type ZnO) is given by:

$$\phi_F = -\frac{kT}{q}\ln\frac{N_D}{n_i} \tag{5.2}$$

where, , N_D is the donor concentration.

The depletion width of the MIS structure can be calculated as:

$$W = \sqrt{\frac{-2\varepsilon\phi_s}{qN_D}} \tag{5.3}$$

The maximal depletion width of a n-type ZnO film can then be determined by setting surface potential $\phi_s=2\phi_F$ (the condition of strong inversion) as:

$$Wm = \sqrt{\frac{-4\varepsilon\phi_F}{qN_D}} \tag{5.4}$$

The calculated maximal depletion width of n-type ZnO film is ~135 nm. In the ZnO tunable SAW device design, the thickness of the semiconducting ZnO film is selected as 100 nm. Therefore, the relationship between the bias and depletion width is governed by equations used under the depletion condition. The derivation has been given as follows:

With a gate bias V_G, we have:

$$V_G = V_{FB} + V_{ox} + \phi_s \tag{5.5}$$

where V_{FB} is the flat band voltage and V_{ox} is the voltage dropped across the gate oxide.

To simplify the calculation, we ignore the oxide charge Q_i, and then the flat band voltage equals to the work function difference between the aluminum and n-type ZnO:

$$V_{FB} = \Phi_{ms} - \frac{Q_i}{C_{ox}} = \Phi_{ms} \tag{5.6}$$

and the expression of V_{ox} is given by:

$$Vox = -\frac{Q_d}{C_{ox}} = -\frac{\sqrt{-2qN_D\varepsilon\phi_s}}{C_{ox}} \tag{5.7}$$

By introducing Eq.(5.6), (5.7) into Eq.(5.5), we have:

$$V_G = \Phi_{ms} - \frac{\sqrt{-2qN_D\varepsilon\phi_s}}{C_{ox}} + \phi_s \tag{5.8}$$

$$(-\phi_s) + \frac{\sqrt{2qN_D\varepsilon}}{C_{ox}}\sqrt{(-\phi_s)} + (V_G - \Phi_{ms}) = 0 \tag{5.9}$$

By setting $-\phi_s = y^2$ and solving Eq.(5.9), we can get the solution of ϕ_s as function of V_G. By introducing the values of ϕ_s into Eq.(5.3), the relationship between gate bias V_G and corresponding depletion width W can be solved. This relationship is calculated by introducing various SiO_2 thicknesses and setting the ZnO channel thickness as 100 nm. Table 5.2 gives the summarized calculation results. From Table 5.2, it can be seen that the thickness of SiO_2 has close relation with the required bias to deplete the ZnO channel and the voltage dropped across the SiO_2 takes the major part of the total bias. With the decrease of the SiO_2 thickness, the required bias for channel depletion also decreases. In this calculation, the influence of the oxide charge has been ignored. However, in the real ZnO tunable SAW devices, the oxide charge and interface states at SiO_2/n-ZnO and n-ZnO/piezo-ZnO interfaces will further increase the required bias to deplete the channel. In the ZnO tunable SAW device design, the desired operation mode is with low bias and large velocity tunability. By considering the required depletion bias and effective coupling coefficient, along with other factors, such as the processing tolerance, electrical breakdown voltage and mesa step coverage, the thicknesses of the ZnO channel and SiO_2 gate insulator are selected as ~100 nm and ~200 nm in the prototype ZnO tunable SAW device fabrication, respectively.

		Reference
Eg (eV) (300K)	3.4	[103]
ε_{ZnO}	8.12	[104]
m_e^*	$0.318m_0$	[104]
m_h^*	$0.5m_0$	[105]
$q\chi_{ZnO}$ (eV)	4.29	[106]
N_D (cm^{-3})	1.6×10^{17}	
$q\Phi_{Al}$ (eV)	4.1	
m_0 (kg)	9.11×10^{-31}	
k (J/K)	1.38×10^{-23}	
ε_0 (F/cm)	8.85×10^{-14}	
q (C)	1.6×10^{-19}	
T (K)	300	
ε_{SiO2}	3.9	
h (J-s)	6.626×10^{-34}	

Table 5.1. Parameters used in the bias and depletion width calculation of the SiO_2/n-ZnO MIS structure.

	The thickness of SiO_2				
	100nm	**150nm**	**200nm**	**250nm**	**300nm**
V_G (V)	-9.9	-13.7	-17.2	-21.0	-24.8

Table 5.2. The required biases in the MIS structure to deplete 100 nm n-type ZnO channel with different SiO_2 thicknesses.

The horizontal structure of the ZnO tunable SAW device is shown in Figure 5.3. There are two sets of tunable SAW devices, with delay lengths, L, of 1.2 and 1.7 mm, corresponding to mesa length L_{mesa}, of 1.0 and 1.5 mm, respectively. The delay lengths and mesa lengths are chosen to achieve sufficiently large acoustic velocity change or phase shift for multiple wave modes, i.e. Sezawa and Love mode. Three wavelengths, 8, 12 and 16 μm, were chosen based on the photolithography constraints and the piezoelectric film thickness. Quarter-wavelength (λ/4) IDTs are used in the devices with λ = 8 μm. The width of a signal electrode and the gap between the electrodes are 2 μm. Split-electrode (λ/8) IDTs are used for the λ = 12 and 16 μm devices, in order to reduce the inter-electrode reflections. The aperture of the IDTs was chosen to be 380 μm.

In the ZnO/r-Al_2O_3 system, two types of wave modes, the Rayleigh-type and the Love-type can be excited by aligning the SAW propagation either along the c-axis (Rayleigh mode, || [0001]) or perpendicular to the c-axis of the ZnO film (Love mode, || $[\bar{1}100]$), respectively. The shear vertical (SV) component in Rayleigh-type wave mode offers high mass sensitivity for gaseous-environment sensing while the shear horizontal (SH) component in Love wave reduces the acoustic attenuation when contacting to a liquid, and is therefore ideal for liquid- environment sensing. In the ZnO based tunable SAW device, the first higher-order Rayleigh mode (Sezawa wave) and Love wave mode are used instead of using base Rayleigh wave mode, as they possess larger effective piezoelectric coupling coefficients. In order to realize multimode operation, the tunable SAW devices are aligned in two directions, i.e. parallel to the ZnO *c*-axis for Sezawa mode and perpendicular to the ZnO *c*-axis for Love mode operation.

The acoustic velocity tunability of the ZnO tunable SAW device is based on the acoustoelectric interaction between the electric field accompanying the propagating SAW and free carriers in the semiconducting channel. Under zero gate bias, the sheet charge density of the semiconducting ZnO channel is high, the SAW will propagate with an initial acoustic velocity and modified by the mass-loading effect of the SiO_2/Semiconducting ZnO stack and the screening effect of the gate electrode. When the electrons in the ZnO channel are depleted due to the reverse gate bias, the SAW will propagate with the open-circuit velocity v_{oc}, again modified due to the mass loading and gate electrode screening effects. When the ZnO channel is in the accumulation stage due to the forward bias, the electron density increases to very high level, the SAW will propagate with the slower short-circuit v_{sc} velocity. For intermediate sheet charge densities with the change of the gate bias, the SAW's electric field will generate current in the channel, resulting ohmic loss, and will propagate at a velocity v, which is between v_{oc} and v_{sc}. The value of v will be determined by the charge density, the effective coupling of the structure, and v_{oc}. In principle, the channel can be made either single layer semiconductor or two dimensional electron gas (2DEG) system, which offers larger tunable range and lower bias. Both MS and MIS structure can be used to control the charge density in the channel. In this work, based on the consideration of device processing, material growth, and device reliability, single semiconducting ZnO channel and SiO_2/ZnO MIS structure are used in the prototype tunable SAW devices.

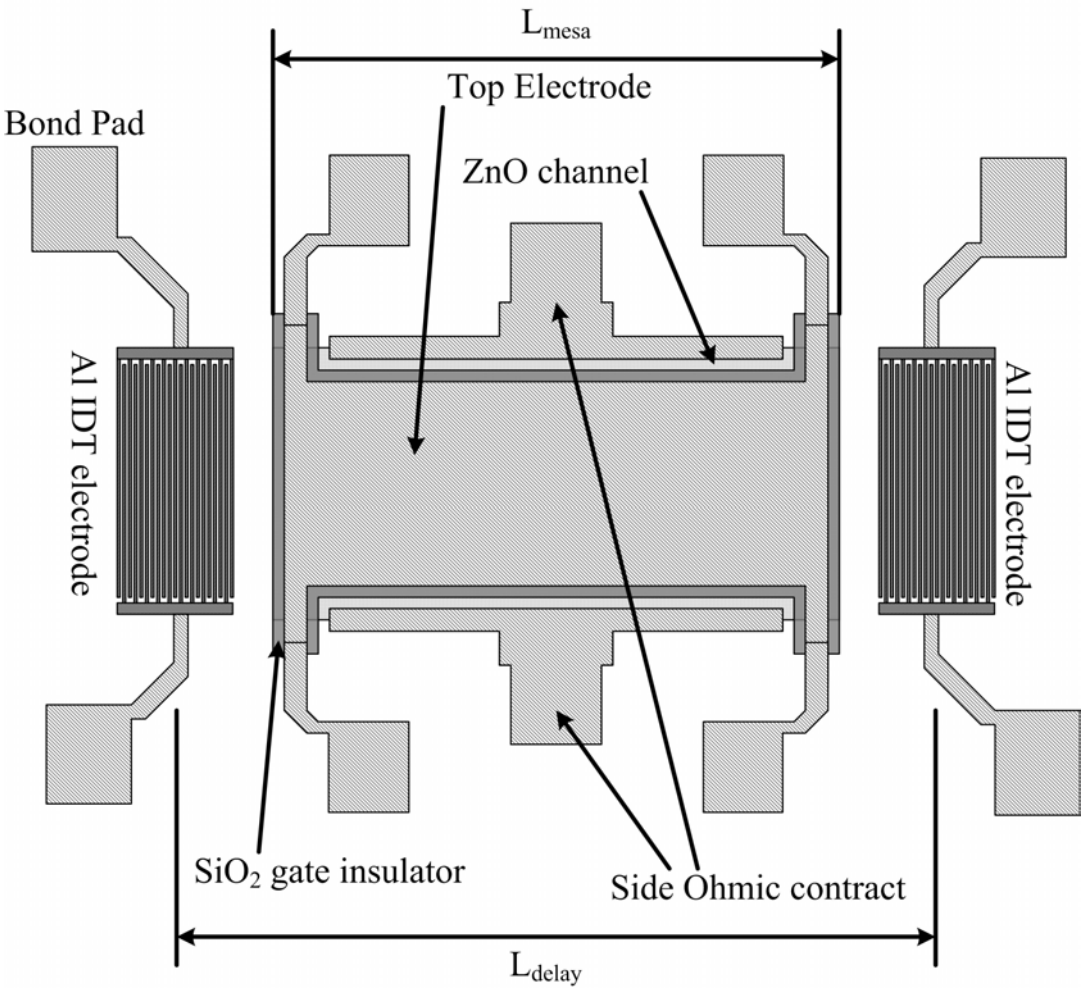

Figure 5.3 Schematic horizontal structure of the ZnO tunable SAW device

5.2 Hybrid Piezoelectric ZnO Film Deposition

In the development of the ZnO tunable SAW device, the growth of the thick piezoelectric ZnO film (~2.0μm) is of critical importance. The thickness of the piezoelectric layer determines the excitation of the multiple wave modes and maximal effective electromechanical coupling coefficient. The uniformity and surface roughness of the piezoelectric layer impact the insertion loss of the SAW and the interface quality between piezoelectric and semiconducting ZnO layer. In the development of the ZnO tunable SAW device, the thick piezoelectric ZnO film was initially grown by MOCVD and with post growth Li diffusion. However, the processed prototype device showed a relative large insertion loss and small acoustic velocity tunability. To improve the piezoelectric ZnO film growth and meanwhile keep the in-plane piezoelectric anisotropy for multi-mode SAW operation, a hybrid RF sputtering-MOCVD deposition method has been developed.

In the MOCVD growth of thick ZnO and $Mg_xZn_{1-x}O$ films, one of the major obstacles is the gas phase reaction. The reactions between DEZn, CP_2Mg, and oxygen can occur even at room temperature. The gas phase reaction generates particles, which get incorporated into the deposited films, degrading film crystallinity and morphology. On the other hand, the thermal induced stress may generate cracks in the film. These cracks are in the direction parallel to the c-axis of the ZnO film. In the SAW device fabrication, these cracks may short the IDT fingers and degrade the device performance. In the hybrid RF sputtering-MOCVD deposition, a thin ZnO buffer (~9 nm) was first deposited on the r-sapphire substrate by MOCVD to act as a seed layer for RF sputter deposition. Thick piezoelectric ZnO films were then deposited by RF sputtering on top of

the buffer layer. The RF sputtering targets are prepared by mixing ZnO and NiO (2-3%wt) powder for compensation doping to achieve piezoelectricity. The sputtering chamber is equipped with a standard RF power source. The substrates are rotated and heated to ~450°C. Deposition is carried out in a controlled ambient mixture of Ar and O_2 in ratio 1:1, with the overall chamber pressure maintained at ~$7x10^{-3}$ torr. Typical deposition rates ranges from 0.4 – 0.7 μm/hr. Following the sputter deposition the ZnO films are post-annealed in an O_2 atmosphere for 2 hours at temperatures ranging from 600 - 750°C, to improve film quality. Figure 5.4 (a) shows FESEM images of the piezoelectric ZnO films deposited by this hybrid deposition technique, followed by anneal at 700°C for 2 hours. The MOCVD grown seed layer improves the crystallinity and provides in-plane registry of the RF sputtered thick film with the r-sapphire substrate. The epitaxial relationship between the RF sputtered Ni-doped ZnO film and r-sapphire substrate is identified to be $(11\bar{2}0)$ ZnO ‖ $(01\bar{1}2)$ Al_2O_3 and [0001] ZnO ‖ $[0\bar{1}11]$ Al_2O_3. This hybrid deposition technique enables the growth of high quality thick ZnO films (>2.0 μm) on r- Al_2O_3 without cracks, while keeping the in-plane piezoelectric anisotropy for multi-mode acoustic wave generation. Because the doping of Ni, the as-sputtering ZnO film shows strong piezoelectricity. The hybrid techniques also waive the post-growth diffusion to save the processing steps.

In order to construct the active channel for ZnO tunable SAW device, the quality of the re-grown semiconducting ZnO film on top of the hybrid grown piezoelectric ZnO was also investigated. Figure 5.4 (b) shows the FESEM image of the smooth and dense re-grown ZnO layer. The inset represents a coupled x-ray θ-scan of the ZnO dual-layer structure. It clearly shows that both of the semiconducting and piezoelectric ZnO layers

are along the $(11\bar{2}0)$ a-plane.

To evaluate the SAW performance of the hybrid deposited piezoelectric ZnO film, SAW devices are made on the annealed samples. Figure 5.5 shows the SAW testing results on a hybrid RF sputtering-MICVD grown ZnO film (with post-growth O_2 anneal). The device wavelength is 8 μm with the delay length of 1.7 mm. The thickness of the ZnO film is ~2.3 μm. This device is aligned parallel to the c-axis of ZnO film. Multi-mode SAW responses have been observed. The basic Rayleigh wave is observed at center frequency of ~531 MHz with insertion loss of ~-38dB. The SAW velocity is ~ 4250 m/s. Sezawa wave is observed at center frequency of 665MHz with insertion loss of ~-19.7dB. The SAW velocity is ~5320 m/s. In comparison to the MOCVD grown film, it can be observed, ZnO film grown by hybrid RF sputtering-MOCVD technology generates better SAW response. This improvement might be resulted from the improved surface morphology and metal/piezoelectric material adhesion.

By aligning the SAW device perpendicular to the c-axis of ZnO film, Love wave mode was observed. Figure 5.6 shows the measured Love and Sezawa wave response on the ZnO films deposited by the hybrid RF sputtering-MOCVD method with similar thickness (~2.4 μm). The acoustic velocity of Love wave is smaller than Sezawa mode on ZnO/r-Al_2O_3 material system. For the Sezawa wave mode (SAW || [0001]), the center frequency is measured at 666.3 MHz, corresponding to v_{Sezawa}= 5330 m/s, with an insertion loss of –35.20 dB. For the Love wave mode (SAW || $[\bar{1}100]$, the center frequency is measured at 424.2MHz, corresponding to v_{Love}= 3393.6 m/s, with an insertion loss of –33.76 dB.

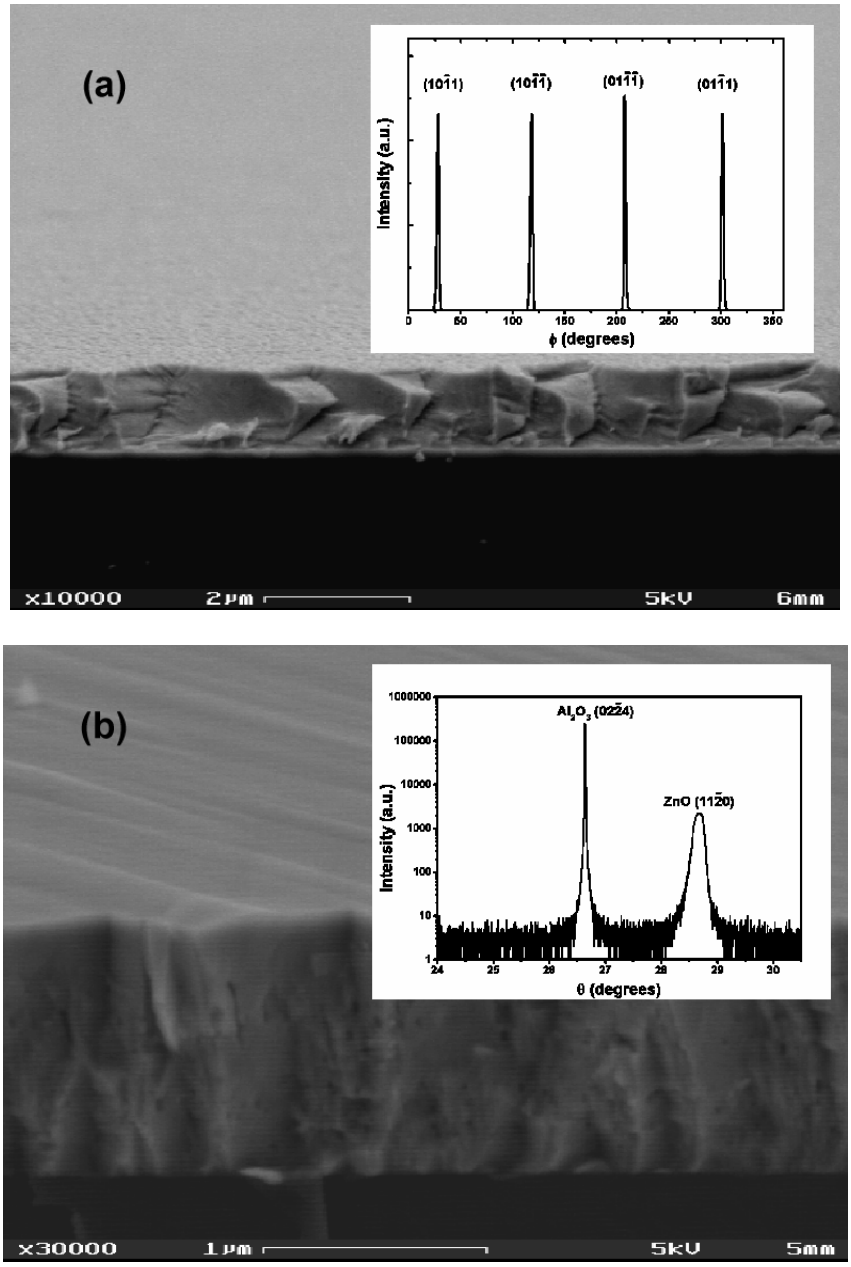

Figure 5.4. (a) FESEM image the sputtering deposited Ni-doped piezoelectric ZnO layer on r-Al_2O_3 substrate with a thin buffer ZnO layer. The inset shows x-ray phi scan of the film; (b) Semiconducting/piezoelectric ZnO dual-layer structure. The inset shows coupled x-ray θ-scan of the semiconducting ZnO film re-grown on the piezoelectric template

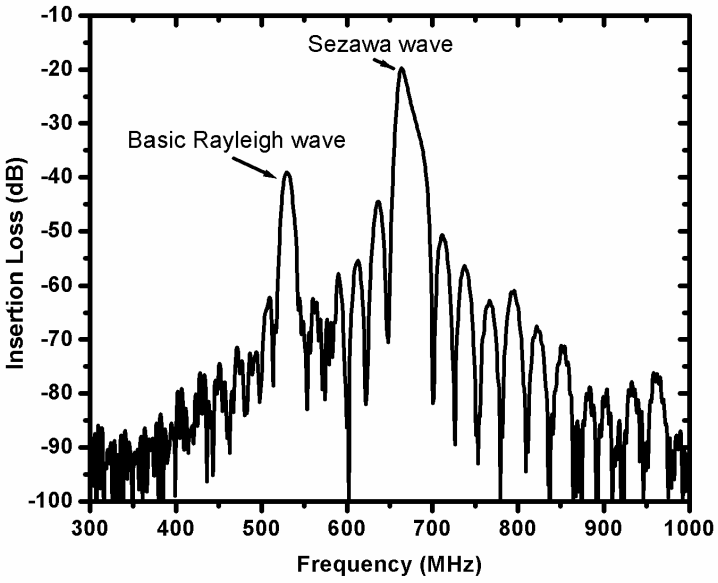

Figure 5.5 Rayleigh and Sezawa wave mode on a hybrid RF sputtering-MOCVD grown ZnO film

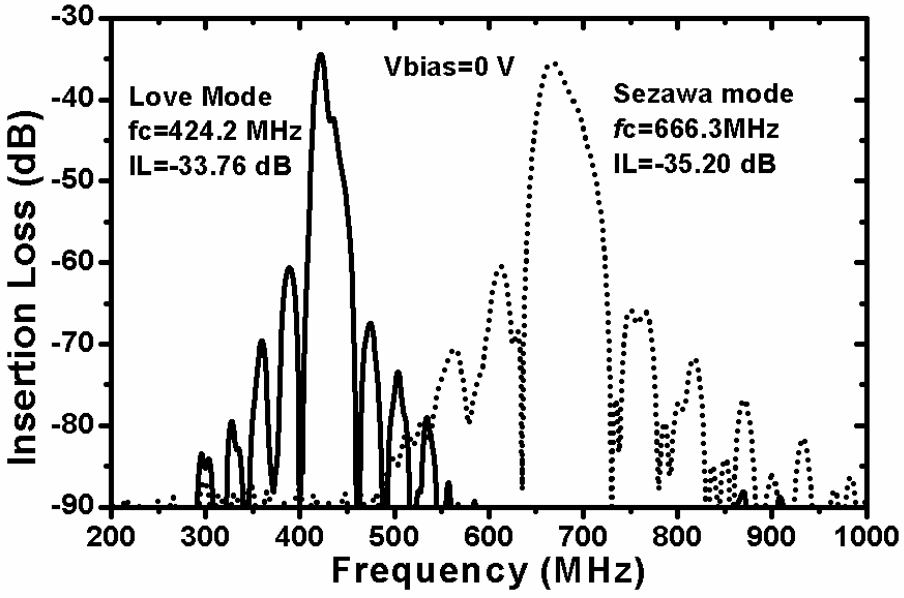

Figure 5.6 Love and Sezawa wave mode on a hybrid RF sputtering-MOCVD grown ZnO film

5.3 Fabrication Procedure and Testing Setup

Figure 5.7 gives an overview of the ZnO tunable SAW device fabrication flowchart. After the finish of the material growth, the ZnO tunable SAW device fabrication procedure mainly involves 1) Sample cleaning; 2) channel mesa patterning; 3) gate insulator deposition and patterning; 4) SAW aluminum IDT patterning and 5) top electrode patterning. Multiple processing techniques are used in the device fabrication including photolithography, ZnO thin film etching, SiO_2 deposition and etching, metallization and metal etching.

The sample cleaning process involves:

(i) Clean with acetone in an ultrasonic cleaner.

(ii) Clean in methanol.

(iii) Clean in DI water.

(iv) Dry the substrate with ultra pure nitrogen.

The wet chemical etching technique developed in chapter 3 is used in the channel mesa patterning. The SiO_2 gate insulator is deposited by a Plasma-Thermal 790 series PECVD system. The deposition condition is: substrate temperature: 250^{o}C; Wall temperature: 60 ^{o}C; SiH_4 flow rate: 200 sccm; N_2O flow rate: 1100 sccm; and RF power: 25 W. The SiO_2 gate is patterned with diluted BOE (1:7) solutions.

The microscopic images of a prototype ZnO tunable SAW device made on hybrid deposited piezoelectric ZnO film are shown in Figure 5.8 (a) Top view of the tunable SAW device; (b) Al IDT electrodes; and (c) channel mesa area.

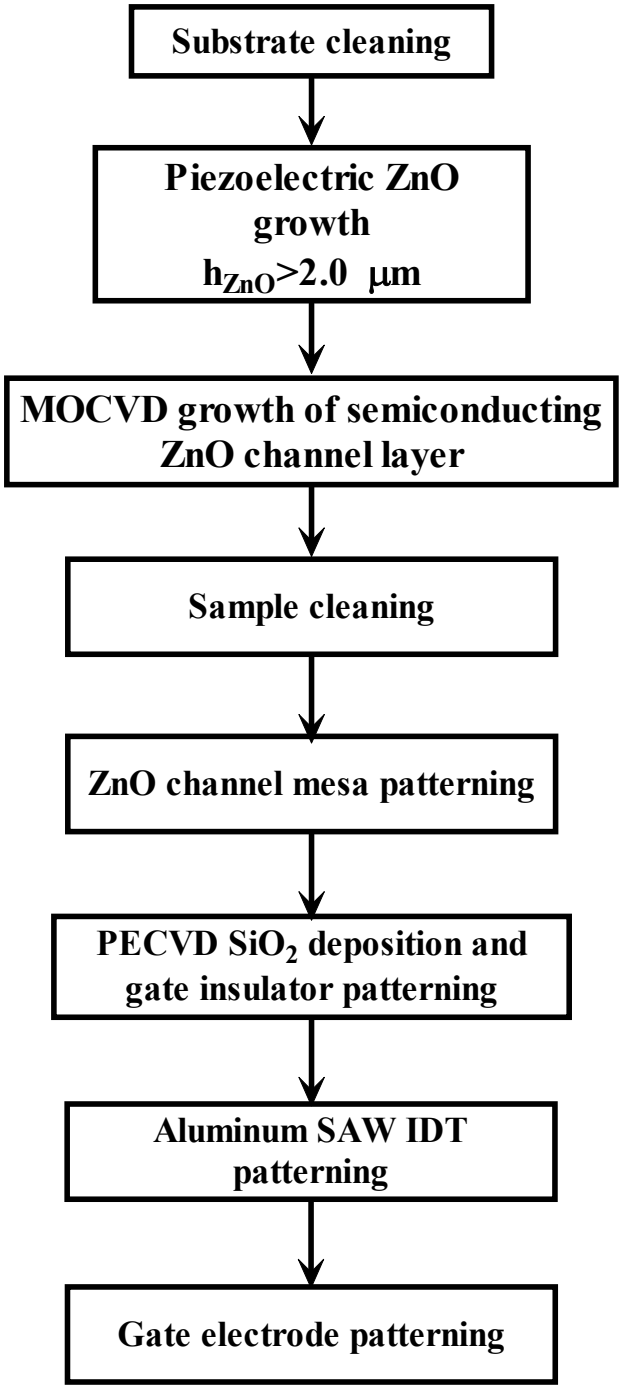

Figure 5.7 ZnO tunable SAW device fabrication flow chat

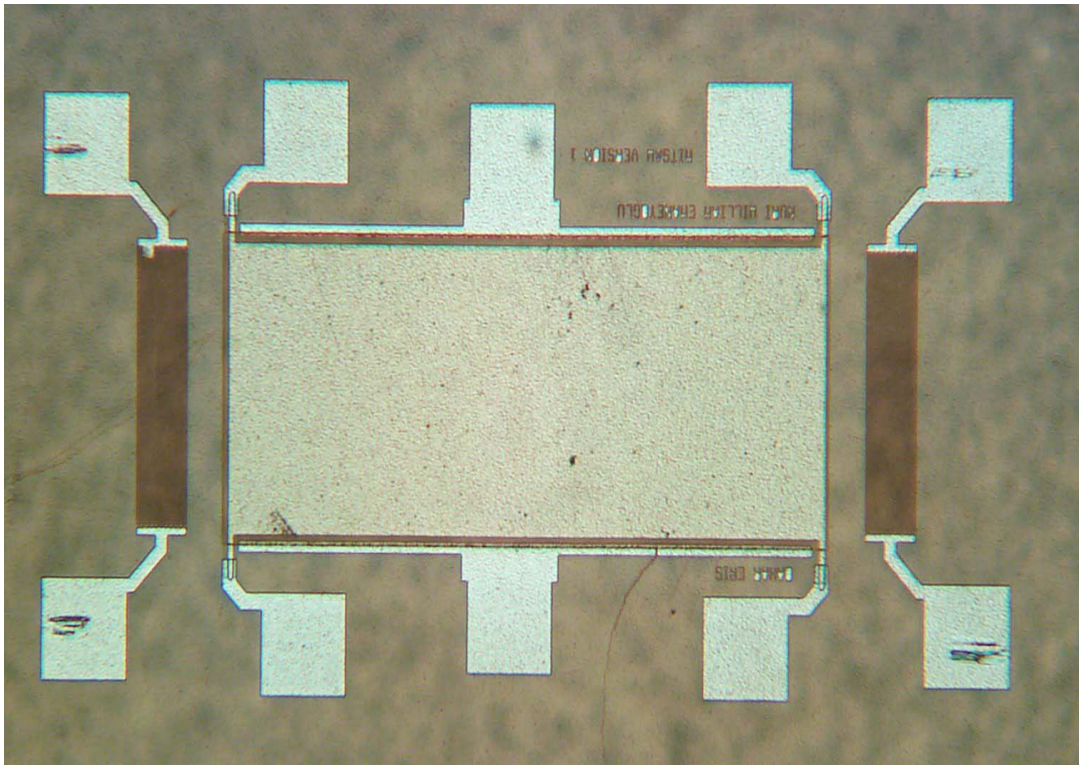

(a)

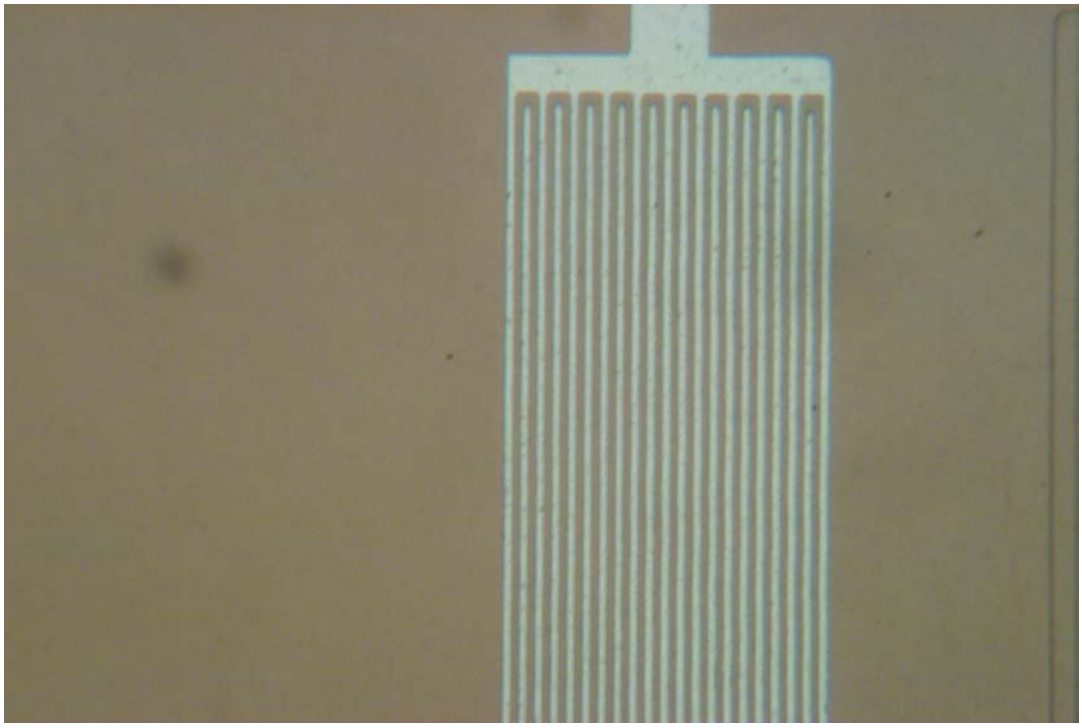

(b)

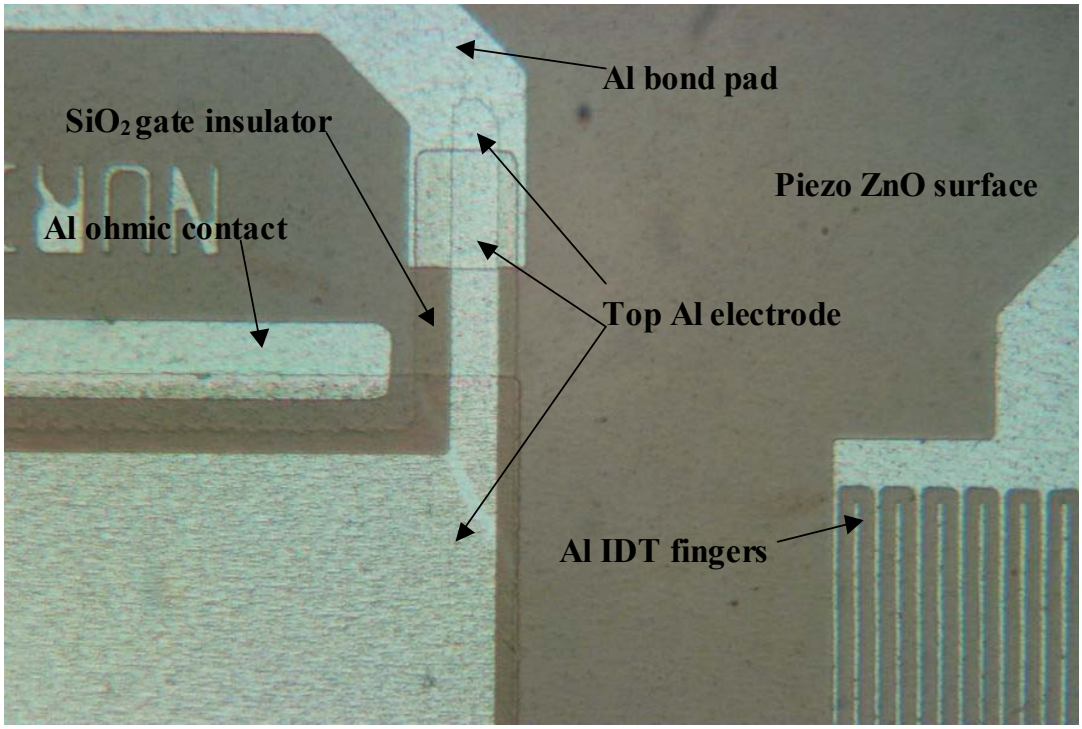

(c)

Figure 5.8 Optical microscopic images of the ZnO tunable SAW device, (a) Top view of the device; (b) Al IDT electrodes; (c) top electrode, gate insulator and channel mesa area

Tunable SAW Testing Setup

The voltage tunable SAW phase shifters were tested using a HP 8753D network analyzer and Cascade Microtech probes for the rf response (transmission parameter S_{21}). Under different biasing voltage, the phase shifts of the measured S_{21} are calculated with respect to the reference data (no biasing). The negative biasing and DC ground is supplied by a ± 20V DC power source. The bias induced phase shift across the device can be translated to the acoustic velocity change by

$$\frac{\Delta v}{v_0} = \frac{\Delta\phi \times \lambda}{360^o \times L_{mesa}} \tag{5.10}$$

where L_{mesa} is the length of the semiconducting mesa.

I-V measurements with HP 4156 C semiconductor parameter analyzer were used to determine the resistance change of the channel layer with respect to the bias voltage, which in turn is used to simulate the acoustic velocity change and attenuation based on Eq 2.40 and correlated with measured results.

5.4 Measurement of the Prototype ZnO based tunable SAW device

5.4.1 Prototype Tunable SAW device with MOCVD grown piezoelectric ZnO Film (Li doped)

Prototype tunable SAW devices were initially made with the MOCVD grown piezoelectric ZnO film (Li doped). Figure 5.9 shows the measured S_{21} (insertion loss) spectrum of a prototype tunable device under zero gate bias. The device parameters are: Wavelength= 8μm, delay length=1.2 mm; channel mesa length=1.0 mm, h_{piezo}=2.0 μm; $h_{channel}$=150 nm; and h_{SiO2}=220 nm. The center frequencies of Rayleigh and Sezawa wave mode are 576 MHz and 725 MHz, respectively. The insertion loss of the Rayleigh and Sezawa wave mode are -61 dB and -75 dB. Figure 5.10 and 5.11 shows the measured phase shift spectrum around the center frequency of the SAW mode with respect to the bias voltage (0 V to -20V, V_{step}=-4V) for basic Rayleigh and Sezawa wave mode, respectively. Under -20V bias, the phase shift of basic Rayleigh wave mode is ~6^o at f_c=576 MHz and the corresponding relative velocity change is only 133 ppm. In comparison, for the Sezawa wave mode, due to the higher coupling coefficient, the measured phase shift reaches ~130 ^{o} at f_c=725 MHz and the and the corresponding relative velocity change is 0.28%. Figure 5.12 shows the organized phase shift vs. bias relationship for both Rayleigh and Sezawa wave mode.

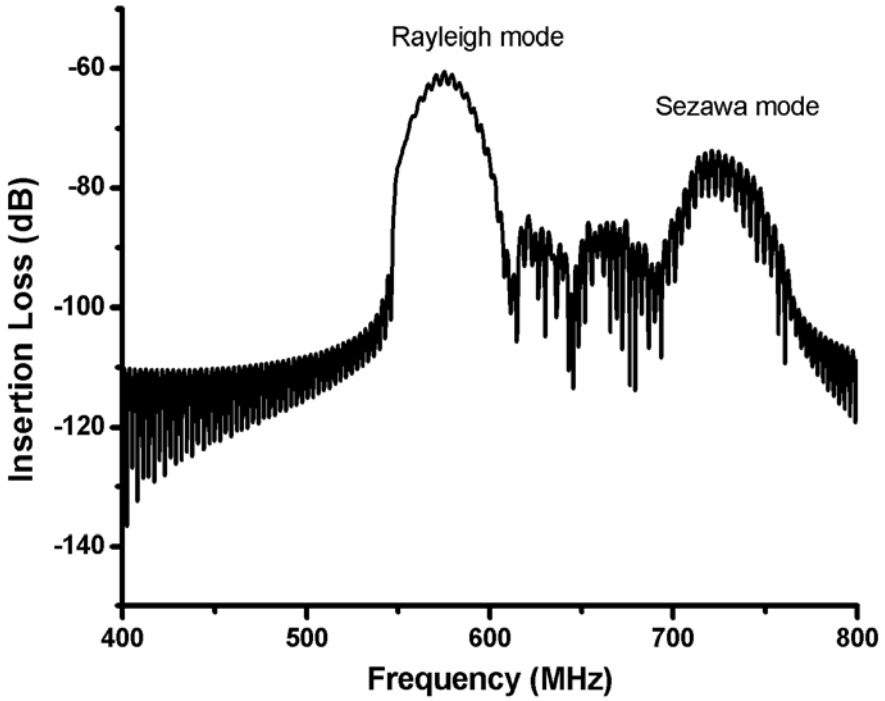

Figure 5.9. S_{21} spectrum of the prototype ZnO tunable SAW device under 0V bias

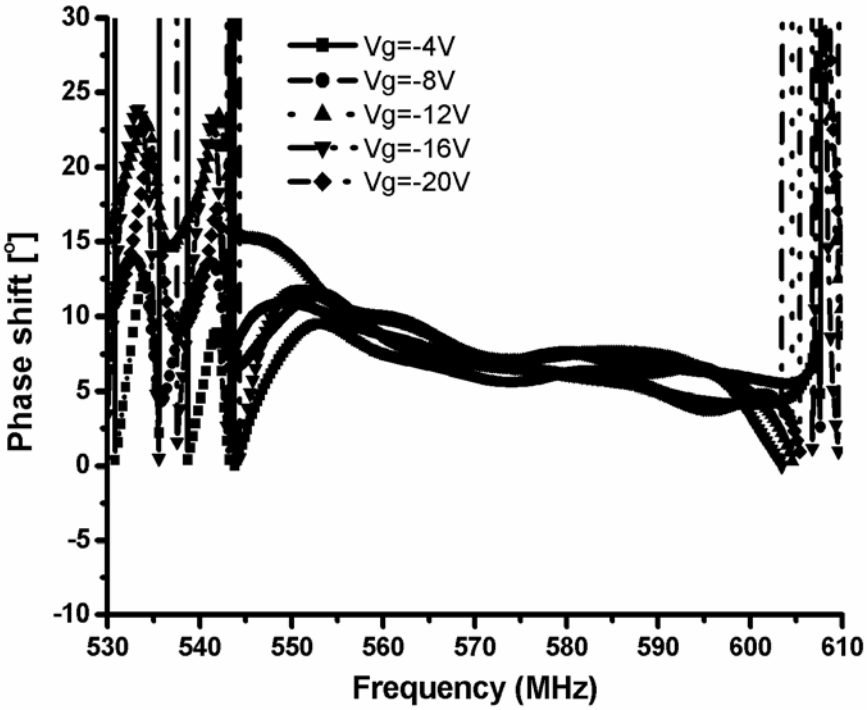

Figure 5.10. SAW Phase shift spectrum around the center frequency- Rayleigh mode (f_c=576 MHz)

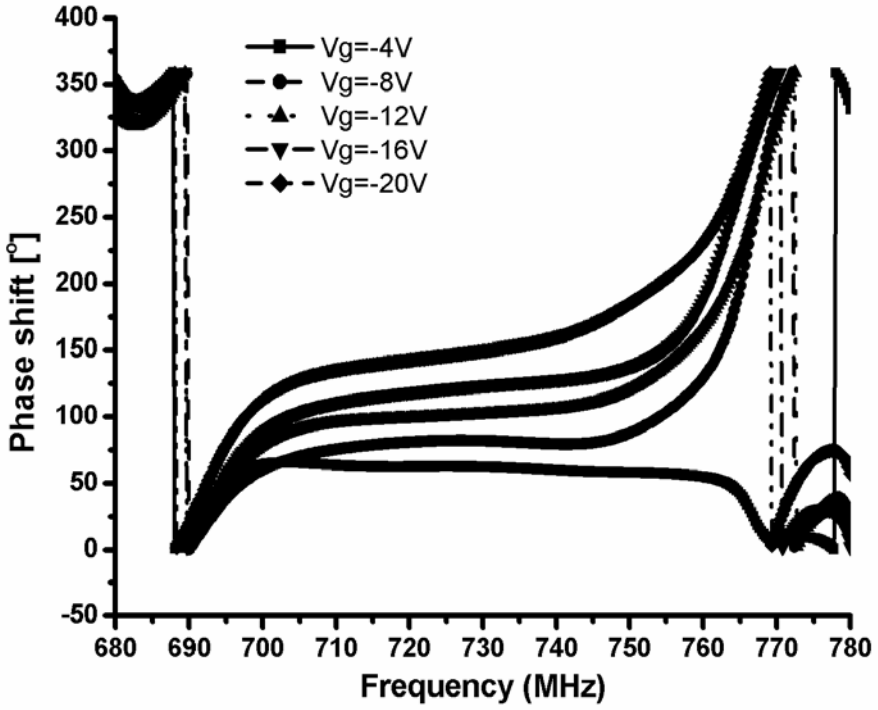

Figure 5.11. SAW Phase shift spectrum around the center frequency- Sezawa mode (f_c=725 MHz)

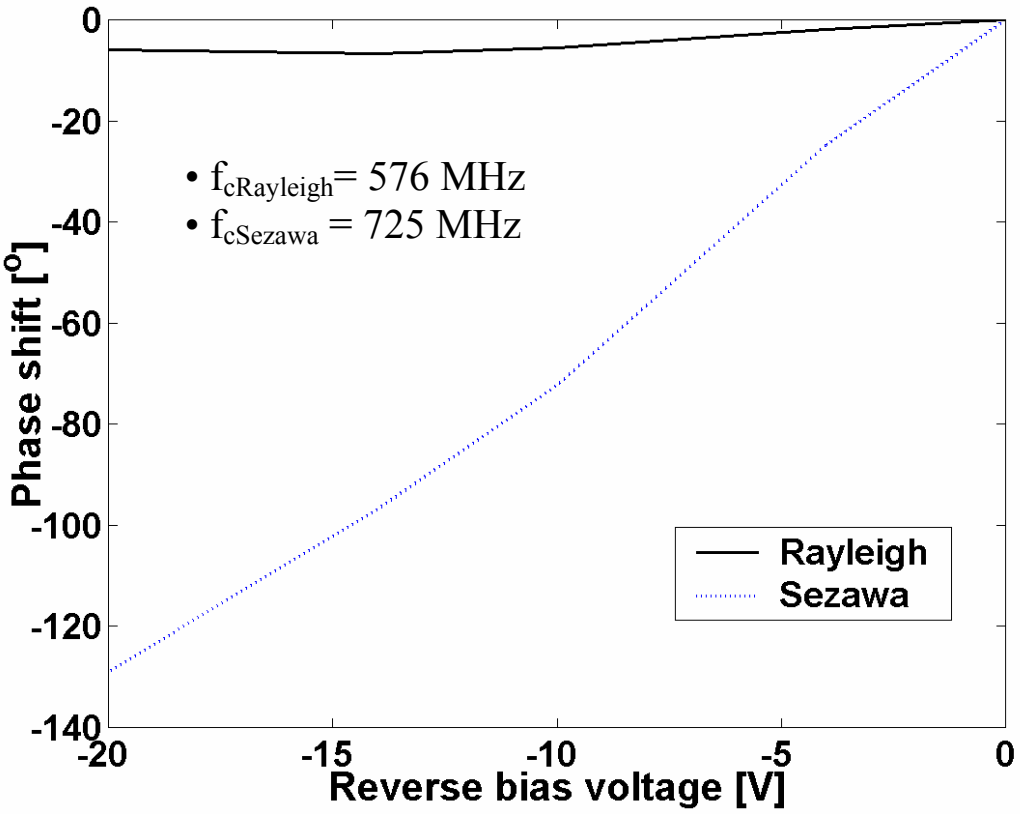

Figure 5.12 Phase shift vs. bias relationship for Rayleigh and Sezawa wave mode.

Based on the MOCVD grown piezoelectric ZnO film, a prototype ZnO tunable SAW has been developed. The acoustic velocity tunability has been demonstrated with basic Rayleigh and Sezawa wave mode. The device shows much larger phase shift and velocity tunability when operated with Sezawa wave mode than with Rayleigh mode, due to its high coupling coefficient. However, the prototype tunable SAW device shows limitation as 1) relatively high insertion loss. It will limit the device applications in areas such as adaptive filters and sensors. The high insertion loss may due to the non-sufficient Li diffusion for piezoelectricity and increased mechanical scattering of the SAW wave resulting from the increased surface roughness and particle accumulation during the MOCVD growth of thick ZnO film (~2.0 μm). 2) The phase and velocity tunability range of the device is relative small. Large tunability range is highly desired for many applications such as adaptive filters, Voltage Controlled Oscillators (VCO) and tunable sensors.

In comparison to the MOCVD growth, the RF sputtering-MOCVD deposited piezoelectric ZnO films show better SAW performance, meanwhile keep the in-plane piezoelectric anisotropy for multi-mode operation. To improve the performance of the ZnO tunable SAW device with respect to the insertion loss, velocity tunability and required bias, prototype devices has been developed based on the thick piezoelectric films deposited by the hybrid method.

5.4.2 Prototype Tunable SAW device with hybrid deposited piezoelectric ZnO Film (Ni doped)

Targeting for better device performance, prototype ZnO tunable SAW devices were developed based on the RF sputtering-MOCVD deposited piezoelectric ZnO film. The thickness of the piezoelectric ZnO layer is determined to be 2.4 μm for maximal coupling coefficient and larger acoustic tunability range. The channel thickness is reduced to 100 nm to reduce the required gate bias. The thickness of the SiO_2 gate dielectric is maintained as 220 nm. The prototype device parameters include: Wavelength= 8μm, delay length=1.7 mm; and channel mesa length=1.5 mm. Tunable SAW devices are made to operate with multiple wave mode (Sezawa or Love wave mode) by align the SAW devices along or perpendicular to the c-axis of the piezoelectric ZnO film.

The phase shifts and attenuations of the tunable SAW device around the center frequency are evaluated under different DC biasing with respect to its reference under V_g= 0V. Table 5.3 shows the measured attenuation and phase shift of Rayleigh and Sezawa wave mode under different DC bias. The center frequency of basic Rayleigh wave mode is 528 MHz, corresponding to $v_{Rayleigh}$=4656 m/s. In comparison, The Sezawa wave mode response is at 666.3 MHz, corresponding to v_{Sezawa}= 5330 m/s, which is close the estimated velocity leading to the maximum coupling coefficient. Within the DC bias tunable range, both of the attenuation and phase shift of the basic Rayleigh wave mode is very small. The acoustic velocity changes are located in the ppm range. Meanwhile, for Sezawa wave mode, the velocity change resulted by DC bias is much higher due to its high coupling coefficient. The maximal phase shift is 420^o with –18 V biasing, corresponding to 0.62% velocity change.

Figure 5.13 shows the detailed SAW spectrum (Sezawa mode) of the tunable SAW device with 0 V and –10 V DC biasing voltage. Under 0V biasing, the center frequency of Sezawa wave mode is 666.3 MHz and the insertion loss is –35.20dB. Under –10V DC biasing, the insertion loss increases to -53.87dB and the phase shift reaches 291^{o}, corresponding to 0.43% phase velocity change compared with the 0V biasing case. The phase shift at center frequency of Sezawa wave mode with respect to the biasing changing from 0 V to –10 V is shown in Figure 5.14. With an increase of negative biasing from 0V to –10V with –2V step, the phase shift increases continuously to 291^{o}. The phase transition around the center frequency (f_c ± 40MHz) is smooth with small phase noise.

By examining table 5.3, it can be found that the phase shift increases continuously with increasing gate bias. For the device with L_{mesa}=1.5 mm, the maximal phase shift is 420^{o} at –18 V bias, corresponding to a 0.62% velocity change. Meanwhile, the attenuation increases to the maximum –12.29 dB at –8V bias, then shows an inflexion and ends with -7.75 dB at –18V bias. These results match the acoustoelectric relaxation model, as the velocity has the fastest change and the attenuation has a maximum value when the sheet conductivity approaches the critical relaxation conductivity σ_m.

Biasing (V)	**Rayleigh mode (fc=528MHz)**			**Sezawa mode (fc=666.3MHz)**		
	Γ (dB/mm)	Δϕ (^{o})	Δ*v*/*v*	Γ (dB/mm)	Δϕ (^{o})	Δ*v*/*v*
0	0	0	0	0	0	0
-2	-0.25	-0.9	-10*ppm*	-1.57	5.8	***0.01%***
-4	-0.39	0.1	2 *ppm*	-5.20	29.6	***0.04%***
-6	-0.81	-0.5	-5*ppm*	-10.91	114.3	***0.17%***
-8	-1.02	-0.01	0	-12.29	209.1	***0.31%***
-10	-1.27	0.9	10 *ppm*	-11.93	291.0	***0.43%***
-12	-1.23	0.8	9 *ppm*	-11.11	334.9	***0.50%***
-14	-1.29	3.2	35 *ppm*	-10.21	367.0	***0.54%***
-16	-1.25	3.2	35 *ppm*	-9.32	395.0	***0.58%***
-18	-1.31	4.1	45 *ppm*	-7.75	419.8	***0.62%***

Table 5.3. Prototype tunable SAW device: Attenuation, phase shift and velocity change under different DC bias for Rayleigh and Sezawa wave mode.

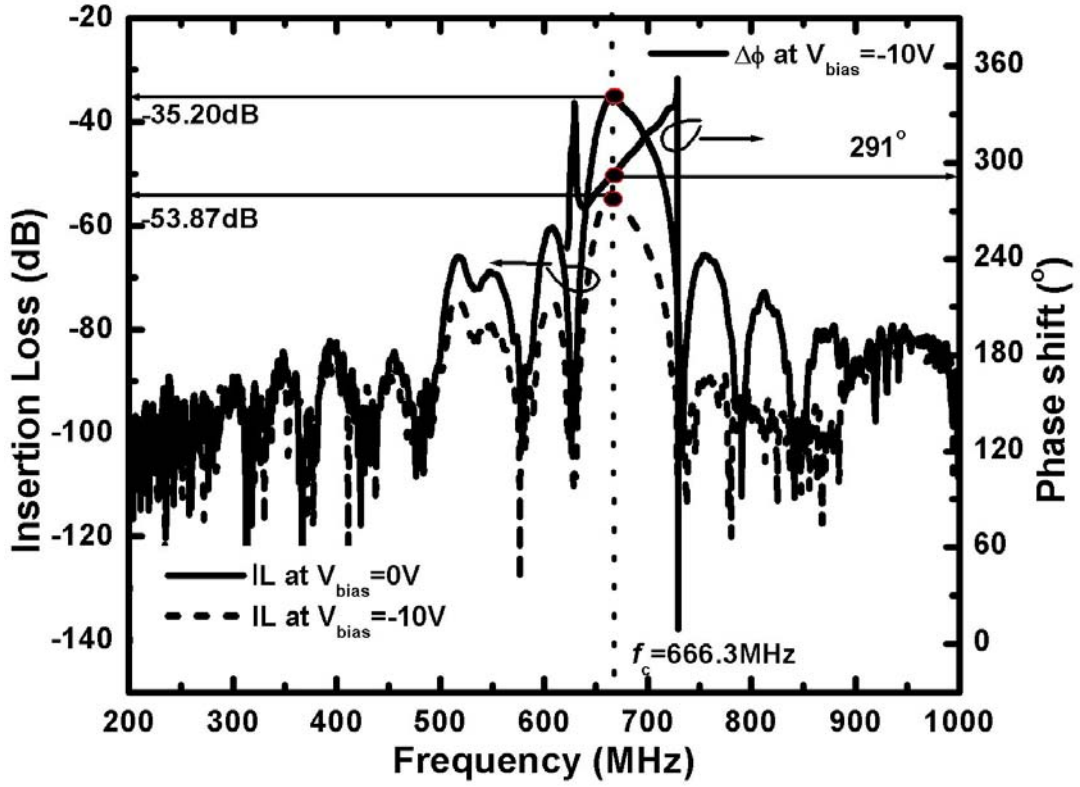

Figure 5.13. SAW spectrum of the tunable SAW device with 0 V and –10 V DC bias (Sezawa mode)

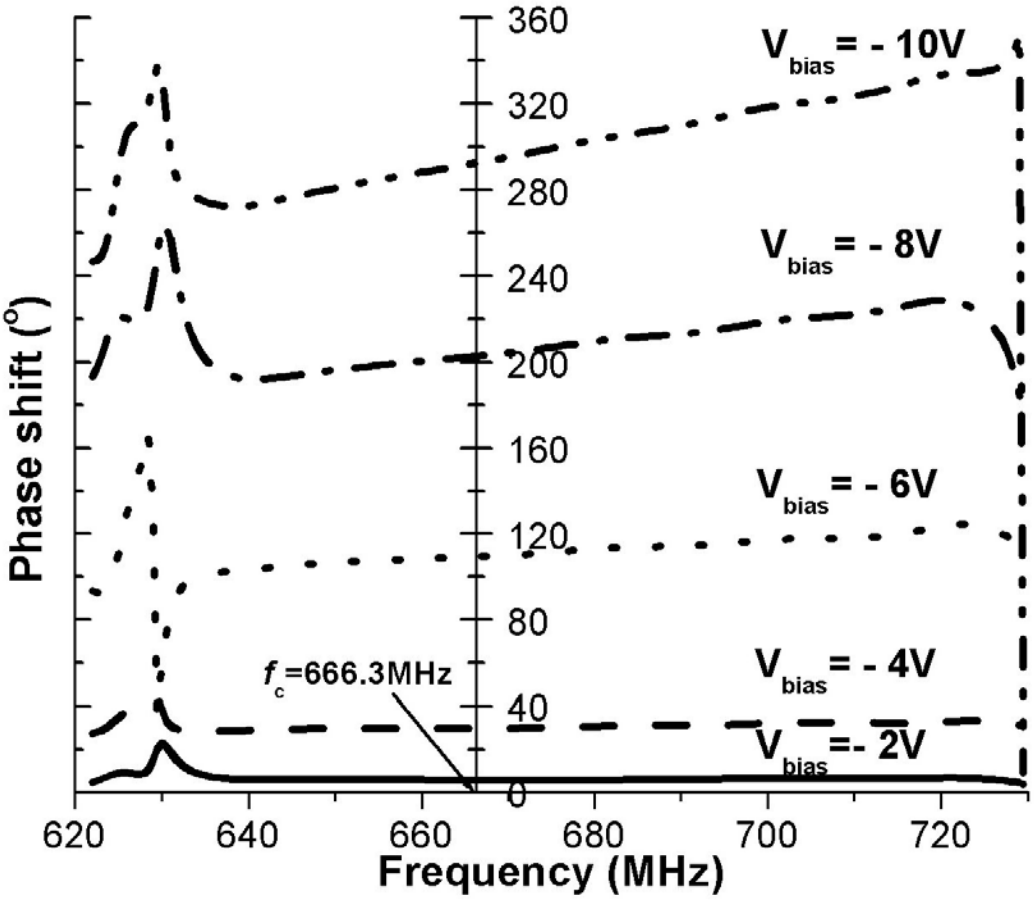

Figure 5.14. Frequency spectrum of the voltage controlled phase shift (Sezawa mode)

The performance of the tunable SAW device is also evaluated by comparing the testing results with the simulated results based on the acoustoelectric interaction described in chapter 2. To compare the measurement results with the acoustoelectric interaction modeling simulation, the original equations derived in the acoustoelectric interaction model need to be modified. In the acoustoelectric interaction model, the interaction between the SAW and thin semiconducting channel can result an acoustic velocity change as:

$$\frac{\Delta v}{v_0} = \frac{v - v_0}{v_0} = \frac{K^2_{eff}}{2} \frac{1}{1 + (\sigma_d / \sigma_M)^2} \tag{5.11}$$

where $\sigma_M = v_0 (\varepsilon_1 + \varepsilon_2)$, is the conductivity, at which the maximum loss occurs. K_{eff}^2 is the effective coupling coefficient. σ_d is the channel sheet conductivity.

However, this equation is derived for the situation, in which the open circuit velocity is used as the reference point. In the ZnO tunable SAW device, the initial reference points used is at 0 V bias and with sheet conductivity not equal to 0 (1/Ω) . Therefore, the equation used in the device simulation will has form as:

$$\frac{\Delta v}{v_0} = \frac{v_{NV} - v_{0V}}{v_0} = \frac{v_{NV} - v_0}{v_0} - \frac{v_{0V} - v_0}{v_0} = \frac{K^2_{eff}}{2} \frac{1}{1 + (\sigma_{NV} / \sigma_M)^2} - \frac{K^2_{eff}}{2} \frac{1}{1 + (\sigma_{0V} - \sigma_M)^2} \tag{5.12}$$

where σ_{NV} is the sheet conductivity with N (V) bias; σ_{0V} is the sheet conductivity with 0 (V) bias. By measuring the channel sheet conductivities with 0 V and various bias points, the acoustic velocity change can be calculated with respect to the external bias voltage. It needs to be noted that, although the maximal velocity change is achieved by changing the channel sheet conductivity from infinite (short circuit velocity) to zero (open circuit velocity) with the value of $\frac{\Delta v_{\max}}{v_0} = \frac{K^2_{eff}}{2}$, the acoustic velocity change can reach ~99% of

the maximal value when the channel sheet conductivity varies from $100\sigma_M$ to $0.01\sigma_M$. In the design of the device, it needs to be considered to limit the required bias.

The bias induced attenuation of the device is also extracted from the measured S_{21} parameters. The intensity of the transmitted SAW can be expressed as: $I = I_0 \exp(-\Gamma l)$, where I_0 denotes the intensity of the SAW just entering the semiconducting channel, and l is the length of the channel in the direction of SAW propagation. Γ is the attenuation coefficient with unit dB/mm or nepers/mm. From the measured S_{21} parameters, the Insertion Loss (IL) of the SAW device at the center frequency f_c can be determined. The insertion loss (IL) of a SAW in decibels (dB) is defined as:

$$IL = 10\log_{10}\frac{(power\ at\ load\ with\ no\ device\ present)}{(power\ at\ load\ with\ device\ inserted)} \tag{5.13}$$

The attenuation from y_1 to y_2 can be expressed as the amplitude ratio of the SAW from y_1 to y_2:

$$\frac{e^{-\Gamma y_1}}{e^{-\Gamma y_2}} = e^{-\Gamma(y_1 - y_2)} \quad (y_2 > y_1) \tag{5.14}$$

By taking the natural logarithm of the amplitude ratio, the attenuation measured in *nepers*, is:

$$Attenuation = \Gamma(y_2 - y_1) \text{ nepers} \tag{5.15}$$

A neper is actually a dimensionless quantity and the name is used simply to indicate that the attenuation is measured on a natural logarithmic scale. The attenuation factor Γ is therefore said to have units of nepers/meters or nepers/cm. In decibels, the attenuation from y_2 to y_1 is defined as:

$$Attneuation = 10\log(e^{-\Gamma(y_1 - y_2)})^2 = 20(\log e)\Gamma(y_2 - y_1) \text{ dB} \tag{5.16}$$

and is, consequently, a measure of (amplitude ratio)^2. The attenuation factor Γ is

converted from nepers/meter to dB/meter by multiplying with 20(log*e*). That is:

$$\Gamma(dB/meter) = 20(\log e)\Gamma(nepers/meters) \approx 8.686\Gamma(nepers/meter) \tag{5.17}$$

With the measured insertion loss (S_{21}) at the center frequency f_c, we may derive the attenuation coefficient Γ:

$$IL = S_{21} = 10\log(\frac{I_l}{I_0})2 = 20\log e^{-\Gamma l} = 20\log e(-\Gamma l) \tag{5.18}$$

where $I_l = I_0 \exp(-\Gamma l)$. By introducing the length of the SAW propagating path, the attenuation per unit length can be calculated with unit nepers/mm and can be transferred to dB/mm by multiply with 8.686. The attenuation per unit length in decibels can also be calculated directly by dividing the IL with delay length. The difference between these two attenuations is the attenuation after the application of negative biasing: $\Delta\Gamma = \Gamma_{NV} - \Gamma_{0V}$ and this ΔΓ is the attenuation per unit length used in the acoustoelectric interaction model.

In the modeling simulation, the attenuation equation derived is originally for the situation that the sheet conductivity changes from infinite to zero. In the real tunable SAW device, it needs to be modified to get the attenuation difference between the reference point (bias=0 V) and testing point (bias= N V). Similar as the derivation of the velocity equation, the attenuation difference can be expressed as:

$$\Gamma = \Gamma_{NV} - \Gamma_{0V} = 8.686(\frac{K_{eff}^2}{2}\frac{\pi}{\lambda}\frac{\sigma_{NV}/\sigma_M}{1+(\sigma_{NV}/\sigma_M)^2} - \frac{K_{eff}^2}{2}\frac{\pi}{\lambda}\frac{\sigma_{0V}/\sigma_M}{1+(\sigma_{0V}/\sigma_M)^2}) \text{ (dB/mm)} \tag{5.19}$$

where λ is the wavelength of the SAW device determined by the IDT finger design with unit (mm).

To simulate the acoustic velocity change and attenuation, I-V measurements were used to determine the sheet conductivity change of the channel layer with respect to the bias voltage. For the prototype tunable SAW device with λ=8 μm, the center frequency of the Sezawa mode is measured at 666.3 MHz, corresponding to v_{Sezawa}= 5330 m/s and the critical sheet conductivity is estimated to be $\sigma_M \sim 4.64 \times 10^{-7}$ S. For the Love wave mode, the center frequency is measured at 424.2MHz, corresponding to v_{Love}= 3393.6 m/s and the critical sheet conductivity is estimated to be $\sigma_M \sim 3.37 \times 10^{-7}$ S. Figure 5.15 (a) shows the measured (solid circle) and simulated (hollow circle) velocity change of the ZnO based tunable SAW device for the Sezawa wave mode and the measured sheet conductivity vs. DC bias results and, (b) shows the measured (solid star) and simulated (hollow star) attenuation. For Love mode operation**,** the phase shift and insertion loss change results show similar tendency as the Sezawa mode, while the maximal phase shift is 277.3^o at –18V bias, corresponding to a 0.42% velocity change. The maximum insertion loss is measured to be –9.99 dB/mm at –12V bias. The experimental and calculated velocity change and attenuation are shown in Figure 5.16.

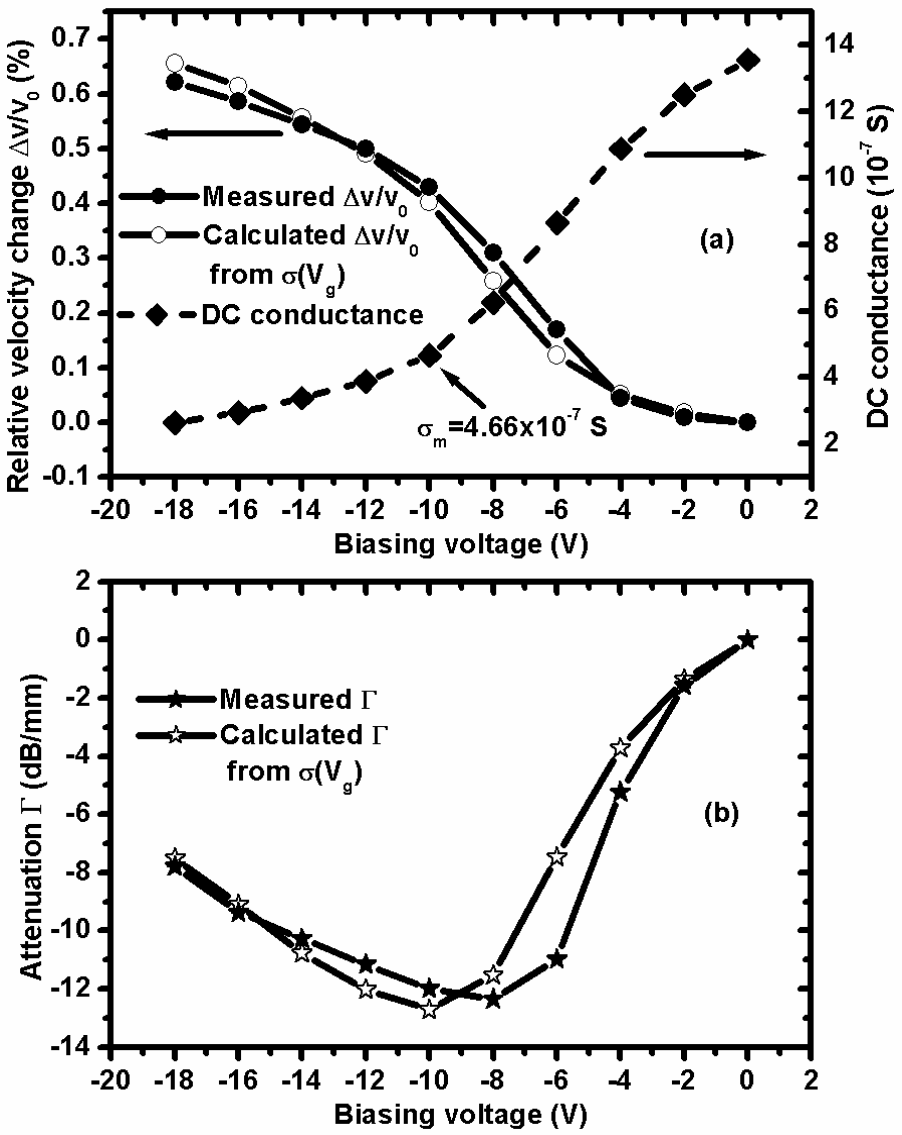

Figure 5.15 (a) Measured and simulated phase velocity change of the ZnO tunable SAW device (Sezawa mode), and measured DC conductance as function of the bias voltage, (b) Measured and simulated attenuation of the device as function of the bias voltage.

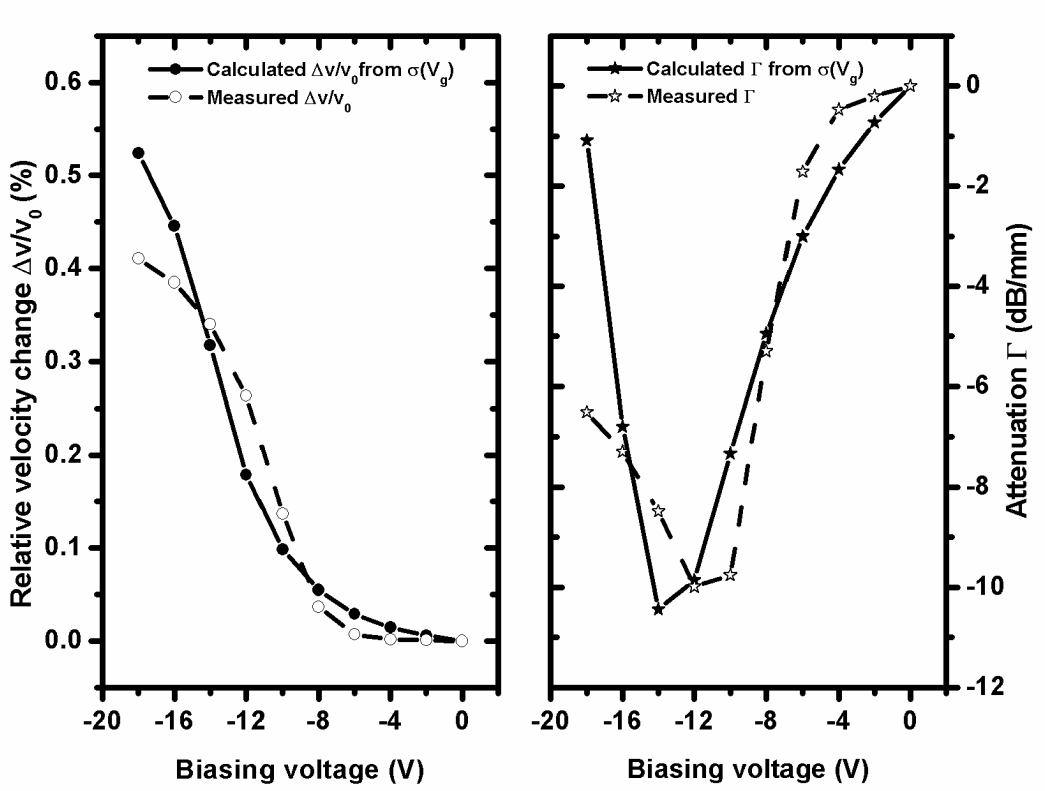

Figure 5.16 Measured and calculated velocity change and attenuation of the device (Love mode) as function of the bias voltage.

The measured results are generally in agreement with the calculation based on the acoustoelectric relaxation model. The discrepancy primarily results from the use of DC conductance in the model calculation. For the acoustoelectric interaction, only the conductance of the surface layer with thickness of a Debye-length is important for the attenuation, while the DC conductance gives a mean value for the film cross-section [6]. The estimated Debye screening length in the device is ~10 nm for N_{ZnO}~10^{17} cm^{-3}, which is one order of magnitude smaller than the thickness (h_{ZnO}=100 nm) of the semiconducting ZnO layer. The estimated effective coupling coefficient is 1.9% for the Sezawa mode and 1.2% for the Love mode. These effective coupling coefficients also match the simulation results based on the transfer matrix method. Figure 5.17 shows the simulated (a) coupling coefficient, and (b) velocity as function of the hf (m/s). The two data points in (a) indicate the operation point of current Sezawa and Love wave mode tunable SAW devices: R-Rayleigh wave mode; S-Sezawa wave mode and L-Love wave mode.

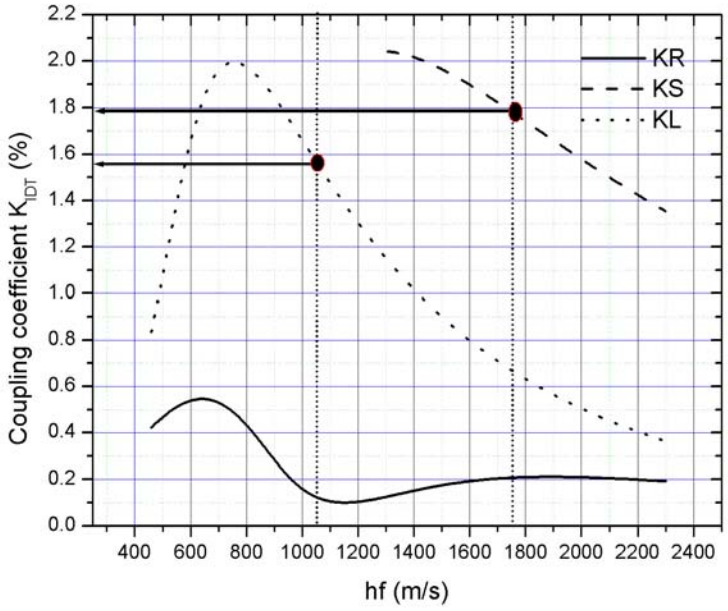

(a)

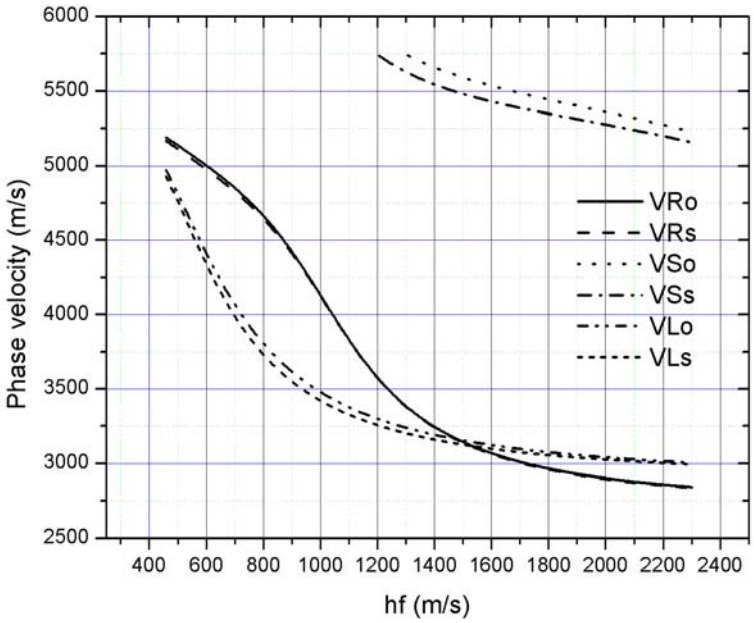

(b)

Figure 5.17 (a) the simulated coupling coefficient of Rayleigh, Sezawa and Love wave mode; (b) the simulated velocities with open and short surface.

A voltage controlled oscillator (VCO) can be implemented by inserting the tunable SAW phase shifter in the feedback loop of an oscillator circuit. The resonance frequency can be calculated based on:

$$\Delta f = \frac{1}{\tau}\frac{\Delta\phi}{360^o} = \frac{1}{\frac{L_{mesa}}{v_{SAW,mesa}} + \frac{L_{IDT}}{v_{SAW,IDT}}}\frac{\Delta\phi}{360^o} \tag{5.20}$$

With a –12 V DC bias, on the Sezawa wave, the 335° phase shift would result in a 2.9 MHz oscillation frequency shift, corresponding to a 0.44% relative frequency shift (f_c=666.3MHz); whereas for Love mode operation, the 178° phase shift would result in a 0.98 MHz oscillation frequency shift, corresponding to a 0.23% relative shift (f_c=424.2MHz). These devices are favorable in comparison with previously reported voltage controlled SAW devices in terms of the required bias voltage and the resulting tunability range. In the GaAs/$LiNbO_3$-Hybrid devices [41], a 470 μm 2DEG mesa was placed inside the delay line region and -10 V was used as the biasing voltage to achieve maximum phase shift. The oscillation frequency shift was reported to be 0.82 MHz, corresponding to a 0.193 % relative shift with respect to the center frequency at 434MHz. Table 5.1 shows the comparison between the ZnO based tunable SAW device and the reported data.

Reference	Device Structure	L_{mesa}	Biasing	$\phi\Delta$	$\Delta v/v$	Δf	f (MHz)	$\Delta f/f$ (%)
[27]	Topelectrode/LiNbO3 /bottom electrode	2.52mm	E=0.5 kV/mm	1^{o}	0.0022%	4.17kHz	189	0.0022%
[29]	Si/Air gap/LiNbO3	12mm	+30V (pulse)	180^{o}	0.06%	138kHz	230	0.06%
[31]	ZnO/SiO2/Si	4mm	-5V	67^{o}	0.085%	120kHz	214	0.056%
[30]	GaAs lateral MESFET and Schottky barrier diode	10mm	-60V	85^{o}	0.0575%	68kHz	118	0.0575%
[41]	GaAs 2DEG/LiNbO3	0.47mm	-10V	355^{o}	1.75%	0.84MHz	434	0.193%
Our results	SiO2/MOCVD ZnO/Sputtering ZnO/r-Sapphire	1.5mm	-13.5V	360^{o}	0.54%	3.18MHz	666.3	0.477%

Table 5.1 Comparison between the ZnO tunable SAW device with the reported data.

5.5 Summary

Based on the acoustoelectric interaction, a ZnO based voltage controlled multimode tunable SAW device is designed and demonstrated. The device is composed of piezoelectric ZnO film/r-Al_2O_3 system and SiO_2/semiconducting ZnO MIS structure. The acoustic velocity tunability is achieved by changing the sheet conductivity of the semiconducting ZnO channel through the gate bias. The device can be operated with both Sezawa and Love mode, which are suitable for gaseous and liquid environment sensing, respectively. Multiple sensing functions can be integrated in a single chip. Under –18 V bias, the 420^o and 277.3^o phase shifts are achieved for Sezawa and Love mode operation, respectively. The ZnO based tunable SAW devices are expected to find broad applications in communications, as well as in chemical/biochemical sensing.

Chapter 6. Conclusions and Future Work

6.1 Conclusions

This dissertation focuses on the research and development of ZnO based tunable SAW devices. The device operational principle is based on the acoustoelectric interaction, in which the electrical perturbation (charge density change) is coupled to the SAW propagating properties (acoustic velocity and attenuation).

In this dissertation work, to fulfill the requirement of device fabrication, the wet chemical etching and $SiCl_4$ based Reactive Ion Etching of ZnO and $Mg_xZn_{1-x}O$ films grown on r-Al_2O_3 by MOCVD have been studied. For the wet chemical etching of ZnO films, the etch rates of various etchants and composition ratios is investigated. Because the film's primary symmetric axis is located in plane, the wet chemical etching of $(11\bar{2}0)$ ZnO film shows in-plane anisotropy. To generate good etching profile, an optimized etching process by using H_3PO_4+$C_6H_8O_7$+H_2O, Al etch mask and short-time etching-rinsing cycles has been developed. A maximal vertical/horizontal-etching slope of 1:1 is obtained in the directions perpendicular to c-axis of $(11\bar{2}0)$ ZnO films. The XPS and electrical tests indicate that the etching process preserves the surface properties of the original films.

For the dry etching of ZnO and $Mg_xZn_{1-x}O$ films, $SiCl_4$ has been used as the etch gas. The etch rate of $Mg_xZn_{1-x}O$ increases with an increase of rf power and with a decrease of the chamber pressure. Due to the high boiling temperature of the etching products, the etch rate of $Mg_xZn_{1-x}O$ film decreases for higher Mg compositions. SiO_2 is used as the etch mask. Good etching profile and smooth etching surface are achieved. The SEM,

XPS and PL measurements show that under the optimized RIE conditions, there is no observable surface damage or optical deterioration of the etched ZnO and $Mg_xZn_{1-x}O$ films as compared to the as-grown samples.

Based on the acoustoelectric interaction, a prototype ZnO based UV SAW device has been designed and demonstrated by using a ZnO/$Mg_{0.2}Zn_{0.8}O$/piezo ZnO/r-Al_2O_3 multilayer structure. The UV sensing function of the semiconducting ZnO film is integrated to the SAW technology. The prototype device is tested under various light wavelength and power density. The UV SAW response closely follows the absorption spectrum of the ZnO film. For light wavelengths above 400 nm, the phase shift is small. The phase shift and insertion loss increases rapidly as the light wavelength approaches the band edge. For light wavelength of 365 nm and light power of 2.32 mW/cm^2, a phase shift of 107° is achieved. The demonstrated ZnO UV SAW device shows a better sensing performance than the report data, due to the higher coupling coefficient of ZnO/r-Al_2O_3 material system. The UV SAW device can be used as the passive zero-power remote wireless UV sensor, especially useful in the distributed sensor network.

An integrated voltage controlled multimode tunable SAW device has been designed and demonstrated by using piezoelectric ZnO film/r-Al_2O_3 system and SiO_2/semiconducting ZnO MIS structure. By changing the carrier density in the semiconducting ZnO channel through the MIS structure, voltage controlled acoustic velocity change is realized based on the acoustoelectric interaction. Due to the in-plane piezoelectric anisotropy of the ZnO/Al_2O_3 material system, the demonstrated device can be operated with both Sezawa and Love mode, which are suitable for gaseous and liquid environment sensing, respectively. Multiple sensing functions can be integrated in a

single chip. Under –18 V bias, a phase shift of 420^{o} is achieved for Sezawa mode operation, corresponding to 0.62% acoustic velocity change. For Love mode operation, the phase shift and corresponding velocity change are 277.3^{o} and 0.42%, respectively. The measurement results are compared with the simulation data and show good agreement. The estimated effective coupling coefficient is 1.9% for the Sezawa mode and 1.2% for the Love mode. The ZnO based tunable SAW devices are expected to find broad applications in communications, as well as in chemical/biochemical sensing.

6.2 Suggestions for Future Work

In order to improve the device performance and extend their applications, the following work is recommended for the future research and development of ZnO based multifunctional tunable SAW devices:

1. For the ZnO UV SAW device, single ZnO film is used as the UV sensing layer. In some applications, UV sensing with shorter wavelength is highly desired. In comparison to ZnO, $Mg_xZn_{1-x}O$ reduces the UV cutoff wavelength due to the enlargement of the energy band gap. The application of $Mg_xZn_{1-x}O$ to the UV SAW sensors to generate deep UV wireless sensing will be necessary.
2. For the ZnO based voltage controlled tunable SAW device, the efficiency of the carrier density tuning of the MIS structure directly impact the device performance with respect to the external bias and velocity tuning range. The material growth needs to be improved to increase the channel electron mobility for larger velocity tunability. The quality of the gate dielectric and dielectric/channel interface also needs to be improved to enhance the device

reliability, yield and reduce the operational bias. In comparison to SiO_2, high k dielectrics, such as HfO_2 and Al_2O_3, processes higher dielectric constant and gate capacitance, which will result a lower required bias for fixed velocity tunability. The study of high k MIS structure, including material deposition, interface quality control, charge depletion efficiency and the integration with tunable SAW device, is necessary for devices with low bias and large tunability.

3. Instead of single semiconducting ZnO channel, the using of 2DEG formed by $Mg_xZn_{1-x}O$/ZnO heterostructure offers the tunable SAW devices with larger tunability, smaller bias and faster response time. The material quality, strain effect and electrical properties will be investigated for $Mg_xZn_{1-x}O$/ZnO single and double heterostructure grown on r-Al_2O_3 substrates. The feasibility of tunable SAW devices with $Mg_xZn_{1-x}O$/ZnO heterostructure will be studied.
4. One of the important applications of the tunable SAW device is the adaptive SAW band-pass filter. The center frequency of the filter can be directly adjusted by the applied bias. To realize the filter frequency tunability, instead of the delay line region, the acoustoelectric interaction needs to be applied to the IDT region to directly tune the V_{IDT} and corresponding SAW center frequency. The charge density control through MIS or MS structure with single ZnO channel or $Mg_xZ_{1-x}nO$/ZnO 2DEG layer in the IDT region need to be studied for the adaptive filter application.

References:

1. B.A. Auld, Acoustic Fields and Waves in Solids, 1, 2nd ed. *Krieger Publishing Company, Malabar*, Florida, Appendix 2, (1990).

2. T. Lay, T. C. Wallance, Modern Global Seismology, 58, *Academic Press, INC.* (1995).

3. K. Sezawa, "Dispersion of Elastic Waves propagating on the Surface of Stratified Bodies and on Curved Surfaces," *Bulletin, Earthquake Research Institute*, Tokyo University, 3, 1 (1927).

4. C. K. Campbell, Surface Acoustic Wave Devices for Mobile and Wireless Communications, *Academic Press*, Boston, (1998).

5. A. R. Huston and D. L. White, "Elastic Wave Propagation in Piezoelectric Semiconductors", *J. Appl. Phys.* 33, 40 (1962).

6. K. A. Ingebrigtsen, "Surface Waves in Piezoelectrics", *J. Appl. Phys*. 40 (7), 2681 (1969).

7. K. A. Ingebrigtsen, "Linear and Nonlinear Attenuation of Acoustic Surface Waves in a Piezoelectric Coated with a Semiconducting Film", *J. Appl. Phys*. 41 (2), 454, (1970).

8. R. Adler, "Simple Theory of Acoustic Amplification", *IEEE Trans. Sonics Ultrason*. SU-18 (3), 115, (1971).

9. P. Bierbaum, "Interaction of ultrasonic surface waves with conduction electrons in thin metal films", *Appl. Phys. Lett.*, 21 (12), 595 (1972).

10. G. S. Kino, "Acoustoelectric interactions in acoustic-surface-wave devices", *Proc. of the IEEE*, 724, (1976).

11. A. Wixforth, J. Scriba, M. Wassermeier, J. P. Kotthaus, G. Weimann and W. Schlapp, "Interaction of surface acoustic waves with a two-dimensional electron system in a $LiNbO_3$-GaAs/AlGaAs sandwich structure", *J. Appl. Phys.* 64 (4), 2213 (1988).

12. M. Razeghi, "Short-wavelength solar-blind detectors-status, prospects and markets", *Proc. of the IEEE*, 90 (6), 1006, (2002).

13. D. Ciplys, R. Rimeika, A. Sereika, R. Gaska, M.S. Shur, J.W. Yang, and M.A Khan, "GaN-based SAW delay-line oscillator", *Elec. Lett.*, 37, 545, (2001).

14. D. Ciplys, R. Rimeika, M.S. Shur, S. Rumyantsev, R. Gaska, A. Sereika, J. Yang, and M.A Khan, "Visible–blind photoresponse of GaN-based surface acoustic wave oscillator", *Appl. Phys. Lett.*, 80, 2020, (2002).

15. T. Palacios, F. Calle, J. Grajal, E. Monroy, M. Eickhoff, O. Ambacher, and F. Omnes, High frequency SAW devices on AlGaN: Fabrication, characterization and integration with optoelectronics", *Proc. 2002 IEEE Ultrasonics Symp.*, 1, 55, (2002).

16. F. Calle, J. Pedros, T. Palacios, and J. Grajal, "Nitride-based surface acoustic wave. devices and applications", *Phys. Stat. Sol.* (c) 2 (3), 976 (2005).

17. D. Ciplys, M.S. Shur, R. Rmieika, J. Sinius, R. Gaska, Yu. Bilenko and Q. Fareed, "UV-LED controlled GaN-based SAW phase shifter", *Elec. Lett.*, 42, 1294, (2006).

18. P. Sharma, S. Kumar, and K. Sreenivas, "Interaction of surface acoustic waves and ultraviolet light in ZnO films", *J. Mater. Res.*, 18 (3), 545, (2003).

19. P. Sharma and K. Sreenivas, "Highly sensitive ultraviolet detector based on $ZnO/LiNbO_3$ hybrid surface acoustic wave filter", *Appl. Phys. Lett.*, 83, 3617, (2003).

20. S. Kumar, P. Sharma and K. Sreenivas, "Low intensity ultraviolet light detector using a surface acoustic wave oscillator based on $ZnO/LiNbO_3$ bilayer structure", *Semicond. Sci. Technol*. 20 (8), 27, (2005).

21. R.I. Amorosi, C.K. Campbell, "Studies of a Tunable SAW Oscillator Using a Differential SAW Delay Line with MOSFET Control", *IEEE Trans. Sonics Ultrason*. 32, 574, (1985).

22. J. Zhu, N.W. Emanetoglu, Y. Lu, J. A. Kosinski, R. Pastore, "A Multi-IDT Input Tunable Surface Acoustic Wave Filter", *IEEE Trans. Ultrason. Ferroelectr. Freq. Control*. 48, 1383, (2001)

23. S.A. Doberstein, K.V. Nikolaenko, M.A. Evdokimov, V.K. Razgonyaev, "A Wide-Range Tunable/Switchable Low-Loss SAW Filter", *Proc. 2000 IEEE Int. Ultrasonics Symposium*, 87, (2000).

24. A. Hietala, W.P. Robbins, "Design methodology for tunable SAW devices using magnetostrictive thin films", *Proc.-IEEE Ultrason. Symp*. 239, (1986).

25. S.G. Joshi, "Electronically Tunable SAW Oscillator on Temperature Stable Quartz Substrate", *Proc.-IEEE Ultrason. Symp*. 203, (1984)

26. A.J. Budreau, P.H. Carr, J.H. Silva, "New Configuration for Electronically Variable SAW Delay Line", *Proc.-IEEE Ultrason. Symp*., 399, (1982)

27. K. S. Kao, C. J. Chung, Y. C. Chen, C. C. Cheng, "Phase Tunable SAW Device on $LiNbO_3$ Substrate", *Ferroelectrics*, 304, 139, (2004).

28. B.D. Zaitsev, A.V. Ermolenko, V.A. Fedorenko, "Magnetoacoustic SAW Interaction in YIG Films", *Freq. Contr.,* 45, (2), 356, (1998).

29. A. Hietala, W.P. Robbins, “Design methodology for tunable SAW devices using magnetostrictive thin films”, *Proc. IEEE 1986 Int. Ultrasonics Symposium*, 239, (1986).

30. B. Altan, W.P. Robbins, "Tunable ZnO-Si SAW Devices Using Magnetostrictive Thin Films", *Proc. IEEE 1981 Int. Ultrasonics Symposium*, 311, (1981).

31. A.K. Ganguly, D.C. Webb, K.L. Davis, N.C. Koon, J.B. Milstein, "Magnetically Variable Surface-Wave Velocity in a Highly Magnetostrictive Rare-Earth-Iron Compound", *Proc. 1977 IEEE Int. Ultrasonics Symposium*, 785, (1977).

32. R. Hannebrekke, K.A. Ingebrigtsen, “Acoustoelectric amplification of surface waves in structure of cadmium-selenide film on lithium niobate”, *Electron. Lett.*, 6, (16), 520, (1970).

33. R.W. Ralston, “Stable CW operation of gap-coupled silicon-on-sapphire to $LiNbO_3$ acoustoelectric amplifiers”, *Proc. 1975 IEEE Int. Ultrasonics Symposium*, 217, (1975).

34. K.M. Lakin, H.J. Shaw, “Surface wave delay line amplifiers”, *IEEE Trans. Microwave Theory Tech.*, MTT-17, 912, (1969).

35. J. D. Crowley, J. F. Weller, T. G. Giallorenzi, “Acoustoelectric SAW phase shifter”, *Appl. Phys. Lett.* 31, 558, (1977)

36. T. W. Grudkowski, G. K. Montress, M. Gilden, J. F. Black, “Integrated Circuit Compatible Surface Acoustic Wave Devices On Gallium Arsenide”, *IEEE Trans. Microwave Theory Tech.*, MTT-29, 1348, (1981).

37. S. Urabe, “Voltage Controlled Monolithic SAW Phase Shifter and Its Application to Frequency Variable Oscillator”, *IEEE Trans. Sonics Ultrason*. 29, 255, (1985)

38. A. Wixforth, J. Scriba, M. Wassermeier, and J. P. Kotthaus, “Surface acoustic waves on $GaAs/Al_xGa_{1-x}As$ heterostructures”, *Phys. Rev. B*, 40 (11), 7874 (1989)

39. A. Wixforth, “Interaction of surface acoustic waves, electrons, and light”, *Int. J. High Speed Elec. Syst.*, 10 (4), 327, (2000).

40. C. Rocke, S. Manus, A. Wixforth, M. Sundaram, J.H. English, A.C. Gossard, “Voltage tunable acoustoelectric interaction in GaAs/AlGaAs heterojunctions”, *Appl. Phys. Lett*. 65, 2422, (1994).

41. M. Rotter, W. Ruile, A. Wixforth, and J. P. Kotthaus, “Voltage controlled SAW velocity in $GaAs/LiNbO_3$-hybrids”, *IEEE Trans. Ultrason. Ferroelectr. Freq. Control*. 46, 120, (1999).

42. D.C. Look, “Recent advances in ZnO materials and devices”, *Mat. Sci. & Eng* , B80, 383, (2001).

43. F.D. Auret, S.A. Goodman, M.Hayes, M.J. Legodi, H.A. van Laarhoven, D.C. Look, "Electrical characterization of 1.8 MeV proton-bombarded ZnO", *Appl. Phys. Lett.*, 79, (19), 3074, (2001).

44. F.D. Auret, S.A. Goodman, M.Hayes, M.J. Legodi, H.A. van Laarhoven, D.C. Look, "The influence of high energy proton bombardment on the electrical and defect properties of single-crystal ZnO", *J. Phys. Condensed Matter*, 13, 8989, (2001).

45. R. D. Vispute, V. Talyansky, Z. Trajanovic, S. Choopun, M. Downes, R. P. Sharma, T. Venkatesan, M. C. Woods, R. T. Lareau, K. A. Jones, "High quality crystalline ZnO buffer layers on sapphire (001) by pulsed laser deposition for III–V nitrides", *Appl Phys. Lett.*, 70, (20), 2735, (1997).

46. F. Hamdani, A. Botchkarev, W. Kim, H. Morkoç, M. Yeadon, J. M. Gibson, S.-C. Y. Tsen, D.J. Smith, D. C. Reynolds, D. C. Look, K. Evans, C. W. Litton, W. C. Mitchel, P. Hemenger, "Optical properties of GaN grown on ZnO by reactive molecular beam epitaxy", *Appl. Phys. Lett.*, 70, (4), 467, (1997).

47. Y. Liu, C.R. Gorla, N.W. Emanetoglu, S. Liang, Y. Lu, "Ultraviolet Detectors Based on Epitaxial ZnO Films Grown by MOCVD", *J. Elec. Mat.*, 27, (1), 69, (2000).

48. S. Liang, H. Sheng, Y. Liu, Z. Huo, Y. Lu, H. Shen, "ZnO Schottky ultraviolet photodetectors", *J. Crys. Growth*, 225, 110, (2001).

49. F.D. Auret, S.A. Goodman, M.J. Legodi, W.E. Meyer, D.C. Look, "Electrical Characterization of Vapor-Phase-Grown Single-Crystal ZnO", *Appl. Phys. Lett.*, 80, (8), 1340, (2002).

50. B. J. Coppa, R. F. Davis, R. J. Nemanich, "Gold Schottky Contacts on Oxygen Plasma-Treated, n-type ZnO ($000\bar{1}$)", *Appl. Phys. Lett.*, 82, (3), 400, (2003).

51. A. Salomon, D. Berkovich, D. Cahen, "Molecular Modification of an Ionic Semiconductor-Metal Interface: ZnO/Molecule/Au Diodes", *Appl. Phys. Lett.*, 82, (7), 1051, (2003).

52. P. Zu, Z. K. Tang, G.K.L. Wong, M. Kawasaki, A. Ohtomo, H. Koinuma, Segawa, "Ultraviolet Spontaneous and Stimulated Emissions from ZnO Microcrystallite Thin Films at Room Temperature", *Solid State Comm*. 103 (8), 459, (1997).

53. S.B. Zhan, S.-H. Wei, A. Zunger, "Intrinsic n-type versus p-type doping asymmetry and the defect physics of ZnO", *Phys. Rev. B*, 63, 075205/1, (2001).

54. D.C. Look, J. W. Hemsky, and J. R. Sizelove, "Residual native shallow donor in ZnO", *Phys. Rev. Lett*., 82, (12), 2552, (1999).

55. V. Srikant, V. Sergo, D.R. Clarke, "Epitaxial Aluminum-doped Zinc Oxide thin films on Sapphire: II, Defect equilibria and electrical properties", *J. Am. Ceram. Soc.,* 78, (7), 1935, (1995).

56. Y. Li, G.S. Tompa, S. Liang, C.R. Gorla, Y. Lu, “Transparent and Conductive Ga-Doped ZnO Films Grown by Low Pressure Metal Organic Chemical Vapor Deposition”, *J. Vac. Sci. & Technol. A*, 15, (3), 1063, (1997).

57. C.K. Lau, S.K. Tiku, K.M. Lakin, “Growth of epitaxial ZnO thin films by organometallic chemical vapor deposition”, *J. Electrochem. Soc.,* 127, (8), 1843, (1980).

58. H. Ieki, H. Tanaka, J. Koike, t. Nishikawa, “Microwave low insertion loss SAW filter by using ZnO/Sapphire substrate with Ni dopant”, *1996 IEEE MTT-S Digest*, 409, (1996).

59. J.-S. Lee, H.-J. Lee, S.-H. Seo, J.-S. Park, “Characterization of undoped and Cu-doped ZnO films for surface acoustic wave applications”, *Thin Solid Films*, 398-399, 641, (2001).

60. K. Minegishi, Y. Koiwai, Y. Kikuchi, K. Yano, M. Kasuga, A. Shimizu, “Growth of p-type Zinc Oxide films by chemical vapor deposition”, *Jpn. J. Appl. Phys. Part 2*, 36, (11A), 1453, (1997).

61. M. Joseph, H. Tabata, T. Kawai, “p-type electrical conduction in ZnO thin films by Ga and N codoping”, *Jpn. J. Appl. Phys. Part 2*, 38, (11A), 1205, (1999).

62. Y.R. Ryu, S. Zhu, D.C. Look, J.M. Wrobel, H.M. Jeong, H.W. White, “Synthesis of p-type ZnO films”, *J. Crystal Growth,* 216, 330, (2000).

63. Z. Jin, T. Fukumura, M. Kawasaki, K. Ando, H. Saito, T. Sekiguchi, Y. Z. Yoo, M. Murakami, Y. Matsumoto, T. Hasegawa, and H. Koinuma, “High throughput fabrication of transition-metal-doped epitaxial ZnO thin films: A series of oxide-diluted magnetic semiconductors and their properties”, *Appl. Phys. Lett*., 78, 3824, (2001).

64. K. Ando, H. Saito, Z. Jin, T. Fukumura, M. Kawasaki, Y. Matsumoto, H. Koinuma, “Magneto-optical properties of ZnO-based diluted magnetic semiconductors”, *J. Appl. Phys.*, 89, 7284, (2001).

65. S. W. Jung, S. –J. An, Gyu-Chul Yi, C. U. Jung, Sung-Ik Lee, and S. Cho, “Ferromagnetic properties of $Zn_{1-x}Mn_xO$ epitaxial thin films”, *Appl. Phys. Lett*., 80, 4561, (2002).

66. J. H. Kim, H. Kim, D. Kim, Y. E. Ihm, and W. K. Choo, “Magnetic properties of epitaxially grown semiconducting Zn1–xCoxO thin films by pulsed laser deposition”, *J. Appl. Phys*., 92, 6066, (2002).

67. S. Ramachandran, A. Tiwari, and J. Narayan, “$Zn_{0.9}Co_{0.1}O$-based diluted magnetic semiconducting thin films”, *Appl. Phys. Lett*., 84, 5255, (2004).

68. E. R. Segnit and A. E. Holland, "The System MgO-ZnO-SiO_2", J. Am. Ceram. Soc. 48, 412, (1965).

69. A. Ohtomo, M. Kawasaki, T. Koida, K. Masubuchi, H. Koinuma, Y. Sakurai, Y. Yoshida, T. Yasuda, Y. Segawa, "$Mg_xZn_{1-x}O$ as a II–VI widegap semiconductor alloy", *Appl. Phys. Lett.*, 72 (19), 2466, (1998).

70. A. Ohtomo, M. Kawasaki, I. Ohkubo, H. Koinuma, T. Yasuda, Y. Segawa, "Structure and optical properties of $ZnO/Mg_{0.2}Zn_{0.8}O$ superlattices", *Appl. Phys. Lett.*, 75 (7), 980, (1999).

71. T. Gruber, C. Kirchner, R. Kling, F. Reuss, and A. Waag, "ZnMgO epilayers and ZnO–ZnMgO quantum wells for optoelectronic applications in the blue and UV spectral region", *Appl. Phys. Lett*. 84, 5359, (2004).

72. S. Liang, C.R. Gorla, N.W. Emanetoglu, Y. Liu, W.E. Mayo, Y. Lu, "Epitaxial growth of ($11\bar{2}0$) ZnO on ($01\bar{1}2$) Al_2O_3 by metalorganic chemical vapor deposition", *J. Elec. Mat.*, 27, (11), L72, (1998).

73. C.R. Gorla, N.W. Emanetoglu, S. Liang, W.E. Mayo, Y. Lu, M. Wraback, H. Shen, "Structural, optical, and surface acoustic wave properties of epitaxial ZnO films grown on ($01\bar{1}2$) sapphire by metalorganic chemical vapor deposition", *J. Appl. Phys.*, 85, (5), 2595, (1999).

74. S. Muthukumar, J. Zhong, Y. Chen, Y. Lu, T. Siegrist, "Growth And Structural Analysis Of Metalorganic Chemical Vapor Deposited ($11\bar{2}0$) $Mg_xZn_{1-x}O$ ($0<x<0.33$) Films on ($01\bar{1}2$) R-plane Al_2O_3 substrates", *Appl. Phys. Lett.*, 82, (5), 742, (2003).

75. H. Maki, T. Ikoma, and I. Sakaguchi, "Control of surface morphology of ZnO (000-1) by hydrochloric acid etching", *Thin Solid Films*, (411), 91, (2002).

76. F.S. Hickernell, and T.S. Hickernell, "The etched surface of sputtered zinc oxide and its relationship to fractal growth and surface wave properties", *Proc. 1992 IEEE Int. Ultrasonics Symposium*, 373, (1992).

77. S.J. Pearton, D. P. Norton, K. Ip, and Y. W. Heo, "Recent advances in processing of ZnO", *J. Vac. Sci. Technol.*, B 22 (3), 932, (2004).

78. S. C. Chang, D.B. Hicks, and R.C.O. Laugal, "Patterning of zinc oxide thin films", *Proc. IEEE Solid-State Sensor Actuator Workshop*, 41, (1992).

79. T. Xu, G. Wu, G. Zhang and Y. Hao, "The compatibility of ZnO piezoelectric film with micromachining process", *Sensors Actuat. A-Phys*, 104, 61, (2003).

80. J. W. Kwon, and E. S. Kim, "Fine ZnO patterning with controlled sidewall-etch front slope", *J. Microelectromech. S.*, 14, 603, (2005).

81. M. J. Vellekoop, C.C. G. Visser, P. M. Sarro and A. Venema, “Compatibility of zinc oxide with silicon IC processing”, *Sensors Actuat. A-Phys*, A21, 1027, (1990).

82. Y. Ito, K. Kushida, K. Sugawara, and H. Takeuchi, “A 100-MHz ultrasonic transducer array using ZnO thin films”, *IEEE Trans. Ultrason., Ferroelect., Freq. Contr.*, 42, 316, (1995).

83. K. C. Lou, X. Zhu, H. Lakdawala and E. S. Kim, “Study on etch front of piezoelectric ZnO film and new step coverage technique”, *Proc. 1997 IEEE Int. Ultrasonics Symposium*, 565, (1997).

84. O. Kluth, A. Loffl, S. Wieder, C. Beneking, W. Appenzeller, L. Houben, B. Rech, H. Wagner, S. Hoffmann, R. Waser, J.A.A. Selvan, H. Keppner, “Texture etched Al-doped ZnO: a new material for enhanced light trapping in thin film solar cells”, *Proc. 26th Photovoltaic Specialists Conf.*, 715, (1997).

85. *Current topics in mateials science*, vol. 7. New York: North-Holland Publishing Company, (1981).

86. R.C. Weast, *Handbook of Chemistry and Physics,* 57th ed. Boca Raton, FL: CRC Press, Inc. (1976).

87. S.S. Tan, M.Ye and A.G.Milnes, « Diffusion limited chemical etching effects in semiconductors”, *Sol. St. Electron.,* 38, 17, (1995).

88. H. W. Lehmann, *Thin Film Processes II*. Boston: Academic Press, 1991

89. N. Madou, *Fundamentals of Microfabrication*. Boca Raton: CRC Press LLC, 1997.

90. Editorial, *Semicon. Intl.*, 72-76, 1992

91. J.-M. Lee, K.-M. Chang, K.-K. Kim, W.-K. Choi, and S.-J. Park, “Dry Etching of ZnO Using an Inductively Coupled Plasma”, *J. Electrochemic. S.*, 148 (1) G1, (2001).

92. K. Ip, K. H. Baik, M. E. Overberg, E. S. Lambers, Y. W. Heo, D. P. Norton, S. J. Pearton, F. Ren, and J. M. Zavada, “Effect of High-Density Plasma Etching on the Optical Properties and Surface Stoichiometry of ZnO”, *Appl. Phys. Lett.*, 81, 3546, (2002).

93. J. S. Park, H. J. Park, Y. B. Hahn, G. C. Yi, and A. Yoshikawa, “Dry etching of ZnO films and plasma-induced damage to optical properties”, *J. Vac. Sci. Technol.*, B 21 (2), 800, (2003).

94. W. T. Lim, I. K. Baek, J. W. Lee, E. S. Lee, M. H. Jeon, G. S. Cho, Y. W. Heo, D. P. Norton, and S. J. Pearton, “Temperature-Dependent Cl2/Ar Plasma Etching of Bulk Single-crystal ZnO”, *Appl. Phys. Lett.*, 83, 3105, (2003).

95. K. Ogata, T. Honden, T. Tanite, and T. Komuro, K. Koike, S. Sasa, M. Inoue, and M. Yano, “Electron-cyclotron-resonance plasma etching of the ZnO layers grown by molecular-beam epitaxy”, *J. Vac. Sci. Technol.*, A 22(3), 531, (2004).

96. H.-K. Kim, J. W. Bae, T.-K. Kim, K.-K. Kim, T.-Y. Seong, and I. Adesida, “Inductively Coupled Plasma Reactive Ion Etching of ZnO using BCl_3-based Plasmas”, *J. Vac. Sci. Technol.*, B 21 (4), 1273, (2003).

97. J.-W. Bae, C.-H. Jeong, H.-K. Kim, K.-K. Kim, N.-G. Cho, T.-Y. Seong, S.-J. Park, I. Adesida, and G.-Y. Yeom, “High-Rate Dry Etching of ZnO in BCl3/CH4/H2 Plasmas”, *Jpn. J. Appl. Phys.*, 42, L535, (2003).

98. H.-K. Kim, J. W. Bae, K.-K. Kim, S.-J. Park, T.-Y. Seong, and I. Adesida, “Inductively-coupled-plasma reactive ion etching of ZnO using BCl3-based plasmas and effect of the plasma treatment on Ti/Au ohmic contacts to ZnO”, *Thin Solid Films*, 447, 90, (2004).

99. N. W. Emanetoglu, G. Patounakis, S. Liang, C. R. Corla, R. H. Wittstruck, and Y. Lu, “Analysis of SAW properties of epitaxial ZnO films grown onR-Al_2O_3 substrates”, *IEEE Trans. Ultrason. Ferroelectr. Freq. Control*, 48, 1389, (2001).

100. H. Sheng, S. Muthukumar, N.W. Emanetoglu, and Y. Lu, “Schottky diode with Ag on (11-20) epitaxial ZnO film”, *Appl. Phys. Lett.*, 80 (12), 2132, (2002).

101. P. Wu, N. W. Emanetoglu, S. Muthukumar, Y.chen, Y. Lu., “Li diffusion in epitaxial (11-20) ZnO thin films”, *J. Electron. Mater.*, 33, 596, (2004).

102. E. L. Adler, “Matrix methods applied to acoustic waves in multilayers”, *IEEE Trans. Ultrason. Ferroelectr. Freq. Control* 37, 485, (1990).

103. A. Ohtomo, K. Tamura, K. Saikusa, K. Takahashi, T. makino, Y. Segawa, H. Koinuma, and M. Kawasaki, “Single crystalline ZnO films grown on lattice-matched $ScAlMgO_4$(0001) substrate”, *Appl. Phys. Lett.* 75, 2635, (1999)

104. D. L. Rode, “Low-field electron transport”, Semicond. Semimet. 10, 1, (1975).

105. O. Medelung (Ed.) and Landolt-Borstein, Semiconductors, Springer, Berlin III-17, 35, (1998).

106. K. B. Sundaram and A. Khan, “Work function determination of zinc oxide films”, J. Vac. Sci. Technol. A 15, 428, (1997).

Curriculum Vita

Jun Zhu

Education

July 1993	Bachelor of Science in Electrical Engineering Xi'an Jiaotong University, Xi'an, China
July 1996	Master of Science in Electrical Engineering Xi'an Jiaotong University, Xi'an, China
January 2008	Doctor of Philosophy in Electrical and Computer Engineering, Rutgers University, New Brunswick, New Jersey

Related Publications

Journals

1. "ZnO TFT Devices Built on Glass Substrates", J. Zhu, H. Chen, G. Saraf, Z. Duan, Y. Lu and S. T. Hsu, accepted by *Journal of Electronic Materials* 2007.
2. "Voltage Tunable Surface Acoustic Wave Phase Shifter Using Semiconducting/piezoelectric ZnO Dual-layers Grown on r-Al_2O_3", J. Zhu, Y. Chen, G. Saraf, N.W. Emanetoglu, Y. Lu, *Applied Physics Letters*, 89, pp 103513, 2006
3. "$SiCl_4$-based Reactive Ion Etching of ZnO and $Mg_xZn_{1-x}O$ Films on r-sapphire Substrates", J. Zhu, G. Saraf, J. Zhong, H.F. Sheng, B.V. Yakshinskiy and Y.Lu, *Journal of Electronic Materials*, Vol. 35, No. 6, pp 1311-1315, 2006.
4. "Optoelectronic-acoustic Interaction in ZnO/r-Al_2O_3 for Tunable Surface Acoustic Wave Filters and Ultraviolet Photodetectors", N. W. Emanetoglu, J. Zhu, Y. Chen, J. Zhong, Y. Chen, Y. Lu, *Applied Physics Letters*, 85, pp.3702, 2004.
5. "Wet chemical etching of $(11\bar{2}0)$ ZnO films", Jun Zhu, N.W. Emanetoglu, Y. Chen, B.V. Yakshinskiy, Y. Lu, *Journal of Electronic Materials*, Vol. 33, No. 6, pp 556-559, 2004.
6. "Characteristics of $Mg_xZn_{1-x}O$ Bulk Acoustic Wave Devices", R.H. Wittstruck, X. Tong, N.W. Emanetoglu, P. Wu, Y. Chen, J. Zhu, S. Muthukumar, Y. Lu, *IEEE Transactions on Ultrasonics, Ferroelectrics, and Frequency Control*, Vol. 50, No. 10, pp: 1272-1278, Oct. 2003.

Patents:

"MOCVD-Sputtering Hybrid Technology to Deposit Multilayer and Multifunctional Epitaxial Films" with Prof. Y. Lu, Y. Chen and Saraf, Gaurav, US patent filed in 2006.